Tetraspanin web formation and function

Dissertation

zur

Erlangung des Doktorgrades (Dr. rer. nat.)

der

Mathematisch-Naturwissenschaftlichen Fakultät

der

Rheinischen Friedrich-Wilhelms-Universität Bonn

vorgelegt von

Yahya Homsi

aus

Tripoli, Libanon

Bonn, Dezember 2014

Angefertigt mit der Genehmigung der Mathematisch-Naturwissenschaftlichen Fakultät der Rheinischen Friedrich-Wilhelms-Universität Bonn

1. Gutachter

Herr Prof. Dr. Thorsten Lang

2. Gutachter

Herr Prof. Dr. Sven Burgdorf

Tag der Promotion:

26.02.2015

Erscheinungsjahr:

2015

Erklärung/Declaration

Teile dieser Arbeit wurden bereits vorab veröffentlicht/Parts of this work have been published in advance:

Homsi, Y., Schloetel, J.-G., Scheffer, K. D., Schmidt, T. H., Destainville, N., Florin, L. & Lang, T. (2014). The extracellular δ-domain is essential for the formation of CD81 tetraspanin webs. *Biophysical journal* 107 (1), 100–113.

Kaczmarek, J., **Homsi, Y.**, van Üüm, J., Metzger, C., Knolle, P. A., Kolanus, W., Lang, T. & Diehl, L. (2014). Liver sinusoidal endothelial cell-mediated CD8 T cell priming depends on co-inhibitory signal integration over time. *PloS one* 9 (6), e99574.

Quast, T., Eppler, F., Semmling, V., Schild, C., **Homsi, Y.**, Levy, S., Lang, T., Kurts, C. & Kolanus, W. (2011). CD81 is essential for the formation of membrane protrusions and regulates Rac1-activation in adhesion-dependent immune cell migration. *Blood* 118 (7), 1818–1827.

Table of contents

List of illustrations

List of tables

List of abbreviations

aa	amino acid
APC	allophycocyanin
a.u.	arbitrary units
BCA	bicinchoninic acid assay
BSA	bovine serum albumin
bp	base pare
CD	cluster of differentiation
cDNA	complementary deoxyribonucleic acid
CHAPS	3-[(3-cholamidopropyl)dimethylammonio]-1-propane-sulfonic acid
CLSM	confocal laser scanning microscopy
CW-STED	continuous wave stimulated emission depletion
DAPI	4',6-diamidino-2-phenylindol
ddH_2O	double distilled water
DMEM	Dulbecco's modified eagle medium
DMSO	dimethylsulfoxide
DNA	deoxyribonucleic acid
DOC	deoxycholic acid
DPBS	Dulbecco's phosphate buffered saline
DRM	detergent resistant membrane
DZNE	*Deutsches Zentrum für Neurodegenerative Erkrankungen*
E. coli	*Escherichia coli*
EDTA	ethylenediaminetetraacetic acid
e.g.	*exemply gratia*
EGFP	enhanced green fluorescent protein
EGFR	epidermal growth factor receptor
EGTA	ethyleneglycol-*bis*(β-aminoethyl)-N,N,N',N'-tetraacetic acid
EMCCD	electron multiplying charge coupled device
EMEM	Eagle's minimal essential medium
EtOH	ethanol
etc.	*et cetera*
et al.	*et alii*
F	Faraday
FBS	fetal bovine serum
FITC	fluorescein isothiocyanate
FP	fluorescent protein
FRAP	fluorescence recovery after photobleaching
g	gram
x g	relative centrifugal force
GFP	green fluorescent protein
GPI	glycosylphosphatidylinositol
g-STED	gated stimulated emission depletion
h	hour
HEPES	4-(2-Hydroxyethyl)piperazine-1-ethanesulfonic acid
HRP	horseradish peroxidase
Hz	Hertz
i.e.	*id est*
Ig	immunoglobuline
kDa	kilo Dalton

LB	Luria-Bertani broth
M	molar
MHC	major histocompatibility complex
mg	milligram
mGFP	monomeric green fluorescent protein
min	minute
ml	millilitre
mM	millimolar
mRFP	monomeric red fluorescent protein
ms	millisecond
n	refractive index
NA	numerical aperture
nm	nanometre
ns	nanosecond
PBS	phosphate buffered saline
PCR	polymerase chain reaction
pH	potential hydrogen
PMSF	phenylmethylsulfonylfluoride
POPC	1-palmitoyl-2-oleoyl-sn-glycero-3-phosphocholine
RFP	red fluorescent protein
RIPA	radioimmunoprecipitation assay buffer
RNAi	Ribonucleic acid interference
RPMI	Roswell Park Memorial Institute
ROI	region of interest
rpm	round per minute
RT	room temperature
s	second
SD	standard deviation
SDS	sodium dodecyl sulfate
SDS-PAGE	sodium dodecyl sulfate polyacrylamide gel electrophoresis
SE	standard error
STED	stimulated emission depletion
TAE	Tris-acetate-EDTA
TBS	tris buffered saline
TBST	tris buffered saline Tween 20
TEM	tetraspanin enriched microdomain
T_g	time gated
TIRF	total internal reflection fluorescence
TMA-DPH	1-(4-trimethyl-ammonium-phenyl)-6-phenyl-1,3,5-hexatriene p-toluene-sulfonate
Tris	tris(hydroxymethyl)aminomethane
u.a.	*und andere*
V	volt
VMD	visual molecular dynamics
v/v	volume/volume
W	watt
w/v	weight/volume
3D	three dimensions
°C	degree Celsius
Ω	Ohm

1 Summary

The cell membrane is crucial for living cells; it encloses the intracellular matrix, maintains the concentration of cytosolic components, and controls the in-/outward signalling and interaction pathways. The cell membrane consists mainly of lipids and proteins. Membrane proteins are involved in essential physiological functions of the cell; in addition, they have the ability to organize, interact and assemble laterally to form clusters or platforms that are biologically important for cell function. The mechanisms underlying membrane protein organization and assembly in clusters are still not completely understood.

Tetraspanins are a family of membrane proteins exhibiting a particularly high propensity to interact with each other or with partner proteins to form so-called tetraspanin enriched microdomains (TEM) or tetraspanin webs. TEMs are involved in pathogen infections, creating entry and exit platforms, and promote different stages of cancer. Until now, the mechanism of TEM assembly is poorly understood. All tetraspanin family members share a similar molecular structure that comprises four transmembrane domains, intracellular N- and C-termini, a very short intracellular loop, a small extracellular loop (SEL), and a large extracellular loop (LEL), which is further subdivided in five helical domains, the α-, β-, γ-, δ- and ε-domain.

CD81 is an ubiquitously expressed tetraspanin; it is the best studied tetraspanin and one of the most important family members. CD81 plays a crucial role in TEM building and can form with its partner proteins large tetraspanin webs that play physiological roles in different cellular functions and regulate diverse cellular processes. Here, I examined which part of the CD81 molecule is required for protein clustering and protein organization leading to formation of tetraspanin microdomains in the plasma membrane of T cells and hepatocytes. Astonishingly, I find that the organization and assembly of large CD81 platforms are driven by the short extracellular δ-domain of CD81-LEL, independent from the strong

primary interactions with partner proteins as well as the secondary weak stabilizing interactions mediated by palmitoylation. Moreover, the δ-domain is not only necessary for protein clustering but it is also essential for platform function and viral entry. Here, a new model of tetraspanin web formation was presented, in which the δ-domain plays the key role for protein clustering, tetraspanin web organization and function. This model is based on specific interactions via the δ-domain, possibly including a protein dimerization step, to control the organization of tetraspanins into large webs and to regulate their function, instead of stable binary interactions as described by the classical view of TEM organization.

2 Zusammenfassung

Die Zellmembran ist unabdingbar für lebendige Zellen; sie umschließt die intrazelluläre Matrix, reguliert die Konzentration zytosolischer Komponenten, und kontrolliert die in-/auswärtigen Signale und Interaktionswege. Die Zellmembran besteht hauptsächlich aus Lipiden und Proteinen. Die Membranproteine sind in essenzielle physiologische Funktionen der Zelle involviert; zudem haben sie die Fähigkeit sich zu organisieren, miteinander zu interagieren und zu assemblieren, um Cluster oder Plattformen zu bilden, welche für die biologischen Funktionen der Zelle wichtig sind. Die Mechanismen, die die Proteinorganisation und die Assemblierung zu Clustern steuern, sind noch nicht vollständig verstanden.

Tetraspanine sind eine Familie der Membranproteine, die eine hohe Tendenz haben mit sich selbst und mit anderen Proteinpartnern zu interagieren, um sogenannte Tetraspanin angereicherte Microdomänen (TEM) oder Tetraspaninnetzwerke zu bilden. TEMs spielen eine Rolle bei Infektionen, u.a. indem sie bei der Bildung von Zugangs- und Ausgangsplattformen mitwirken, sowie bei der Steuerung verschiedener Krebsphasen. Aktuell ist der TEM-Bildungsmechanismus nur unzureichend aufgeklärt. Alle Tetraspaninfamilienmitglieder haben eine ähnliche molekulare Struktur gemein, die vier Transmembrandomänen, intrazelluläre N- und C-Termini, eine sehr kleine intrazelluläre Schleife, eine kleine extrazelluläre Schleife (SEL), und eine große extrazelluläre Schleife (LEL) beinhaltet. Die große extrazelluläre Schleife ist weiter in fünf helikale Domänen, die α-, β-, γ-, δ- and ε-Domäne, unterteilt.

CD81 ist ein ubiquitär exprimiertes Tetraspanin; es ist das am intensivsten untersuchte Tetraspanin und eines der wichtigsten Familienmitglieder. CD81 spielt eine wichtige Rolle bei der TEM-Bildung und kann mit anderen Proteinpartnern große Tetraspaninnetzwerke ausbilden, die physiologische Rollen in verschiedenen zellulären Funktionen spielen und diverse zelluläre Prozessen regulieren. Hier habe ich untersucht, welcher

Teil des CD81 Moleküls für die Bildung von Proteinclustern notwendig ist, die die Vorrausetzung für Tetraspanin-Mikrodomänen in der Plasmamembran von T-Zellen und Hepatozyten darstellt. Erstaunlicherweise zeigte sich, dass die Organisation der großen CD81-Plattformen von der kleinen extrazellulären δ-Domäne des CD81-LEL Moleküls gesteuert wird. Zudem ist dieser Effekt der δ-Domäne unabhängig von starken primären Interaktionen mit Proteinpartnern sowie von den schwächeren sekundären stabilisierenden Interaktionen die durch Palmitoylierung ermittelt werden. Außerdem ist die δ-Domäne nicht nur für die Bildung von Proteinclustern notwendig, sondern auch für die Funktionsfähigkeit der Plattformen und für Vireninfektionen erforderlich. In dieser Arbeit wird ein neues Modell für die Bildung von Tetraspaninnetzwerken vorgestellt, in dem die δ-Domäne eine Schlüsselrolle bei der Bildung von Proteinclustern und bei der Organisation und Funktionsfähigkeit der Tetraspaninnetzwerke spielt. Dieses Modell basiert auf spezifischen Interaktionen der δ-Domäne und einem potenziellen CD81 Dimerisierungsschritt, welche die Organisierung von Tetraspaninen innerhalb großer Netzwerke kontrollieren und deren Funktionen regulieren im Gegensatz zum klassischen Modell in dem stabile binäre Interaktionen die Organisation von TEMs dominieren.

3 Preamble

Studying molecular processes in cells has provided explanations and more accurate characterisation for many different cellular functions. Molecular biology has made major contributions to science as it describes how molecular processes control most cell activities and their growth. Cellular activities can be seen as a result of a network of molecular processes facilitated by different biological components which initiate and regulate chemical, biochemical and biological pathways in the cell. The improved understanding of molecular mechanisms controlling cellular behaviours and functions in living cells enabled researchers to unravel the mechanisms of many cellular disorders and infectious diseases providing the basis for clinical treatments. The here described work deals with a family of proteins, called tetraspanins, that are involved in different cellular processes as well as in diseases with the goal to unravel their relevance of function.

4 Introduction

4.1 The theory of the cell

The term cell in its biological meaning was introduced by Robert Hooke in 1664 after the examination of a cork sample (figure 1) using a very simple light microscope. He was able to observe small grid-like structures which he called “chambers”, or in Latin *cellula* (cell, small chamber) (Hooke, 1667).

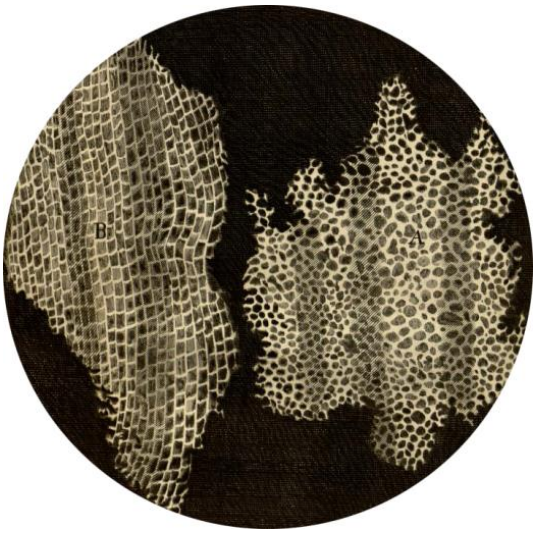

Figure 1. Cells in a cork preparation

Microscopic structure of a cork sample showing the first scientific description of the cell (adapted from Hooke, 1667).

The development of more elaborate microscopy setups enabled the visualization of cells and cell organelles in different biological preparations. In 1838, Matthias Schleiden and Theodor Schwann recognized similarities between samples from plants and animals, and established a general cell theory. The main point of their theory is that “all living things are composed of cells that have analogue structures and cells are the basic unit of the life” (Schleiden, 1838; Schwann, 1838). A few years later, Rudolf Virchow further developed this theory and described that every single cell is derived from a pre-existing cell (Virchow, 1871). Despite the very basic microscopy and laboratory techniques available at that time, the main principles postulated in this theory i.e. the cell is the smallest unit of an organism and the starting point for new cells, are valid until today.

4.2 The cell membrane

The cell membrane constitutes only 1 % of the total cell volume. Nevertheless, it is crucial for the viability of the cell because it encloses, defines and maintains the essential components of the intracellular matrix separating them from the extracellular surrounding. Besides constituting barriers separating the inside of the cell from the external world, the cell membrane also selectively controls the flux of certain ions and organic molecules in and out of the cell. This property is known as semi-permeability of the membrane. Moreover, cell membranes contain sensor proteins which allow forwarding and controlling of signal transduction into and out of the cell. Finally, many biochemical processes that are essential for the cell occur at the cell membranes (Goñi, 2014).

4.2.1 Composition of the cell membrane

Cell membranes are composed of a defined proportion of lipids and proteins (Phillips, Ursell et al., 2009). The Lipids are amphipathic molecules that form a bilayer via hydrophobic interactions, van-der-Waals forces and other secondary weak interactions, so that the lipophilic residues are oriented towards the inside and the hydrophilic residues are oriented towards the outside of the bilayer. Proteins bind to or are anchored to both leaflets of the bilayer. At the extracellular side of the membrane, some proteins and lipids additionally are linked to carbohydrates to form glycoproteins or glycolipids (Ohtsubo & Marth, 2006). The exact composition of these membrane components varies depending on cell type and function (Dupuy & Engelman, 2008).

4.2.2 Lipids of the cell membrane

The common feature of all lipids is their amphipathic character. The chemical structure typically shows a hydrophilic head combined with two hydrophobic acyl chains of different lengths (figure 2A). In aqueous surroundings, the polar head groups of the lipids and the nonpolar acyl chains tend to associate with each other in order to form the energetically

most stable structure of lipid bilayer: The polar head groups interact with each other and are oriented towards the aqueous milieu, while the nonpolar tails assemble at the inside of the bilayer. This simple principle enables cells to form a boundary for their internal contents from the external environment and in addition to form intracellular compartments. Furthermore, lipids provide the cell membrane with the ability of budding, tubulation, fission and fusion, which is essential for cell division, biological reproduction and intracellular trafficking (van Meer et al., 2008). The majority of the plasma membrane lipids constitute phospholipids followed by sphingolipids and sterols (figure 2).

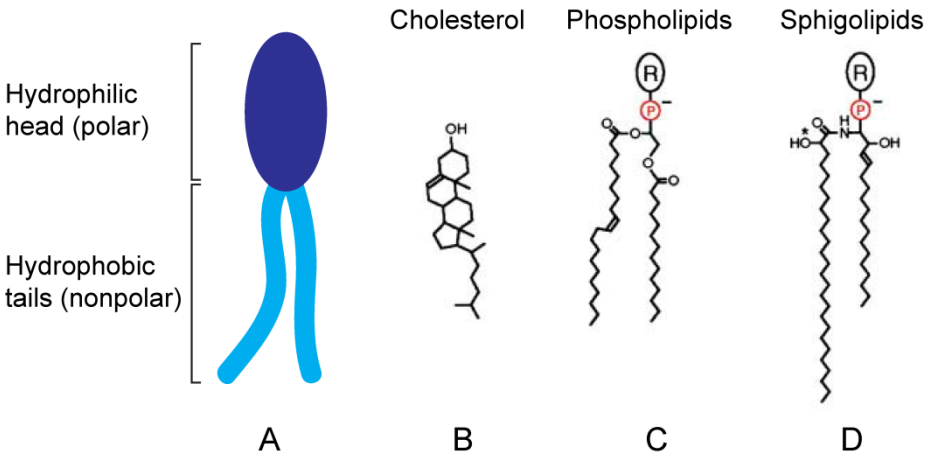

Figure 2. The major lipid classes of the plasma membrane.

Structures of different lipids of eukaryotic cells. (A) Pictogram showing the amphipathic nature of lipid molecules that have a hydrophilic headgroup (polar) and hydrophobic tails (nopolar), (B) cholesterol, (C) phospholipids based on diacylglycerol carrying two acyl chains, one of which contains a *cis* double bound. The rest R of the head group can be either serine, inositol, ethanolamine or choline. (D) Sphingolipids are based on ceramide and typically have saturated acyl chains. The rest R of the head group is generally choline (sphingomyelin) (modified from Munro, 2003).

The distribution of these lipid classes in the membrane bilayer is asymmetric; certain lipids are found predominantly in the extracellular leaflet while others are mainly located in the intracellular leaflet (van Meer et al., 2008). Likewise, glycolipids i.e. lipids bound to an oligosaccharide chain are located only in the outer lipid leaflet.

4.2.3 Membrane proteins

Membrane proteins are proteins that can integrate into or associate to the membrane. Those that can span the membrane bilayer are called transmembrane proteins. They are embedded in the lipid bilayer via their transmembrane domains and have intra- and extracellular parts protruding into the cytosol and the extracellular environment, respectively. Other proteins are attached to the inner or outer leaflet of the lipid bilayer by different anchors or linkers (figure 3). Additionally, membrane proteins can also bind to different oligosaccharide chains to from glycoproteins that are exclusively restricted to the extracellular leaflet.

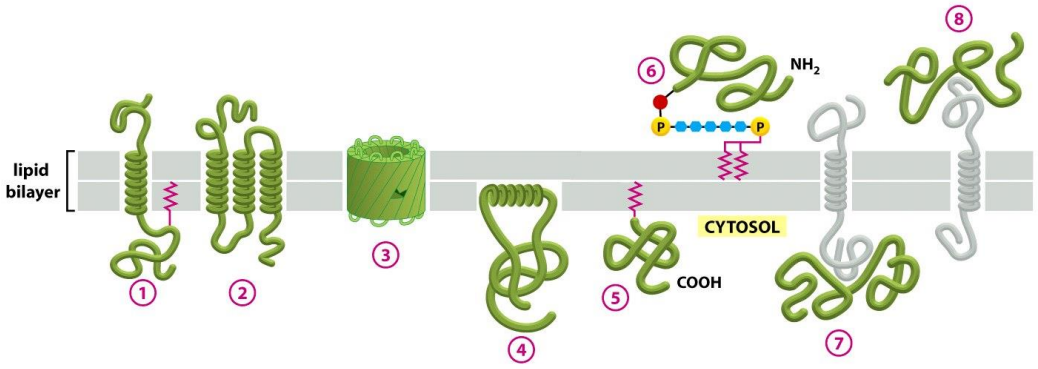

Figure 3. Different association possibilities of membrane proteins to the lipid bilayer.

Proteins associate with the lipid bilayer in various ways: some span the bilayer with a single α-helix (1), or multiple α-helices (2) as a rolled-up β-sheet (3) as in the case of channels. Other membrane proteins are integrated only into one side of the lipid bilayer by an amphipathic α-helix (4), by a covalently attached lipid chain or prenyl group (5) or via an oligosaccharide linker (6). Proteins can also bind to the membrane by noncovalent interactions with other membrane proteins (7,8) (derived from Alberts et al., 2008).

Membrane proteins play an important role in cell physiology: they function as transporters, pumps, receptors, enzymes or anchors and promote fundamental cellular processes. They convey the membrane's semi-permeability which enables the cell to maintain charge and concentration gradients in an active and highly selective way. Membrane proteins assist the transduction of signals through the cell membrane or initiate signalling cascades. Moreover, they organize the structure of the membrane and the shape of the cell, since they serve as anchors for cytoskeleton proteins

and make connections with other cells or the extracellular matrix. Finally, membrane proteins are also involved in enzymatic catalyses.

4.3 Models of the plasma membrane organization

4.3.1 The fluid mosaic model

The foundation of the current understanding of the structure and dynamics of biological membranes has been laid by the fluid mosaic model postulated by Singer and Nicolson in 1972 (Singer & Nicolson, 1972). This model was developed on the basis of a previous model of Danielli and Davson in 1935 (Danielli & Davson, 1935), who already correctly described a bilayer of amphipathic phospholipids as the basic structural element of membranes, however did not account for proteins able to incorporate into the bilayer (figure 4A).

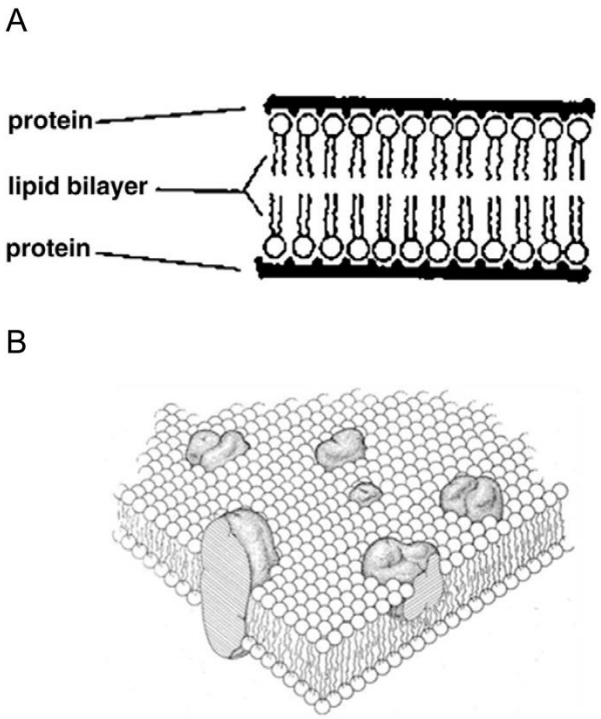

Figure 4. Models of biomembrane structures.

(A) Danielli-Davson model (1935). (B) Fluid mosaic model proposed by Singer and Nicolson in 1972. Lipids are arranged in a way that the lipophilic tails are oriented towards the middle of the lipid bilayer and the hydrophilic heads are exposed to the aqueous surrounding. The embedded proteins diffuse or rotate freely (modified from Goñi, 2014).

In 1972, Singer and Nicolson postulated a new model describing membranes as a fluid of phospholipids that contains a mosaic of dissolved proteins. Lipids and proteins are assumed to constantly diffuse laterally through the planar shape of the membrane, or rotate around an axis perpendicular to the membrane's orientation. The fluid mosaic model (figure 4B) was a revolution and a great success in the field and had incorporated a wide range of experimental observation and ideas about the proteins' and lipids' association with the membrane. This model is accepted as a general starting point in membrane biology research, and new concepts and findings have been constantly complementing and expanding the model.

4.3.2 The Picket-Fence-Model

Though the Singer and Nicolson model provided explanations for a range of questions; it was not able to explain experimental observations showed that proteins in the plasma membrane are restricted in mobility and both lipids and proteins have a 5 to 50 times smaller diffusion coefficient in the plasma membrane than in artificially reconstituted membranes or liposomes (Chang et al., 1981; Kusumi et al., 2005; Sheetz et al., 1980; Sheetz, 1983). Moreover, much evidence showed the existence of factors in the cells that confine the mobility of membrane proteins. These new findings contradicted the free diffusion theory of the fluid mosaic model. In 1980, Sheetz studied protein diffusion coefficients in erythrocyte membranes and showed that the cytoskeleton influences the lateral diffusion of membrane proteins (Sheetz et al., 1980). Hence, the picket fence model was proposed, which states that the lateral diffusion of lipids and proteins is restricted by intracellular factors such as the cytoskeleton. Complementary experiments showed that the degradation of the cytoskeleton by treatment with e.g. trypsin or latrunculin B increases the diffusion of proteins in the plasma membrane (Tsuji & Ohnishi, 1986). The picket fence model describes the cytoskeleton as a fence limiting the lateral diffusion of plasma membrane anchored proteins to the enclosed pickets (figure 5) (Kusumi et al., 2005).

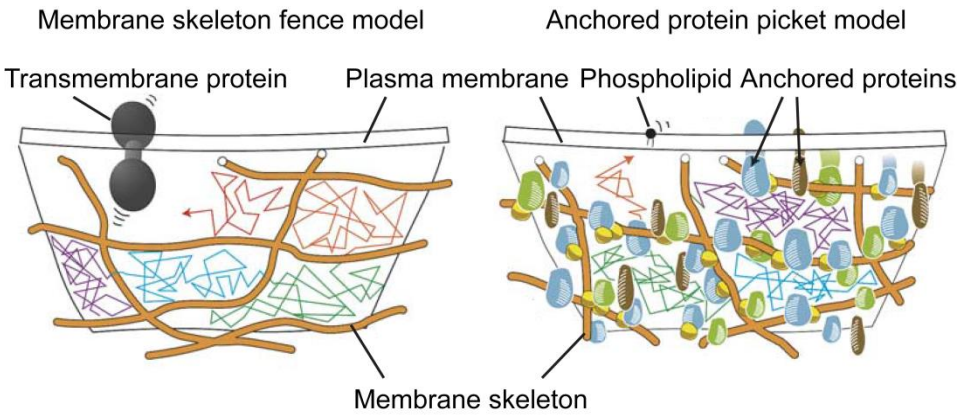

Figure 5. The picket-fence model

Cartoons depicting the picket-fence model. (Left) the membrane skeleton fence model: transmembrane proteins are confined within membrane skeleton network via physical unspecific collision of their cytoplasmic tail with the membrane skeleton. Trajectory of single transmembrane protein crossing different areas formed by membrane skeleton fence network is shown in different colours. (Right) the membrane skeleton anchored transmembrane proteins picket model: transmembrane proteins anchor to and line up along the membrane skeleton fence and act as pickets creating barriers that affect the free diffusion of phospholipids of the plasma membrane. Tracks of phospholipid within confined areas created by cytoskeleton (fence) and anchored proteins (pickets) are shown in different colours (modified from Kusumi et al., 2005).

4.3.3 The membrane raft model

The picket fence model assumes that the formation of protein domains is organized by membrane protein/cytoskeleton interactions. Parallel studies observed an asymmetrical lipid compartmentalization in the plasma membrane of polarized cells in form of lipid microdomains. In the apical membrane, lipid rafts composed of sphingomyelin and cholesterol that clustered into platforms were observed. These lipid rafts appeared to be resistant to detergent treatment, and were enriched with specific raft proteins (Simons & Ikonen, 1997). The mechanism of the membrane raft model is based on the physico-chemical properties of lipids which tend to form ordered phases or platforms - so-called lipid rafts. These rafts allow the recruitment of specific proteins (figure 6). Later, it was shown that the chemical composition of the outer monolayer of the cell membrane differs from those of the cytoplasmic monolayer inducing the propensity of phase separation (Simons & Gerl, 2010).

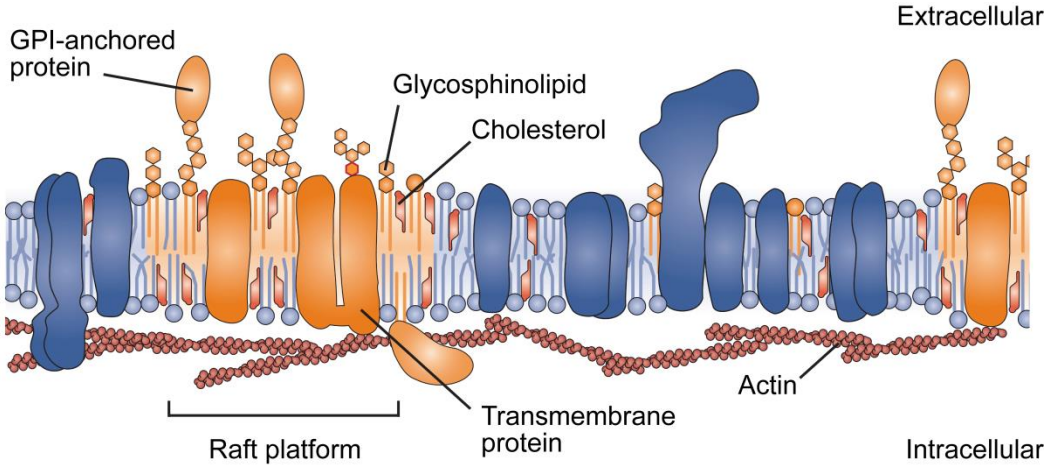

Figure 6. Membrane raft platform

Membrane rafts comprise cholesterols and sphingolipids such as glycosphigolipids as well as membrane proteins. The rafts are fluctuating platforms that assemble via lipid-lipid, lipid-protein and protein-protein interactions and may play a role in signaling and membrane trafficking (modified from Simons & Gerl, 2010).

The detection of lipid rafts became a major point of debate because the biochemical methods used for preparing detergent resistant membranes (DRM) are prone to artefacts (Munro, 2003). Later, lipid rafts were defined as highly dynamic heterogeneous microdomains of 10 – 200 nm in size, which are rich in sphingomyelin and sterols and serve to compartmentalize cellular processes (Simons & Gerl, 2010). Currently, the transient nature of rafts is highlighted by platforms stabilized through protein-protein and protein-lipid interactions (Pike, 2006).

4.3.4 The protein cluster model

The picket fence model suggests that proteins of similar structure and comparable steric hindrance also show a comparable diffusion and similar domain localization. In contrast, the membrane raft model assumes the hydrophobic lipid-lipid and lipid-protein interactions to be responsible for membrane protein organization in lipid domains. Therefore, proteins which have similar lipid anchors or transmembrane domains and tertiary structures should be confined to the same domains of the plasma membrane. Surprisingly, experimental observations show contradictory results.

Sieber et al. showed that protein isoforms with identical transmembrane domains and similar structures are localized in different membrane protein clusters (Sieber et al., 2006). This observation cannot be reconciled with one of the models described so far. Moreover, several membrane proteins isoforms sharing highly similar features were not found in the same membrane region (Kai et al., 2006; Low et al., 2006; Uhles et al., 2003; Zacharias et al., 2002). In addition, the modification of a single small protein motif can lead to distinct segregation of the protein into different protein clusters (Sieber et al., 2006). This difference in clustering upon such subtle changes can be explained by the presence of highly specific protein-protein interactions. The protein cluster model is based on these specific protein-protein interactions and how they influence protein clustering. Syntaxin 1A is a model protein for clustering driven by protein-protein interactions (Sieber et al., 2007). In this case, cluster size and stability are determined by an equilibrium between attractive forces (between protein monomers) and accumulation repulsion (upon cluster growth) (figure 7) (Sieber et al., 2007).

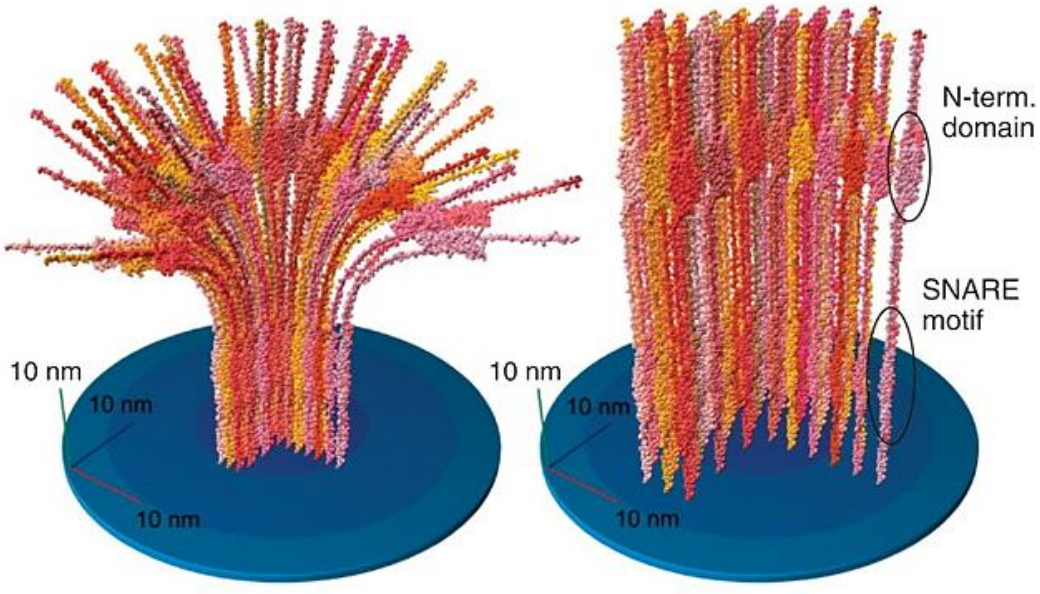

Figure 7. Protein cluster model of syntaxin 1A

Protein clustering driven by specific protein-protein interactions is reached after balancing attractive and repulsive forces. Charge and/or steric crowding may play an important role in the determination of cluster size and stability (derived from Sieber et al., 2007).

The protein cluster model contradicts neither the picket fence model nor the membrane raft model, but it offers new ways to explain observations and answer questions that could not be addressed with the previous models.

4.4 Tetraspanin protein family

Tetraspanins constitute a large family of small surface membrane proteins (~20 – 30 kDa) (Hemler, 2008) which comprise four transmembrane domains and are present in a high copy number in all cell and tissue types. Generally, tetraspanins are expressed in nearly all organisms including plants, fungi and humans, in which 33 tetraspanin members have been identified (Charrin et al., 2009; Huang et al., 2005).

Tetraspanins were first cloned and studied in the early 1990ies. The most important feature of this protein family is the high tendency to interact laterally with one another or with multiple molecular partners in a dynamic assembly process forming tetraspanin webs or so-called tetraspanin-enriched microdomains (TEMs) (Berditchevski & Odintsova, 2007; Berditchevski & Rubinstein, 2013; Charrin et al., 2009; Hemler, 2005, 2008; Homsi et al., 2014; Levy & Shoham, 2005a; Rubinstein et al., 1996; Yáñez-Mó et al., 2009). Therefore, TEMs result from the tetraspanins' ability to associate in high stoichiometry with integrins, members of the immunoglobuline (Ig) superfamily and membrane receptors (Berditchevski & Rubinstein, 2013; Hemler, 2005; Homsi et al., 2014; Rubinstein et al., 1996).

TEMs play an important role in a diverse range of cellular processes and activities, including cell adhesion, morphology, motility, proliferation, signal-transduction, intercellular communication, cell-cell fusion, intracellular signalling, endocytic trafficking as well as in immune system, malignancy and host-pathogen interactions (Berditchevski & Rubinstein, 2013; Homsi et al., 2014; Wright et al., 2004; Yáñez-Mó et al., 2009; Zhang & Huang, 2012). Because of their involvement in infectious and non-infectious diseases, the immune system and malignancy, TEMs have

been gaining in prominence and become more and are becoming more and more important targets in therapeutic strategies (Hemler, 2008, 2013; Homsi et al., 2014).

4.4.1 Tetraspanins involvement in infectious diseases

Apart from their role in a wide range of biological and cellular processes as well as in promoting different stages of cancer, tetraspanins are also known to have a prominent roles in the pathology of infectious diseases such as diphtheria and malaria (Martin et al., 2005; van Spriel, Annemiek B & Figdor, 2010). Recent reports indicate that tetraspanins are not only involved in infections by various microbes but also that tetraspanins play an important role in viral infections and parasites (table 1). Tetraspanins associate selectively with specific viruses and affect multiple stages of infectivity, from the initial cellular attachment to final viral particles release (Martin et al., 2005).

Tetraspanin	Alternative names	Tissue distribution	Involved in infectious disease
CD9	Tspan 29, BA2, p24, GIG2, MIC3, MRP-1, BTCC-1, DRAP-27	Broad	Linked with HIV-1, FIV, CDV. Modulates Diphtheria toxin binding
CD37	Tspan 26, Gp40e52	Immune system (B and T cells, monocytes, macrophages, granulocytes, immature DC)	Regulates immune response to C. albicans
CD53	Tspan 25, MOX44	Immune system (B,T and NK cells, monocytes, macrophages, granulocytes, DC)	Human CD53 deficiency linked to recurrent infections. Role in HIV-1 egress
CD63	Tspan 30, MEL1, ME491, granulophysin, LAMP3, OMA81H, MLA1, NGA, LIMP	Broad	Roles in HIV-1 entry and egress, HTLV mediated syncytium formation, endocytosis of HPV16.
CD81	Tspan 28, TAPA-1, S5.7	Broad	Receptor for HCV. Role in HIV-1, HTLV. Binds to P. falciparum and P. yoelii.
CD82	Tspan 27, Kangai1, R2, 4F9, C33, IA4, ST6, GR15, KAI1, SAR2	Broad	Role in HIV-1 and HTLV assembly.
CD151	Tspan 24, PETA3, SFA1, gp27	Broad	Involved in endocytosis of HPV16, role in porcine RRSV.
Uroplakin Ia	Tspan 21, UP1A, UPIA, UPKA, MGC14388	Bladder epithelium	Binds FimH protein in E. coli during urinary tract infection.
Uroplakin Ib	Tspan 20, UPIB, UPK1	Bladder epithelium	Binds FimH protein in E. coli during urinary tract infection.

Table 1. Different tetraspanin expression profiles with their suggested involvement in the pathogenesis of infectious diseases.

Viruses' abbreviations: Human immunodeficiency virus (HIV), feline immunodeficiency virus (FIV), canine distemper virus (CDV), human T cell leukemia virus (HTLV), human papillomavirus type 16 (HPV16), Hepatitis C virus (HCV), porcine reproductive and respiratory syndrome virus (porcine RRSV) (adapted from van Spriel, Annemiek B & Figdor, 2010).

4.4.2 TEM formation and classification of the underlying tetraspanin interactions

As mentioned above, the most important feature of tetraspanin proteins is their ability to associate laterally with each other and with other partner proteins with high stoichiometry to form tetraspanin webs or TEMs

(Charrin et al., 2001; Hemler, 2003; Stipp, Kolesnikova et al., 2001; Stipp, Orlicky et al., 2001). More than 100 different tetraspanin interaction partners have been identified to associate with one or more tetraspanins (Hemler, 2008). The most important tetraspanin-associated proteins include membrane-bound ligands, integrins, cadherins, different immunoglobulin superfamily members (e.g. EWI-2, EWI-F, CD4, CD8, MHC class I and II, etc.), proteoglycans, complement-regulatory proteins, signalling receptors, growth factors (e.g. EGFR) and others (table 2) (Berditchevski & Rubinstein, 2013; Hemler, 2003, 2008; Yáñez-Mó et al., 2009). These interactions form the basis for the involvement of TEMs in so many different cellular functions and their major role in diverse cellular processes including cell signaling, adhesion, proliferation, morphology, motility, biosynthesis, in the immune system, pathogen infection, malignancy, infectious and non-infectious diseases. Therefore, tetraspanins are considered as master organizers of the plasma membrane (Cambi & Lidke; Hemler, 2005). This wide implication of TEMs in both physiological and pathological processes makes them an important topic in research.

Partner	Associated tetraspanins	Partner	Associated tetraspanins
α3β1, integrin	CD151, CD9	**Dectin-1**	CD63, CD37
α7 β1 integrin	CD151, CD9	**UroplakinII**	UPIa
α6 β1 integrin	CD151, CD9	**UroplakinIII**	UPIb
α6 β4 integrin	CD151	**CD2**	CD9,CD53
α4 β1 integrin	CD81	**CD3**	CD9, CD81, CD82
αL β2 integrin	CD82, CD63	**CD4**	CD81,CD82
αM β2 integrin	CD63	**CD5**	CD9
α1 β1 integrin	CD9	**CD8**	CD81,CD82
α2 β1 integrin	CD9, CD151	**CD19**	CD81
α5 β1 integrin	CD9,CD151	**CD20**	CD53,CD81, CD82
αv β5 integrin	CD81	**CD21**	CD81
gpIIb-IIIa	CD9	**CD36**	CD9
CD41/gpIIb	CD9	**CD38**	CD9
CD42/gpIb	CD9	**CD46**	CD9
CD44	CD9, D6.1A/CO-029/Tspan8	**CD47**	CD9
GPVI	Tspan9, CD151	**Leu 13**	CD81
Syndecan	CD9	**BCR/IgM**	CD9
EWI-2/ PGRL/CD316	CD9/CD81	**MHC-I**	CD82,CD81, CD53
EWI-F/CD9P-1/FPRP/CD315	CD9/CD81	**MHC-II**	CD53,CD81, CD82, CD37
ICAM-1/CD54	CD9	**EGFR**	CD82
VCAM-1/CD106	CD151	**GPCR56**	CD9, CD81
EP-CAM/GA733-2	CD9, D6.1A/CO-029/Tspan8	**BAI2**	CD9
Lu/B-CAM/CD239	CD9	**cKit/CD117**	CD9, CD63, CD81
GA733-1/TACSTD2	CD9	**Pro-TGFα**	CD9
Claudin-7	D6.1A/CO-029/Tspan8	**Pro-HB-EGF**	CD9
E-cadherin	CD151	**ADAM10/CD156c**	CD9
L6	CD151	**MT1-MMP**	CD151, CD63, CD9,CD81, Tspan12

Table 2. Overview of tetraspanin-associated transmembrane partner proteins (adapted from Yáñez-Mó et al., 2009).

TEMs were characterized by immunoelectron microscopy as individual microdomains of ~0.2 μm^2 in size which are separated from each other by 0.6 – 0.7 µm (Nydegger et al., 2006). To date, TEM formation and organization have been studied using mostly classical biochemical methods such as immunoprecipitation and isopycnic centrifugation. Immuoprecipitated tetraspanin complexes collected after lysing cells with detergents of different strength have revealed diverse interaction classes of varying strength that are involved in tetraspanin web formation (figure 8) (Hemler, 2005, 2008; Homsi et al., 2014).

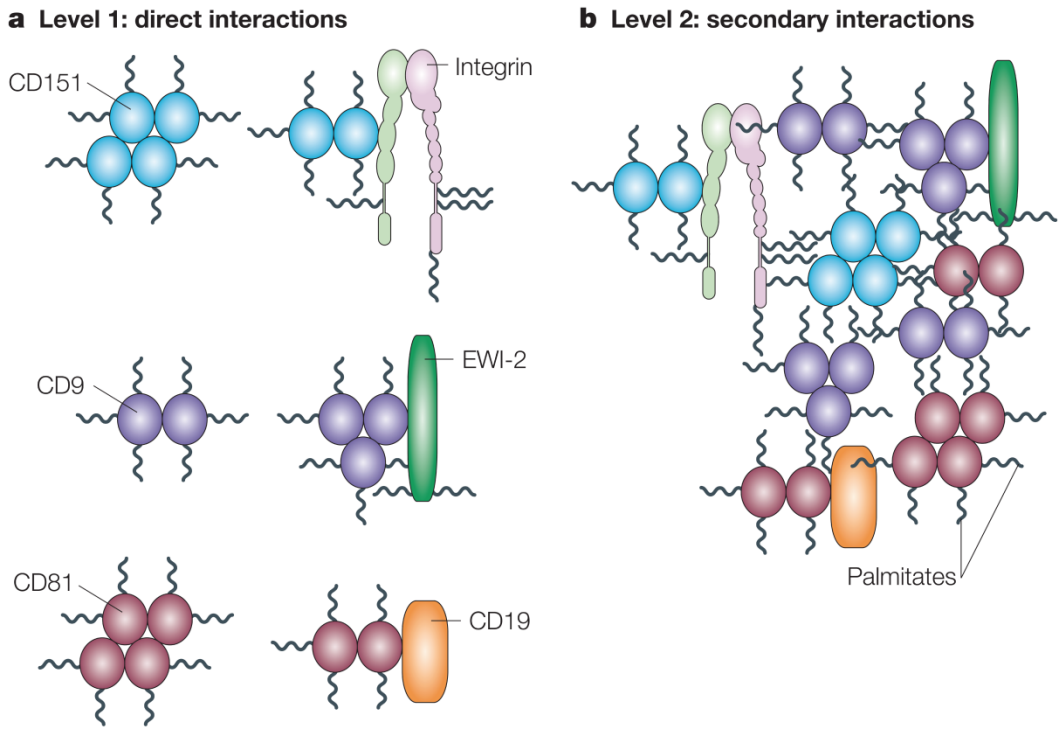

Figure 8. Multistep interactions of tetraspanins.

(a) Level 1 or primary interaction: this interaction is direct and in most cases resistant to stringent detergent treatment. This kind of interaction includes homodimerizations and hetero-associations with other tetraspanin partner proteins such as integrins, EWI proteins, CD19 and others. (b) Level 2 or secondary interaction: is the result of a network of secondary interactions that can be stabilized by palmitoylation of both tetraspanins tetraspanin-associated partner proteins and other weak interactions. These interactions are generally maintained after treatment with mild detergents e.g. CHAPS (derived from Hemler, 2005).

Primary interactions or level 1 interactions are the result of direct binding with high stoichiometry between tetraspanins and non-tetraspanin partner proteins. In addition, tetraspanin homo-dimerization or homo-oligomerization interactions are assumed to be included in this interaction level. These primary protein complexes are resistant to harsh detergents such as Triton X-100 or digitonin (Boucheix & Rubinstein, 2001; Hemler, 2003, 2008). TEMs are further stabilized and assembled through a network of secondary interactions. These secondary interactions define the level 2 interactions that allow different tetraspanins to associate with each other and recruit different tetraspanin partners together into complexes to form large tetraspanin webs. This level of interaction is not resistant to harsh detergents, but can be maintained using mild detergents

such as Brij97 or CHAPS (Charrin et al., 2009; Hemler, 2008; Homsi et al., 2014; Yáñez-Mó et al., 2009). The stability of tetraspanin complexes is further enhanced by protein palmitoylation (Charrin et al., 2002; Hemler, 2008; Yang et al., 2002). Palmitoylation was described to stabilize tetraspanin-tetraspanin interactions and palmitoylation deficient mutants showed impaired binding of CD81 to the tetraspanin CD9 and one of its binding partners EWI-2 (Delandre et al., 2009; Stipp, Kolesnikova et al., 2001), as well as impaired binding of CD151 to other tetraspanins (CD9, CD81, CD63) (Berditchevski et al., 2002). In contrast, the association of CD151 and $\alpha 3\beta 1$ integrin was not affected in non-palmitoylated mutants (Yang et al., 2002). Similarly, inhibition of palmitoylation through treatment with specific drugs does not disrupt pre-existing interactions (Berditchevski et al., 2002; Stipp et al., 2003). Therefore, role of palmitoylation in the TEM formation is not completely understood, but it appears to be mainly important for complex stabilization. Additionally, treatment with mild detergents has led to formation of incomplete solubilized tetraspanin complexes which separate into the low-density fractions of sucrose gradients. TEM complexes have shown interactions with lipids like gangliosides and cholesterols (Claas et al., 2001). Such associations with lipids may be explained by the lipid raft model (see 4.3.3). However, TEMs were shown to have a protein composition different from those of lipid rafts, which indicates a distinct nature (Barreiro et al., 2008; Charrin et al., 2009; Claas et al., 2001; Espenel et al., 2008; Hemler, 2005; Le Naour et al., 2006; Min et al., 2006). Hence, the role of lipids in the TEM assembly is still under debate, but they may be important for stabilization of tetraspanin interactions during tetraspanin web building (Charrin et al., 2009).

4.4.3 Dynamic model of tetraspanin web assembly

The classical research strategies in the tetraspanin field were based exclusively on biochemical approaches that deliver a primarily static image of the TEM formation process and do not address the behaviour in a natural environment. Recently, the development of microscopy

techniques has allowed studying TEMs in the intact membrane of living cells, revealing biophysical characteristics of microdomains including size, diffusion, molecular compositions and interactions. Using modern microscopy methods such as total internal reflection fluorescence (TIRF) microscopy, fluorescence recovery after photobleaching (FRAP) and fluorescence correlation spectroscopy (FCS), it was possible to track single tetraspanin molecules and to study molecular interactions between TEM components over time in a dynamic and more realistic approach. Single molecule tracking has revealed two ways of molecular interaction which differ in their dynamics. Molecular diffusion is transiently slowed down when the molecule enters tetraspanin enriched platforms. The platforms are in permanent exchange with the rest of the membrane and have a constant shape and location. These new observations have demonstrated the dynamic interactions of tetraspanins within the tetraspanin webs (Barreiro et al., 2008; Espenel et al., 2008; Rocha-Perugini et al., 2013). In contrast to the classical view of tetraspanin interactions, another model of TEM building was proposed which takes into account the dynamic behaviour of tetraspanins to describe the molecular assembly of TEMs (figure 9) (Charrin et al., 2009).

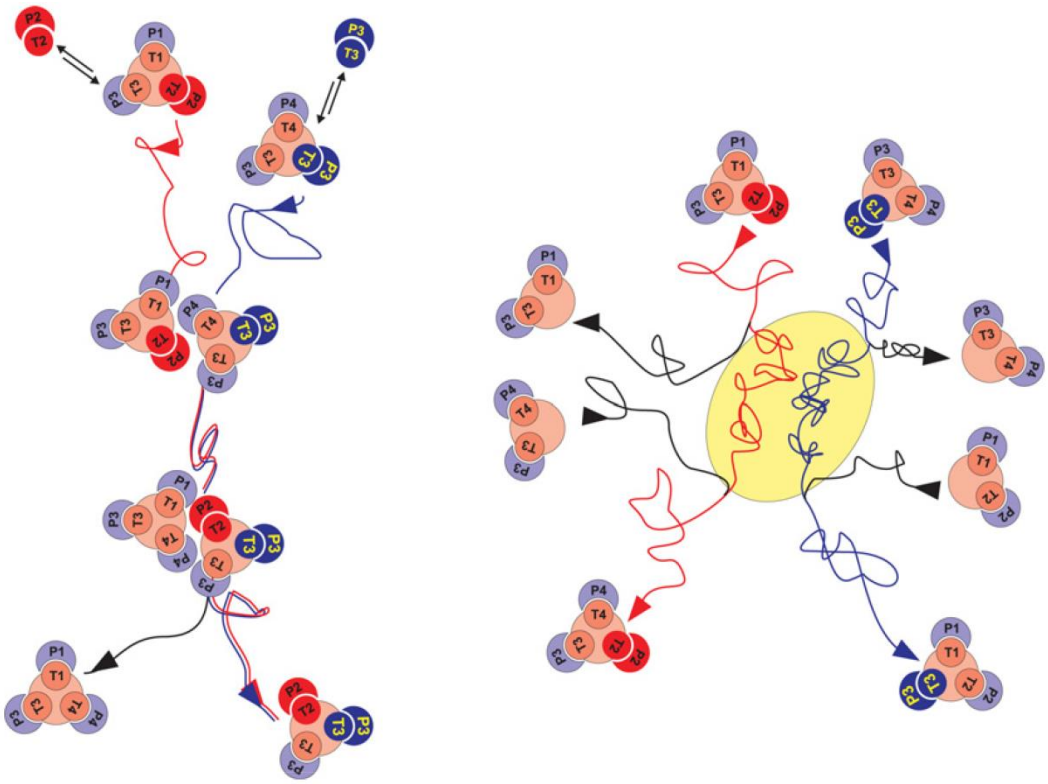

Figure 9. Model of tetraspanin web assembly in a dynamic view

This model is based on the multistep tetraspanin interactions revealed by the biochemical analysis of tetraspanin webs and supplemented with the results of recent analyses of tetraspanin dynamics. The figure shows two tetraspanin – partner pairs and their corresponding movement traces which are labelled in red and blue. The left part of the figure shows a basal level of tetraspanin interactions in the plasma membrane, where small clusters of specifically associated tetraspanin – partner molecules (T_1 – P_1, T_2 – P_2, etc.) diffuse, frequently interact and exchange some of their constituents with other clusters. The right part illustrates cluster behaviours upon particular stimulations. Tetraspanins show a confined movement within a particular area in the plasma membrane (referring to TEMs), in which more stable interactions take place. This model describes a dynamic view based on single molecule tracking data, but other models are possible (derived from Charrin et al., 2009).

Thus, while studies of tetraspanin multilevel interactions and tetraspanin dynamics have explained the basis of TEM formation, the underlying mechanism that drives the association of the wide variety of different proteins and proteins complexes into large tetraspanin webs has remained unclear.

4.5 The tetraspanin CD81

Tetraspanins protrude only 4 – 5 nm out of the plasma membrane (Hemler, 2005, 2008; Kitadokoro et al., 2001; Min et al., 2006). Therefore,

they are hardly accessible for biochemical and immunological methods (Hemler, 2005), making it difficult to unravel their structural features. One of the best studied tetraspanins is CD81 (cluster of differentiation 81), from which a 3D structure has been thoroughly studied and predicted using both computational and crystallographic methods (Seigneuret, 2006).

4.5.1 CD81 topology and structure specificities

CD81 or tetraspanin 28 (26 kDa) contains like all other tetraspanin family members, four transmembrane domains (τ1 – τ4) and two extracellular loops. The small extracellular loop (SEL) and the large extracellular loop (LEL) are flanked by the transmembrane regions τ1/τ2 and τ3/τ4, respectively (figure 10). The LEL contains a cysteine-cysteine-glycine (CCG) motif which is common to all tetraspanin proteins and ensures the formation of disulfide bridges with other cysteine residues of the LEL. The formation of disulfide bridges is important for the correct conformation and maintenance of the secondary structure of the LEL (Kitadokoro et al., 2001; Seigneuret, 2006). The intracellular compartments comprise a very short intracellular loop between τ2/τ3 as well as small N-terminal and C-terminal cytoplasmic tails that harbour two palmitoylation sites each. This palmitoylation may be involved in protein cluster stabilization (see below).

The large extracellular loop is further subdivided into five (α, β, γ, δ and ε) helical domains, of which the α, β and ε domains constitute the constant region that appears to play a crucial role in tetraspanin dimerization (Kitadokoro et al., 2001; Seigneuret, 2006). The γ and δ domains form the variable region which shows marked conformational fluctuations and may play a role in protein-protein interactions (Hemler, 2003; Kitadokoro et al., 2002; Seigneuret, 2006; Stipp et al., 2003). The crystallographic structure of the water soluble CD81 LEL was solved by Kitadokoro in 2001; the five helical domains form a mushroom-like structure that is stabilized by two disulfide bridges (figure 11) (Kitadokoro et al., 2001).

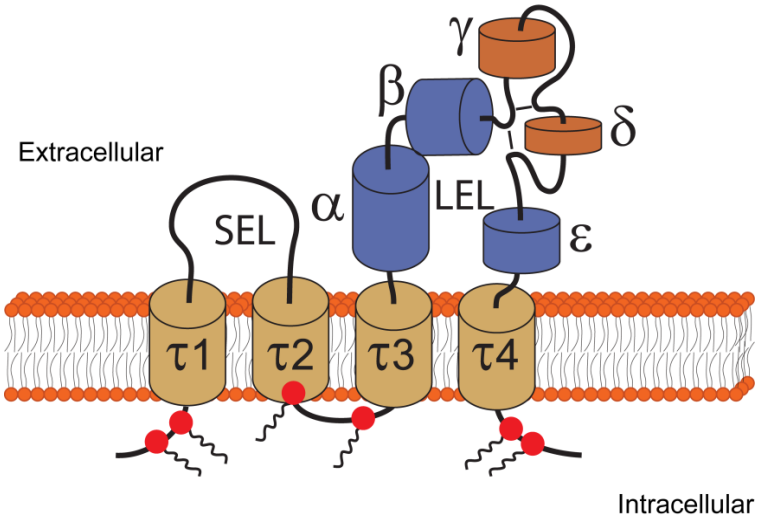

Figure 10. Pictogram of the tetraspanin protein CD81 and its intramolecular domains

CD81 is membrane embedded via its four transmembrane domains (τ1 – τ4); SEL is the small extracellular loop; LEL is the large extracellular loop subdivided in five helical domains (α, β, γ, δ and ε), where the blue colored (α, β and ε) domains constitute the constant region and the orange colored γ and δ domains constitute the variable region; the two disulfide bridges are shown as thin black dashes within the LEL; the red dots with acyl chains show the palmitoylation sites in the intracellular segments of the protein (modified from Homsi et al., 2014).

Based on Kitadokoro's crystallographic data, Seigneuret employed molecular modeling to predict the complete 3D structure of CD81 (Seigneuret, 2006; for more detailed domain structures see figure 23). The four transmembrane domains are closely packed and appear as a twisted left-handed coiled coil bundle. The transmembrane regions τ3 and τ4 span the membrane bilayer and extend towards the extracellular part in continuity with the anti-parallel α and ε helices that form the stalk of the LEL. The β, γ and δ helices form the head subdomain, which is inserted within the stalk subdomain sequence and located on its top giving the whole CD81 molecule a compact rod shape structure. Within the head subdomain, the δ-domain is particularly exposed to the extracellular space (figure 11) (Homsi et al., 2014; Kitadokoro et al., 2001; Kitadokoro et al., 2002).

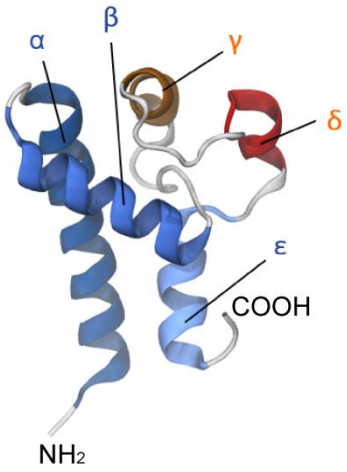

Figure 11. Crystal structure of the human CD81-LEL

The view shows at a realistic scale the orientation of the head (constituted by β, γ and δ domains) and the stalk (constituted by α and ε domains) of the mushroom like structure of the LEL. The structure of the molecule highlights the exposed orientation of the δ domain (red) to outside of the molecule (modified from a figure kindly provided by Dr. Thomas Schmidt and based on Kitadokoro et al., 2001).

Most of the known antibodies raised against CD81 target epitopes within the LEL variable domain i.e. the γ- and δ-helices of the LEL. Both in solution and in hexagonal and monoclinic crystals the LEL shows a high degree of structural flexibility. It is assumed that the structural hyper-flexibility of this region reflects its importance for TEM building and function (Kitadokoro et al., 2002; Seigneuret et al., 2001; Seigneuret, 2006). In addition, the variable domain contains nearly all known tetraspanin protein-protein interaction sites and defines their classes and functions (DeSalle et al., 2010; Homsi et al., 2014; Seigneuret et al., 2001; Seigneuret, 2006; Stipp et al., 2003). The transmembrane domains are highly similar among members of the tetraspanin family, and are involved in inter- and intra-molecular interactions (Charrin et al., 2003; Kovalenko et al., 2005; Montpellier et al., 2011). Interestingly, the tetraspanin transmembrane domains τ1, τ3 and τ4 also contain polar residues that might play a role in transmembrane domain packing (Stipp et al., 2003).

Little is known about the small extracellular loop. It may assist in maintaining the correct conformation of the LEL, and it is required for the

optimal surface expression of CD81, but not for protein-protein binding and interactions (Masciopinto et al., 2001). The SEL has a β-strand secondary structure and it may interact with residues in the constant domain of the LEL (Seigneuret et al., 2001; Seigneuret, 2006). The intracellular N- and C-terminal regions are unstructured and have a disordered conformation (Seigneuret, 2006). In addition, the intracellular segments of CD81 provide palmitoylation sites that may be important for TEM stabilization (Hemler, 2005). Moreover, the C-terminus ensures binding to ezrin-radixin-moesin (ERM) proteins, the cytoskeleton (Coffey et al., 2009; Sala-Valdés et al., 2006; Stipp et al., 2003) and signalling proteins (Stipp et al., 2003) and also regulates molecule dynamics and pathogen receptor activity (Harris et al., 2013).

4.5.2 Role of CD81 and CD81 enriched TEMs in pathogen infection

CD81 was initially discovered on activated B- and T-cells as a target of an antiproliferative antibody (Oren et al., 1990). In the last 20 years, CD81 has been shown to be essential for different biological and physiological processes, including immune responses (Levy & Shoham, 2005b), protein biosynthesis (Shoham et al., 2003), brain development (Geisert et al., 2002), retinal pigment epithelium development (Pan et al., 2011), fertility (Rubinstein et al., 2006) and others.

In addition to its physiological functions, CD81 plays a clinically significant role as a receptor for pathogen entry, e.g. for the hepatitis C virus (HCV) (Pileri et al., 1998), the malaria *Plasmodium* parasite (see also table 1) (Silvie et al., 2003) and *Listeria monocytogenes* (Tham et al., 2010). Moreover, CD81 enriched TEMs are crucial for entry of the human papilloma virus (HPV) (Homsi et al., 2014). Therefore, they provide entry and/or exit platforms for HPV (Spoden et al., 2008), and human immunodeficiency virus (HIV) (Krementsov et al., 2010; Nydegger et al., 2006) and other pathogens (Monk & Partridge, 2012; van Spriel, Annemiek B & Figdor, 2010).

Recently, two pathways of internalization with pathogens have been described. Pathogens can directly associate with CD81. One of the first observations of CD81/pathogen association was shown for HCV (Pileri et al., 1998), where CD81 and at least three receptors as human scavenger receptor SR-BI/Clas1 (Scarselli et al., 2002), tight junction molecules Claudin-1 (CLDN-1) (Evans et al., 2007) and occludin (Liu et al., 2009) are the essential receptors that mediate HCV entry (Burlone & Budkowska, 2009). The interaction between CD81 and HCV is based on CD81 LEL binding to HCV E2 glycoprotein (Pileri et al., 1998). Moreover, this interaction is specific for CD81; other tetraspanin proteins such as CD9, CD63 and CD151 do not show any interaction with HCV E2 glycoprotein (Flint et al., 1999). The functional role of the CD81 interaction with HCV in HCV entry was further experimentally confirmed. It was shown that non-permissive human cell lines such HepG2 and HH29, which do not express endogenous CD81, become susceptible to HCV infection upon ectopical expression of CD81 (Bartosch et al., 2003; Cormier et al., 2004; Lavillette et al., 2007; Zhang et al., 2004). Conversly, CD81 monoclonal antibodies and a soluble form of CD81 LEL inhibited HCVpp (HCV pseudoparticles) and HCVcc (HCV in cell culture) infectivity *in vitro* (Bartosch et al., 2003, 2003; Cormier et al., 2004) and HCV infection *in vivo* (Meuleman & Leroux-Roels, 2008). The current description of the HCV entry mechanism suggests that HCV cell entry is a multi-step process which requires direct binding of HCV to a couple of membrane receptors including CD81. These successive interactions, which do not require the formation of TEM, facilitate virus uptake via clathrin-mediated endocytosis into pH-sensitive early endosomes. In conclusion, the incorporation of CD81 into TEM is not essential for HCV entry (Rocha-Perugini et al., 2009).

A second pathogen entry mechanism has been proposed that requires the association of tetraspanin proteins (including CD81) into TEMs for successful pathogen uptake. It has been shown that CD81 is required for infection with *Plasmodium* sporozoites, but here no evidence proves that a direct interaction with the pathogen takes place. This data suggests that

CD81 does not act as a receptor, but rather associates into TEMs that constitute a novel type of membrane microdomain which can be used for pathogen entry (Silvie et al., 2006). A similar pathogen entry mechanism was proposed for HIV infection, where the virus particles accumulate at surface TEMs containing CD81 that can function as gateways for the pathogen (Nydegger et al., 2006). The actual entry of HIV is clathrin-independent. Therefore, CD81 may directly associate with CD4, integrins and EWI-2 which could influence the surface organization of HIV receptor and virus-cell adhesion. Then, both CD81 and EWI-2 bind to F-actin by ERMs and other factors. In this way the TEMs facilitate pathogen entry through actin cytoskeleton activity (Rocha-Perugini et al., 2014). A similar mechanism, in which TEMs act as pathogen entry gateway, has been observed for HPV. The experimental data suggest that HPV entry does not occur in a clathrin- and caveolin-dependent manner, but rather via specific TEM-organizations containing CD151, CD81 and other tetraspanins (Scheffer et al., 2013; Spoden et al., 2008). Therefore, TEMs are essential for mediating HPV uptake and constitute a novel route for pathogen entry (Spoden et al., 2008). In conclusion, CD81 and CD81 assembled into TEMs play a fundamental role in pathogen entry as well as in other biological processes which makes the characterization of CD81 functional domains a very important issue since they are essential for the relevant CD81 interactions and drive integration of CD81 into TEMs.

5 Aims of the work

Tetraspanins have fascinated researchers due to their ability to associate with each other and with different membrane protein partners to form supra-molecular assemblies, so-called TEMs or webs. The exact mechanism of TEM building and tetraspanin assembly is still not completely understood. Since the identification of this protein family, tetraspanins were studied and isolated using mainly static biochemical approaches such as immunoprecipitation and density gradient centrifugation. However, these methods are limited to a specific observation timepoint and cannot deliver information about the dynamics of TEM formation or behavior; moreover, they yield no information on TEM size, shape or number.

Applying modern microscopy techniques to living cells and plasma membrane sheet preparations, this work focused on clustering of the tetraspanins. In particular, CD81 was studied since the CD81 molecule is the most extensively examined tetraspanin and its 3D structure has been solved, providing a basis for structural deletions. Since all tetraspanins share a common structure, I believed that studying the clustering of CD81 would be a paradigm to reveal the fundamental principles of TEM building mechanism.

The major aim of this work was the characterization of the protein domains important for CD81 clustering and enrichment into TEM to be studied in both static (STED microscopy and immunoprecipitation) and dynamic approaches (TIRF and FRAP microscopy).

Further, I aimed to identify the functional role of the clustering behavior mediated by the related domains of the CD81 molecule. In this context, the effect of TEMs assembly on infection with different pathogens was also to be tested.

The insights in the clustering mechanism and functional roles of CD81 should help us to introduce a new general model for tetraspanin assembly and TEM building.

6 Materials and Methods

6.1 Materials

If not stated otherwise, the chemicals and reagents used for this work are products of the following companies: Carl Roth (Karlsruhe, Germany), Merck (Darmstadt, Germany), Sigma-Aldrich (Hamburg, Germany), Biochrom (Berlin, Germany), Promega (Madison, WI, USA), Fermentas (St. Leon-Rot, Germany), NEB (UK), Bio-Rad (Germany), Machery-Nagel (Düren, Germany). All media, buffers and solutions were prepared using autoclaved deionized water if necessary.

6.1.1 Small instruments

6.1.1.1 UV-Vis spectrophotometer

NanoDrop2000 (Thermo Fisher Scientific, Waltham, MA, USA) was used for DNA concentration measurements

6.1.1.2 Microplate reader

Infinite® 200 PRO multimode microplate reader (Tecan, Maennedorf, Switzerland)

6.1.1.3 Sonifier

Sonopuls HD 2070, 70 W (Bandelin, Berlin, Germany)

6.1.1.4 SDS-PAGE and agarose gel electrophoresis equipments

Mini-PROTEAN Tetra Cell, Mini Trans-Blot® module, PowerPac HC Power Supply and Trans-Blot® SD Semi-Dry Electrophoretic Transfer Cell (Bio-Rad, Hercules, CA, USA), electrophoresis chambers and accessories for agarose gel electrophoresis (biostep, Jahnsdorf, Germany).

6.1.1.5 Membrane scanner

Odyssey® CLx Imaging System (LI-COR Inc., Lincoln, USA) was used for western blot detection and kindly provided by the Kolanus' laboratory (LIMES-Institute, University of Bonn).

6.1.1.6 Thermocyclers

TPersonal (#050-551, Biometra, Goettingen, Germany)

TProfessional basic gradient (#070-601, Biometra, Germany)

6.1.1.7 Centrifuges

Eppendorf centrifuges (5415 R, 5430 R and 5810, Eppendorf, Hamburg, Germany)

Allegra® X-15R (Beckman Coulter, Brea, CA, USA)

6.1.2 Microscope

Several microscope set-ups were used as indicated in the respective sections, where also details about adjusted pixel size and setting are stated.

6.1.2.1 Bright-field microscope

Inverted microscope ECLIPSE TS100, CFI60 Infinity Optical System (Nikon, Tokyo, Japan) was used for cell culture

6.1.2.2 Epifluorescence/TIRF microscope

Olympus IX81 microscope equipped with an oil immersion objective 60x 1.49 NA Apochromat and a 1.6 x magnifying lens (Olympus, Japan). The microscope is coupled with a 16-bit EMCCD camera (16 x 16 μm^2 pixel size, ImagEM C9100-13, Hamamatsu Photonics, Japan) with diverse magnification lenses (1x, 2x, 4x). For Epifluorescence illumination, the system is equipped with a 150 W Xenon lamp integrated into a MT20E fluorescence illumination system (Olympus, Japan) in combination with

F36-500 DAPI HC, F36-525 EGFP HC and F36-503 Tritc HC filter sets (AHF Analysentechnik, Tuebingen Germany). The TIRF modus was realized by an integrated 488 laser LAS/488/20 (Olympus, Japan) in combination with CMR-U-MTIR-488-HC filter set (Olympus, Japan). The CellR software (Olympus, Japan) was used for recording.

6.1.2.3 Confocal laser scanning microscope

Olympus FluoView™ FV1000 (Olympus, Japan) confocal laser scanning microscope with an integrated oil immersion objective UPlanSApo 60x NA 1.35 (Olympus, Japan) and equipped with 405, 488 and 543 Lasers (located at the Kolanus' laboratory, LIMES Institute, university of Bonn). The system was controlled with the Olympus Fluoview 3.0 software (Olympus, Japan).

6.1.2.4 Gated Stimulated Emission Depletion (g-STED) microscope

All STED microscopy was performed on a TCS SP8 gated-STED microscope (Leica, Mannheim, Germany) from the German Centre for Neurodegenerative Diseases (DZNE) in Bonn and located at the center of advanced European studies and research (caesar) in Bonn, at the Light Microscopy Facility (LMF). The microscope used a 100x 1.4 NA oil immersion objective and was equipped with a pulsed Laser (White Light Laser) for fluorescence excitation and a continuous 592 nm laser for stimulated emission depletion. Fluorescence detection and time gating was controlled via hybrid detectors (HyD).

6.1.3 Flow cytometer

A LSR II (BD Biosciences) flow cytometer was used for FACS experiments. The cytometer was kindly provided by the Schultze' laboratory (LIMES Institute, University of Bonn).

6.1.4 Antibodies

6.1.4.1 Primary antibodies

Anti-Human CD81: Functional Grade Purified: mouse monoclonal IgG1 clone 1D6 (#16-0819, eBioscience, San Diego, CA, USA)

Anti-CD81 (5A6): mouse monoclonal IgG1 clone 5A6 (#sc-23962, Santa Cruz, USA)

Anti-CD81 (1.3.3.22): mouse monoclonal IgG1 (#sc-7637, Santa Cruz, USA)

Anti-CD9: mouse monoclonal IgG1 (#SM3039P, Acris, USA)

Anti-CD9: mouse monoclonal $IgG_{2b\ Kappa}$ clone MM2/57 (#CBL 162, Merck Millipore, USA)

Anti-GFP (JL-8): Living Colors® A.v. Monoclonal Antibody mouse IgG_{2a}, (#632381, Clontech, Mountain View, CA, USA)

Anti-GFP (B-2): mouse monoclonal IgG_{2a} (#sc-9996, Santa Cruz, USA)

Anti GFP: rabbit polyclonal IgG (#A11122, Invitrogen, Carlsbad, CA, USA)

Anti-GFP (clone 3E6): mouse monoclonal IgG2a (#A11120, Invitrogen)

Anti-HPV-L1 (K75): rabbit polyclonal (kindly provided by Dr. Luise Florin, university of Mainz)

6.1.4.2 Secondary antibodies

Goat anti-rabbit IgG-HRP (#sc-2030, Santa Cruz, USA)

Goat anti-mouse IgG-HRP (#sc-2031, Santa Cruz, USA)

Goat anti-Mouse IgG (H+L) IRDye800CW (#926-32210, LI-COR, Germany)

Alexa Fluor® 488 donkey anti-mouse IgG (H+L) (#A21202, Invitrogen)

Alexa Fluor® 546 donkey anti-rabbit IgG (H+L) (#A10040, Invitrogen)

Alexa Fluor® 594 donkey anti-mouse IgG (H+L) (#A21203, Invitrogen)

Alexa Fluor® 594 donkey anti-rabbit IgG (H+L) (#A21207, Invitrogen)

Alexa Fluor® 647 goat anti-mouse IgG (H+L) (#A21235, Invitrogen)

Alexa Fluor® 647 chicken anti-rabbit IgG (H+L) (#A21443, Invitrogen)

6.1.5 DNA-purification kits

NucleoSpin ExtractII (#740609, Machery-Nagel, Dueren, Germany)

NucleoSpin Plasmid (#740588, Machery-Nagel)

NucleoBond PC500 (#740574, Machery-Nagel)

6.1.6 Protein purification and analysis

Pierce® BCA protein assay kit (#23225, Thermo Scientific, USA)

GFP-Trap®_A (#gta-20, Chromotek, Martinsried, Germany)

Protein G Mag Sepharose (#28-9440-08, GE Healthcare, USA)

Odyssey® Blocking Buffer (#402-467-0700, LI-COR, Bad Homburg, Deutschland)

Western Blotting Luminol Reagent (#sc-2048, Santa Cruz, USA)

6.1.7 Plasmids

pGEM®-T-Easy Vector System I (#A1360, Promega, Madison, WI, USA)

pEGFP-C1 (#6084-1, Clontech, USA)

pCD3Zeta-mEGFP (kindly provided by Dr. Jan van Üüm) used to amplify monomeric EGFP-sequence via PCR

pCD3Delta-mRFP (kindly provided by Dr. Jan van Üüm) used to amplify monomeric RFP-sequence via PCR

6.1.8 Human papilloma type 16 pseudovirions (PsVs)

PsVs were kindly provided by Dr. Luise Florin (University of Mainz, Germany)

6.1.9 Fluorescent beads for imaging

TetraSpek™ Microspheres, 0.1 µm, fluorescent blue/green/orange/dark red (#T-7279, Invitrogen)

TetraSpek™ Microspheres, 0.2 µm, fluorescent blue/green/orange/dark red (#T-7280, Invitrogen)

TetraSpek™ Microspheres, 0.5 µm, fluorescent blue/green/orange/dark red (#T-7281, Invitrogen)

6.1.10 Buffers and solutions

6.1.10.1 20x Poly-L-Lysin (PLL) stock solution

PLL (#P1524, Sigma-Aldrich) was dissolved in ddH_2O at a concentration of 2 mg/ml and stored at -20 °C in single-use aliquots of 1.5 ml volume.

6.1.10.2 Cytomix solution

120 mM KCl, 10 mM KH_2PO_4, 10 mM K_2HPO_4, 0.15 mM $CaCl_2$, 2 mM EGTA, 5 mM $MgCl_2$, 25 mM HEPES-KOH, pH 7.6. The solution was sterile-filtered using a Ø 0.2 µm filter, aliquoted and stored at -20 °C.

6.1.10.3 Ringer Solution

130 mM NaCl, 4 mM KCl, 1 mM $CaCl_2$, 1 mM $MgCl_2$, 48 mM D(+)Glucose, 10 mM HEPES-NaOH, pH 7.4. The solution was sterile filtered using a Ø 0.2 µm filter, aliquoted and stored at -20 °C.

6.1.10.4 Sonication buffer

120 mM potassium glutamate, 20 mM potassium acetate, 10 mM EGTA, 20 mM HEPES, pH 7.2

6.1.10.5 10x Phosphate buffered saline (PBS)

1.37 M NaCl, 27 mM KCl, 81 mM Na_2HPO_4, pH 7.2

6.1.10.6 Tris buffered saline (TBS)

50 mM Tris, 150 mM NaCl, pH 7.4

6.1.10.7 TBST

TBS with 0.1 % (v/v) Tween 20

6.1.10.8 SDS runnig buffer

25 mM Tris, 192 mM Glycin, 0.1 % SDS, pH 8.3

6.1.10.9 Western blot transfer buffer

25 mM Tris, 192 mM Glycin, 20 % (v/v) Methanol, pH 8.3

6.1.10.10 Western blot blocking buffer

5 % (w/v) milk powder in TBST

6.1.10.11 50x Tris-Acetate-EDTA (TAE) buffer

2 M Tris, 50 mM Na_2EDTA, 5.71 % (v/v) Acetic acid, pH 8.0

6.1.10.12 16 % paraformaldehyde (PFA) stock solution

16 % (w/v) paraformaldehyde was dissolved in ddH_2O under continuous agitation at 65 °C in the fume hood. After cooling to RT, the pH was adjusted to 7.2 by dropwise addition of NaOH. The prepared solution was aliquoted into single-use aliquots of 12.5 ml and stored at -20 °C.

6.1.10.13 4 % PFA fixation solution

The solution was prepared under the hood by mixing 12.5 ml 16 % PFA aliquot with 5 ml 10x PBS in 50 ml Falcon tube. The mixture was adjusted to 50 ml with ddH_2O to reach a final concentration of 4 % PFA/1 x PBS pH 7.2.

6.1.10.14 TMA-DPH solution

Saturated 1-(4-Trimethylammoniumphenyl)-6-Phenyl-1,3,5-Hexatriene *p*-Toluenesulfonate (TMA-DPH; #T204, Invitrogen) solution was centrifuged in 1.5 ml eppendorf tubes for 5 min at 16,000 x g. The supernatant was pipetted into a fresh tube and used directly (1:3 v/v) in the microscopy chamber solution (PBS for membrane sheets or Ringer solution for intact living cells) to visualize cellular membranes.

6.1.10.15 50 mM sulforhodamine 101 stock solution

30.3 mg sulforhodamine 101 (#S7635, Sigma) was dissolved in 1 ml autoclaved ddH_2O and stored in dark at RT.

6.1.10.16 100 µM phenylmethylsulfonyl fluoride (PMSF) stock solution

1.74 mg PMSF was dissolved in 10 ml pure isopropanol, aliquoted and stored at -20 °C.

6.1.10.17 4x Laemmli sample buffer

250 mM Tris pH 6.8, 30 % (v/v) Glycerol, 6 % (w/v) SDS, 0.04 % (w/v) bromphenolblue. The buffer was stored at -20 °C and supplemented 1:5 with β-mercaptoethanol when necessary.

6.1.10.18 Protease inhibitor cocktail stock solution

One tablet of Complete® EDTA free (Roche, Mannheim, Germany) was dissolved in 1 ml autoclaved ddH_2O and stored at -20 °C. The solution was added freshly at a concentration of 1:50

6.1.10.19 Radio immunoprecipitation assay (RIPA) buffer

10 mM Tris, 150 mM NaCl, 1 mM EDTA, 1 % (v/v) Triton X-100, 0.5 % (w/v) DOC, 0.1 % (w/v) SDS, pH 7.4 in autoclaved ddH_2O. The buffer was stored at 4 °C. 1 mM PMSF and protease inhibitor cocktail were added freshly prior to use.

6.1.10.20 HEPES wash buffer

150 mM NaCl, 5 mM $MgCl_2$, 25 mM HEPES, pH 7.2

6.1.10.21 HEPES lysis buffer

150 mM NaCl, 5 mM $MgCl_2$, 25 mM HEPES, 1 % (w/v) CHAPS (C5070, Sigma-Aldrich), pH 7.2 in autoclaved ddH_2O. The buffer was stored at 4 °C and was supplemented with 10 µM PMSF and protease inhibitor cocktail before use.

6.1.10.22 100x FACS buffer

10 % BSA, 0.5 % NaN_3 dissolved in 1x PBS and stored at 4 °C

6.1.10.23 1x FACS buffer

100x FACS buffer diluted (1:100) in pre-cooled 1x PBS and stored at 4 °C

6.1.11 Bacteria culture

All media prepared for bacteria cultures were autoclaved and stored at RT. In case of antibiotic selection mediums, antibiotics were added after autoclaving at a concentration of 100 µg/ml and 50 µg/ml for ampicillin and kanamycin, respectively. For long time storage, bacteria cultures were mixed with 30 % (v/v) glycerol and stored at – 80 °C.

6.1.11.1 *E. coli* bacteria

E. coli XL-10 Gold® Ultracompetent Cells (#200315, Stratagene, La Jolla, CA, USA)

6.1.11.2 LB-medium

2 % (w/v) LB-medium powder according to Lennox (#A6666, AppliChem, Darmstadt, Germany) in ddH_2O.

6.1.11.3 LB-agar plates

2 % (w/v) LB-medium powder according to Lennox, 2 % (w/v) agar in ddH_2O. The mixture was autoclaved and cooled at RT to ~55 °C; antibiotics were added at this step for antibiotic selection plates. Afterwards, the mixture was poured into petri dishes (~25ml/10 mm plate), cured at RT and stored at 4 °C.

6.1.12 Cell culture

All cell culture procedures with the human cell lines Jurkat E6.1 and HepG2 were performed under sterile conditions.

6.1.12.1 Cell lines

6.1.12.1.1 Jurkat E6.1 cells

Jurkat E6.1 cells are human leukemic T cell lymphoblast derived from peripheral blood of a fourteen year old male with T cell leukemia (Jurkat clone E6.1, *homo sapiens*, ATCC® TIB-152™)(Purchased from Sigma-Aldrich, #88042803).

6.1.12.1.2 HepG2 cells

HepG2 cells are a human liver hepatocellular carcinoma cell line derived from the liver tissue of fifteen years old male (HepG2, *homo sapiens*, ATCC® HB-8065™). HepG2 cells are adherent and grow as monolayers in small aggregates (Purchased from CLS, #300198). Preliminary experiments on HepG2 cells were performed on cells that were a gift from the Famulok' laboratory (University of Bonn). Note that no differences between cell types were observed.

6.1.12.2 Medium for Jurkat E6.1 cells

RPMI-1640 (#21875-091, gibco, UK), supplemented with 10 % (v/v) FBS superior (#S0615, Biochrom, Germany), 1 % (v/v), Penicillin-Streptomycin 100x (10,000 U/ml potassium penicillin and 10 mg/ml streptomycin sulfate) (#DE17-602E, Lonza, Belgium).

6.1.12.3 Medium for HepG2 cells

EMEM (#12-662F, Lonza, Belgium), supplemented with 10 % (v/v) FBS superior (#S0615, Biochrom, Germany), 1 % (v/v), Penicillin-Streptomycin 100x (10,000 U/ml potassium penicillin and 10 mg/ml streptomycin sulfate) (#DE17-602E, Lonza, Belgium).

6.1.12.4 Trypsin

Trypsin-EDTA (1x), Dextrose 1 g/l, KCl 400 mg/l, $NaHCO_3$ 580 mg/l, NaCl 8 g/l, Trypsin 500 mg/l, EDTA 200 mg/l (#BE17-161E, Lonza, Belgium)

6.1.12.5 PBS for cell culture

Dulbecco's Phosphate Buffered Saline (DPBS) without Ca^{2+} and Mg^{2+}, KCl 200 mg/l, KH_2PO_4 200 mg/l, NaCl 8 g/l, $Na_2HPO_4.7H_2O$ 2.16 g/l (#BE17-512F, Lonza, Belgium)

6.2 Methods

6.2.1 Cloning

The cloning steps of all constructs were performed following the standard methods of cloning described by Sambrook and Russell (Sambrook and Russell, 2006). Primers used for cloning were designed manually and ordered from MWG Operon (Obersberg, Germany). All cloned constructs were sequenced by GATC (Konstanz, Germany). If necessary, the sequencing procedures were done stepwise using different primer positions to cover the whole desired sequence.

Starting from a cDNA library, I amplified by polymerase chain reaction (PCR) the sequences for CD81 (NM_004356.3) EWI-2 (NM_052868.4) and CD9 (NM_001769.3) using primers which align perfectly to the 5' ends of the sense and antisense strands of the cDNA to get blunt-ended PCR products. Using One*Taq*® DNA-Polymerase (#M0480S, NEB, UK), I added an adenine at the 3' ends of the PCR products. The amplified PCR products carrying 3' adenines rests were subcloned into a pGEM-T easy vector (#A1360, Promega, Madison, WI, USA).

The subcloned CD81 cDNA was fused directly, via fusion PCR (Heckman & Pease, 2007), to the N-terminus of monomeric enhanced GFP (Zacharias et al., 2002) (see 6.1.7), or to the N-terminus of monomeric RFP (Campbell et al., 2002) (see 6.1.7); carrying two silent mutations at the positions 4 and 5 to generate a XhoI restriction side) with a stop codon. The fused PCR products were inserted via NheI/KpnI restriction sites into the expression vector pEGFP-C1 (#6084-1, clontech, Mountain View, CA, USA) lacking EGFP to generate the two wild-type CD81 constructs versions CD81-GFP (figure 12) and CD81-RFP (figure 13).

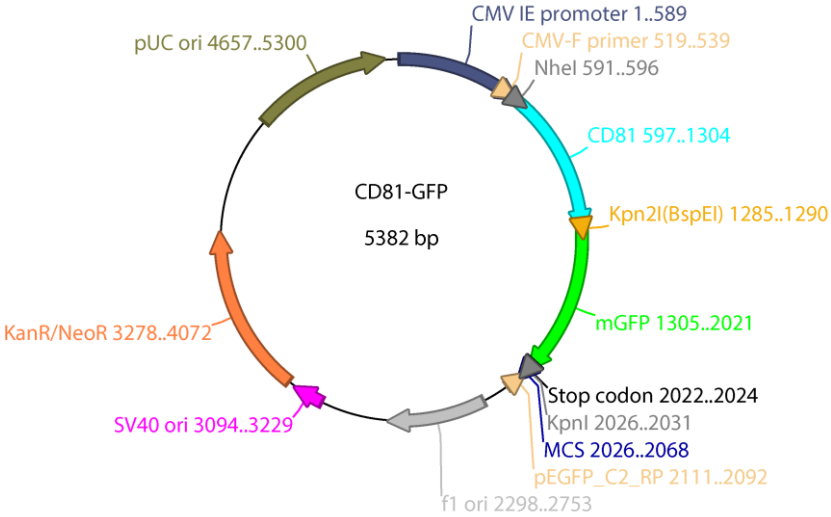

Figure 12. CD81-GFP construct cloned in the expression vector pEGFP-C1

CMV; human cytomegalovirus, MCS; multiple cloning site, f1 ori; f1 origin, KanR/NeoR; Kanamycin/Neomycin resistance, pUC ori; pUC origin. (Created using ApE software http://biologylabs.utah.edu/jorgensen/wayned/ape/)

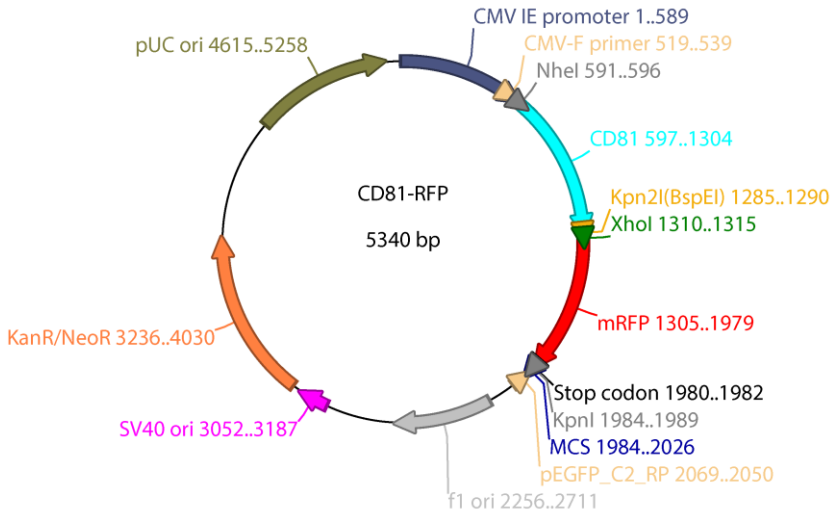

Figure 13. CD81-RFP construct cloned in the expression vector pEGFP-C1

For abbreviations see figure 12. (Created using ApE software http://biologylabs.utah.edu/jorgensen/wayned/ape/)

CD81 constructs were derived from CD81-GFP after substitution or deletion using fusion PCR and then inserted between NheI and Kpn2I a C-terminal restriction site within the CD81 sequence. If the mutation was downstream of the Kpn2I site, the fusion PCR was performed for the whole CD81-GFP sequence and products were inserted via NheI/KpnI sites. Using this procedure I generated the following constructs: CD81-C/A with all juxtamembrane cycteins at the positions 6, 9, 80, 89, 227 and 228 substituted for alanine; CD81-$\Delta\alpha\beta$ lacking aa 115-155; CD81-$\Delta\gamma$ lacking aa 156-174; CD81-$\Delta\gamma\delta$ lacking aa 156-190 and CD81-$\Delta\delta$ lacking aa 176-186.

The same cloning procedures were performed using fusion PCR to fuse EWI-2 or CD9 C-terminally to the N-terminus of mRFP carrying a C-terminal myc-tag (myc sequence; GAACAAAAACTTATTTCTGAAGAAGATCTG) followed by a stop codon. Finally, the pEGFP-C1 expression vector was used as a target for inserting EWI-2-RFP-myc via the AgeI/KpnI sites (figure 14) or CD9-RFP-myc via NheI/KpnI sites (figure 15).

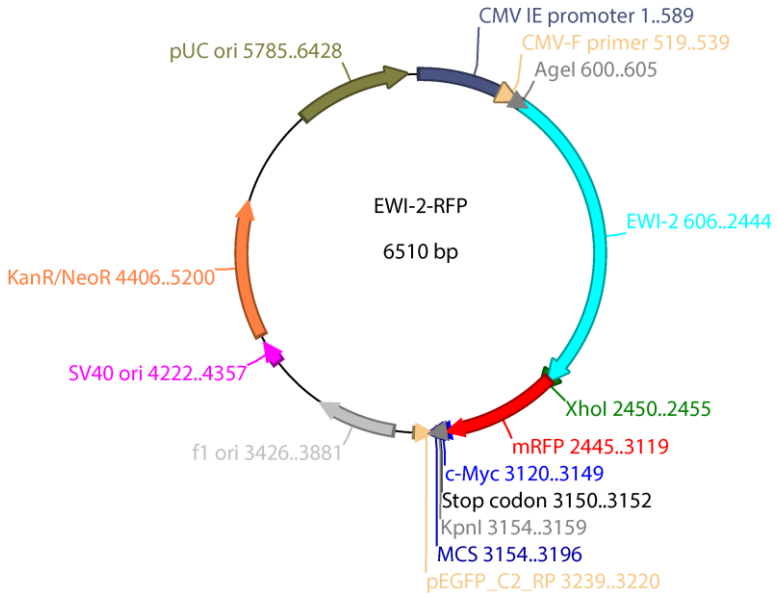

Figure 14. EWI-2-RFP construct cloned in the expression vector pEGFP-C1

For abbreviations see figure 12. (Created using ApE software http://biologylabs.utah.edu/jorgensen/wayned/ape/)

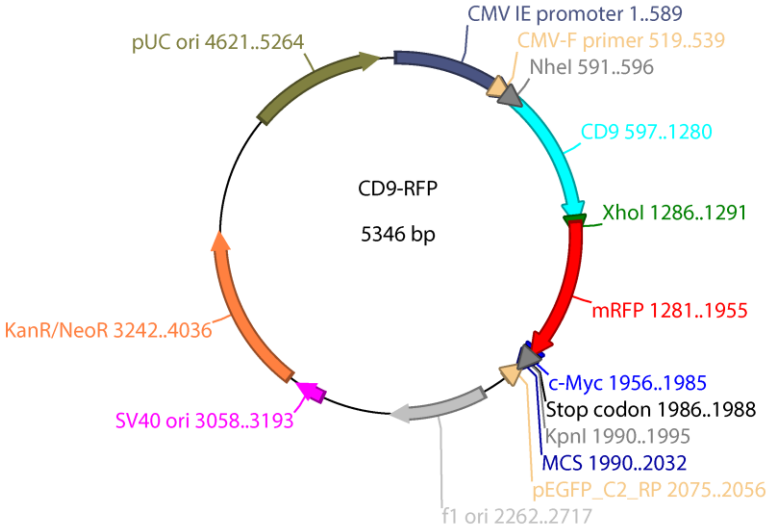

Figure 15. CD9-RFP construct cloned in the expression vector pEGFP-C1

For abbreviations see figure 12. (Created using ApE software http://biologylabs.utah.edu/jorgensen/wayned/ape/)

For the amplification of plasmid DNA, the bacterial strain *E. coli* XL-10 Gold® Ultracompetent Cells (see 6.1.11.1) was used. DNA/PCR products were purified using plasmid/PCR purification kits (see 6.1.5).

6.2.2 Cell culture

All cell lines were cultivated in standard cell culture vessels (Sarstedt, Nümbrecht, Germany and Labomedic Bonn, Germany).

6.2.2.1 Cell culture and splitting

HepG2 and Jurkat E6.1 cells were cultivated in 75 cm^2 and 175 cm^2 flasks, respectively. Adherent HepG2 cells were split 1:4 every 3 days when they reached 80 % confluence. In brief, cells were washed once with DPBS and detached from the flask after 3 min incubation with 1 ml Trypsin/EDTA at 37 °C. The cells were washed with 9 ml full medium and pipetted up and down to collect all detached cells in the flask. 2.5 ml of cell suspension were pipetted into fresh flask containing 22.5 ml full medium. Cell culture was maintained further by 37 °C. Jurkat E6.1 cells were split every 3 – 4 days by simple dilution to yield a concentration of 2 × 10^5 cells/ml.

6.2.2.2 Cryo-stocks

HepG2 cells were washed, detached and collected as described in 6.2.2.1. At this step the cell concentration was determined using a Neubauer counting chamber. The cell suspension was transferred into a 15 ml falcon tube and centrifuged for 3 min at 1000 rpm in an Eppendorf centrifuge 5810. The supernatant was aspirated and the cell pellet was resuspended in freezing medium (full medium supplemented with 10 % DMSO) at a concentration of 2.5 × 10^6 cells/ml. For the suspension Jurkat E6.1 cell line, cells were counted directly from the culture and then collected by centrifugation, washed with DPBS, centrifuged again and resuspended in freezing medium at a concentration of 5 × 10^6 following the same protocol as for HepG2 cells. 1 ml cell suspension aliquots were pipetted in cryovials and then frozen in a gradient freezing chamber (Nalgene Cryo containers, #C1562-1EA, Sigma-Aldrich, Hamburg, Germany) at -80 °C over night and transferred to a liquid nitrogen container on the next day.

For thawing cells, a cryovial aliquot was removed from the liquid nitrogen tank and allowed to thaw directly in a water bath at 37 °C for 2 min. The cell suspension was washed in 9 ml pre-warmed full medium, centrifuged and the cells were taken up in the appropriate volume of pre-warmed full medium.

6.2.2.3 Cell transfection

HepG2 and Jurkat E6.1 cells were transfected using the Gene pulser Xcell electroporation system (Bio-Rad, Hercules, CA, USA). 60 µg plasmid DNA were used for a single transfection, while 30 µg of each plasmid were used for a double transfection.

3×10^6 HepG2 cells/transfection were resuspended with DNA in 400 µl Cytomix solution, transferred to a 2 mm electroporation cuvette and electroporated at the following settings: Exponential protocol, 200 V, 950 µF, 200 Ω. For Jurkat E6.1 cells, 1×10^7 cells/transfection were used and electroporation was performed in a 4 mm electroporation cuvette after resuspending the cells with DNA in 800 µl Cytomix solution. The electroporation pulse was set to the following pulse program: Exponential protocol, 250 V, 1500 µF and infinite Ω. Accumulated cell debris on top of the cell suspension after electroporation was carefully aspirated and subsequently the cell suspension was pipetted directly into pre-warmed medium and cultured at 37 °C in an appropriate flask. Experiments with HepG2 and Jurkat E6.1 cells were performed 1 day and 2 days after transfection, respectively.

6.2.2.4 Glass coverslips cleaning and coating with poly-L-Lysine

For all microscopy experiments, the glass coverslips used were first cleaned and, if required, coated with poly-L-Lysine. For cleaning, coverslips were first incubated for 2 h in 1 M HCl in a glass beaker under constant agitation followed by five wash steps with ddH_2O. Next, coverslips were incubated for 2 h in 1 M NaOH under constant agitation. Subsequently, the coverslips were washed again five times with ddH_2O

and once with absolute EtOH. Finally, the coverslips were incubated for 2 h in absolute EtOH. Afterwards, the EtOH was discarded and the cleaned coverslips were baked, dried at 70 °C and kept at RT in a sterile surrounding.

Coating was performed in a sterile hood. A 1x working solution of 100 µg/ml poly-L-Lysine was prepared by diluting a 20x poly-L-Lysine stock solution in autoclaved ddH_2O. The coverslips were transferred into 6-well plates and coated with 500 µl of 1x poly-L-Lysine solution for 30 min at RT. Finally, the poly-L-Lysine solution was aspirated and the coverslips were dried at RT under the sterile hood for 2 h. The prepared coverslips in 6-well plates were then stored at 4 °C.

6.2.3 Preparation of membrane sheets

The preparation of unroofed cells or membrane sheets facilitates visualization and examination of membrane protein organization with high sensitivity. This detergent-free preparation uses a 100 ms ultrasound pulse to generate two dimensional, pure, native basal plasma membranes by applying mechanical shearing forces (Avery et al., 2000; Heuser, 2000). The prepared membrane sheets allow biochemical access to the cytosolic side of the native cell membrane and allow exclusive imaging of the basal membrane and its tightly attached components with a high signal to noise ratio (figure 16).

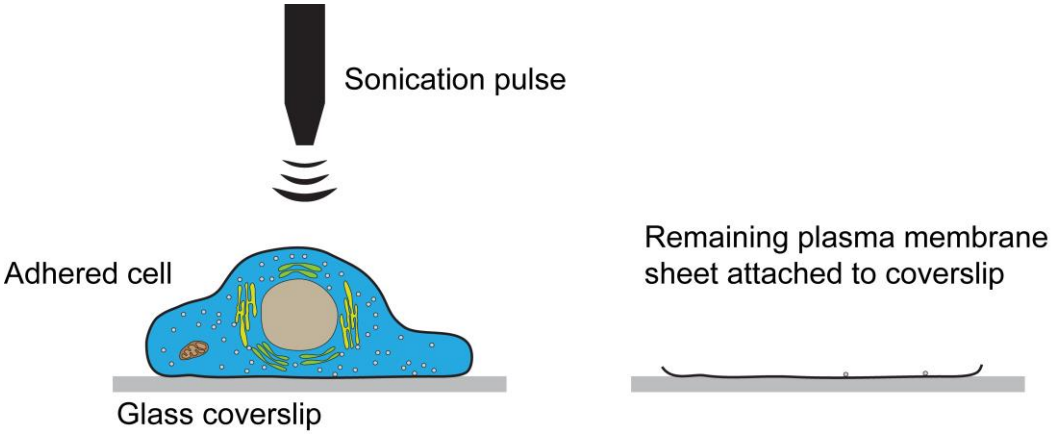

Figure 16. Preparation of membrane sheets

Intact living cells adhered on poly-L-Lysine coated glass coverslip are treated with a 100 ms sonication pulse. The mechanical shearing force leads to washing off the upper part of the cell leaving only the native basal membrane and membrane associated vesicles attached to the coverslip. Membrane sheet preparations are devoid from out-of-focus signals and present a detergent free preparation to analyze membrane structures organizations.

The preparation of membrane sheets from HepG2 cells was performed after transfecting and plating on poly-L-Lysine coated coverslips in 6-well plates at a concentration of ~5 × 10^5 cells/coverslip. After one day, HepG2 cells were ready to use for sonication. In contrast, Jurkat E6.1 cells were collected 2 days after transfection (see 6.2.2.3) and resuspended in pre-warmed Ringer solution. Then, the cell suspension was plated onto 6-well plates containing poly-L-Lysine coated coverslips at a concentration of ~1.5 × 10^6 cells/coverslip. Cells were incubated in the cell incubator for 20 min to allow for adhesion of cell to the coverslips before sonication. For membrane sheets generation, each coverslip was placed with the cells facing up in a glass dish containing ice-cold sonication buffer. The tip of an ultrasound sonicator Sonopuls HD 2070 (Bandelin, Berlin, Germany) was submerged into the sonication buffer above the coverslip at a distance of ~0.5 cm. Afterwards, a 100 ms sonication pulse was applied at a pulse power optimized for each cell line, which was 75 % and 25 % for HepG2 and Jurkat cells, respectively. The successful generation of membrane sheets was verified by visual inspection confirming the appearance of a star-shape transparency clearing in the center of the coverslip, indicating the presence of unroofed cells in this area.

Subsequently, the coverslip was transferred to a new 6-well plate and fixed directly for 30 min at RT with 4 % PFA in PBS. Finally, the fixative was quenched for 30 min at RT with 50 mM NH_4Cl in PBS, followed by 3 washes of 10 min with PBS.

6.2.4 Immunostaining of membrane sheets from cells expressing CD81-GFP

Membrane sheets were generated from transfected cells, fixed, quenched and washed (see 6.2.3). Subsequently, membrane sheets were incubated with the first antibody anti-CD81 (Anti-Human CD81 mouse monoclonal IgG1 clone 1D6, eBioscience) diluted (1:100) in 3 % BSA-PBS for 1 h at RT in a dark humid chamber followed by washing 3 times with PBS for 10 min. The incubation with the secondary antibody (Alexa Fluor® 594 donkey anti-mouse IgG (H+L), Invitrogen) diluted (1:200) in 3 % BSA-PBS was performed in the dark for 1 h at RT for HepG2 and overnight at 4 °C for Jurkat E6.1 cell membrane sheets. Then, the coverslips were washed 3 times with PBS for 10 min and directly imaged in PBS supplemented with a lipid dye (TMA-PDH) for visualization of membranes. The sheets were observed using the Olympus IX81 microscope (see 6.1.2.2) in epifluorescence modus. The exposure times in the green channel for imaging of HepG2 and Jurkat membrane sheets were 1 s and 100 ms, respectively. In the red channel, the exposure times were 500 ms and 100 ms for HepG2 and Jurkat samples, respectively. All images are shown applying a linear lookup table at arbitrary scaling.

6.2.5 Determination of protein concentration

The protein concentration was determined using the BCA Protein Assay Reagent (#23225, Thermo Scientific, Rockford, USA) following the manufacture's protocol. The absorbance at 595 nm was measured in 96-well-plates using the microplate reader Infinite® F200pro (TECAN, Maennedorf, Switzerland). The protein concentration was determined referring to a BSA standard curve.

6.2.6 Immunoprecipitation

For immunoprecipitation, 1×10^7 Jurkat T cells were used two days after transfection (see 6.2.2.3). Cells were washed once with ice cold HEPES buffer and then lysed in 1 ml HEPES lysis buffer. The solution was incubated for 2 h at 4 °C on the tube rotator. Afterwards, the cell lysate was centrifuged for 5 min at 6000 rpm using an Eppendorf centrifuge (Eppendorf centrifuge 5430R) and the lysate supernatant was transferred into a new tube 50 µl of the lysate were removed and kept for input samples. During the lysis, GFP-Trap® A (#gta-20, Chromotek, Martinsried, Germany) beads, which are covalently coupled with anti-GFP recombinant antibody fragments, were equilibrated by washing once with ddH_2O and twice with HEPES buffer. Between each washing step beads were collected by centrifugation for 2 min at 2500 x g and the supernatant was carefully aspirated. The cell lysate was incubated with 30 µl pre-equilibrated GFP-Trap® A beads rotating for 2 h at 4 °C. Subsequently, beads were collected by centrifugation for 2 min at 2500 x g and then washed twice with 500 µl HEPES buffer. Finally, beads were loaded into the gel pockets under non-reducing conditions to avoid cleavage of the disulfide bridges in the LEL which precludes later detection of the epitope in western blot analysis.

6.2.7 SDS-PAGE and western blot analysis

The protein biochemistry experiments were performed following standard methods as described in (Kyhse-Andersen, 1984; Laemmli, 1970; Towbin et al., 1979) or (Rehm & Letzel, 2010).

Immunoprecipitation samples were prepared for SDS-PAGE by mixing the samples (1:4) with 4x Laemmli sample buffer under non-reducing conditions and boiled for 10 min at 95 °C. For further analysis, samples were shipped to the laboratory of Dr. Luise Florin (University of Mainz). Florin' laboratory is equipped with a more sensitive protein detection system. Further processing was performed by Dr. Konstanze Scheffer using the following protocol. In brief, proteins were separated on 10 %

polyacrylamide gels and then transferred to nitrocellulose membranes (#10485376, Whatman, Maidstone, UK). Afterwards, membranes were blocked for 1 h at RT with TBS-T 5 % milk and then incubated with the first antibody anti-GFP (Living Colors® A.v. Monoclonal Antibody (JL-8), #632381, Clontech, Mountain View, CA, USA) diluted 1:10,000 in TBS-T 5 % milk followed by 3 washing steps with TBS-T for 10 min. Next, membranes were incubated with the HRP-coupled secondary antibody anti-mouse (goat anti-mouse IgG-HRP, #sc-2031, Santa Cruz, USA) diluted 1:5,000 in TBS-T 5 % milk for 1 h at RT and then washed 3 times for 10 min with TBS-T and once with TBS. Then the same protocol was performed using either anti-CD81 (mouse monoclonal (1.3.3.22),#sc-7637, Santa Cruz, USA) diluted 1:200 or anti-CD9 (mouse monoclonal, #SM3039P, Acris, USA) diluted 1:10,000 in TBS-T 5 % milk after membrane stripping by washing with 1 M NaOH for 5 min. Finally, membranes were developed on autoradiography films. In other western blot analyses performed in Bonn, the same protocol was used following the immunoprecipitation lysis protocol, the GFP antibody used was anti-GFP (rabbit polyclonal IgG, #A11122, Invitrogen, Carlsbad, CA, USA) diluted 1:1000 and the secondary antibody used was anti-rabbit (goat anti-rabbit IgG-HRP, #sc-2030, Santa Cruz, USA) diluted 1:5000 in TBS-T 5 % milk.

Alternatively, another western blot protocol was also optimized in this work, which was varied in some steps. Cells were lysed in 100 µl ice cold RIPA buffer and incubated under rotation for 30 min at 4 °C. Afterwards, cells were centrifuged for 5 min at 4 °C at 13000 rpm and the cell lysate samples were mixed (1:4) with 4x Laemmli buffer supplemented with β-mercaptoethanol. After protein separation on 10 % polyacrylamide gels, the proteins were transferred onto a nitrocellulose membrane using a semi-dry blotting system (Bio-rad). In the following steps, Odyssey® Blocking Buffer (#402-467-0700, LI-COR, Bad Homburg, Deutschland) was used instead of TBS-T 5 % milk. The first antibody was an anti-GFP antibody (mouse monoclonal IgG_{2a} (B-2), #sc-9996, Santa Cruz, USA) diluted (1:1000) in Odyssey® Blocking Buffer and the secondary antibody

was labeled with the fluorescent dye IRDye®800CW (Goat anti-Mouse IgG (H+L) IRDye800CW, #926-32210, LI-COR, Germany) diluted (1:5000). Finally the antibody staining was visualized using the Odyssey® CLx Imaging System (LI-COR Inc., Lincoln, USA).

6.2.8 Flow cytometry, fluorescence activated cell sorting (FACS) analysis

Transfected cells were washed once with ice cold DPBS and then harvested by cell scraping in the case of HepG2 cells or by centrifugation (for 3 min at 1000 rpm) in the case of Jurkat T cells. The cell pellet was resuspended in ice cold 1x FACS buffer at a concentration of 10^6 cells/100 µl. For each FACS sample 100 µl cell suspension was pipetted into FACS tube (Polystyrene round-bottom 12 x 75 mm) (#2017257, Labomedic, Germany). Since low temperature inhibits endocytosis and surface internalization pathways, all staining and washing steps were performed on ice and all buffers and reagents were pre-cooled before use. 1 µg of the first antibody anti-CD81 (anti-human CD81 mouse monoclonal IgG1 clone 1D6, eBioscience) was directly added to the cell suspension in the FACS tubes, mixed by a quick vortex-pulse and incubated in the dark for 30 min at 4 °C. Next, cells were washed twice with 500 µl 1x FACS buffer centrifuging for 5 min at 300 x g and 4 °C. Afterwards, cells were incubated in the dark with 1 µg of the secondary antibody anti-mouse (Alexa Fluor® 647 goat anti-mouse IgG (H+L), #A21235, Invitrogen) for 30 min at 4 °C followed by two washing steps for 5 min centrifuging at 300 x g and 4 °C. Control conditions included omission of the first antibody as well as unstained transfected and non-transfected cells which were prepared and incubated in parallel with the treated samples. Finally, samples were analyzed on a LSR II (BD Biosciences) (see 6.1.3). The fluorescence intensity of all channels is shown at logarithmic scaling and the thresholds of the fluorescence channels were adjusted once for each cell line in order to set the control population at the origin of the axes. Samples were sorted at low flow speed to avoid the detection of multiple events, measuring no more than

1000 events/sec. The data were analyzed and plotted using FlowJo software (TreeStar Inc., Ashland, OR, USA).

6.3 Microscopy

To visualize different proteins of interest on the cell membrane, they were coupled directly to fluorophores by generating fusion proteins with mGFP or mRFP proteins. Alternatively, immunostaining was performed using a first antibody raised against the protein of interest and a secondary antibody coupled to a fluorescent dye. As outlined in detail below, for studying static and dynamic aspects of tetraspanin domains several microscopy methods including epifluorescence, TIRF, FRAP and STED microscopy were applied.

6.3.1 Epifluorescence microscopy

Epifluorescence microscopes have a relatively simple setup consisting of a light source (usually a Xenon lamp) coupled to filter sets for specific excitation and detection of different dyes followed by an optical system and an EMCCD camera. In an epifluorescence microscope, the excitation light propagates through the whole sample and the light emitted by dyes located in a relatively large area along the z-axis is collected, which can increase the signal to noise ratio (figure 17). This microscopy modus was mostly used with 2-dimensional samples (membrane sheets) that in an ideal case generate no out-of-focus light.

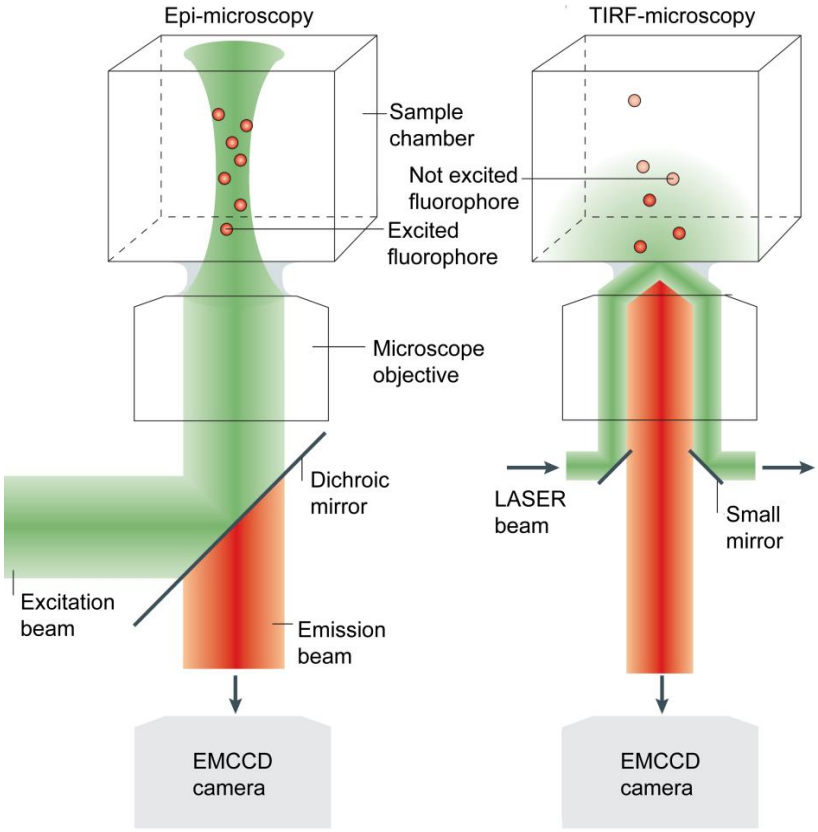

Figure 17. Technical differences between epi- and TIRF-microscopy

Epifluorescence microscopy setup is shown on the left and a TIRF microscopy setup on the right. The excitation beam is depicted in green and the emission beam in red. An EMCCD camera is used for low noise imaging of low light levels. In the case of epifluorescence microscopy (left), the dichroic mirror in the middle of the objective light trajectory reflects the excitation light into the objective from which it focused into the sample, while emission light collected by the objective passes through. In the case of TIRF microscopy (right), small mirrors at the edge of the objective serve for generation a total internal reflection at the interface between the sample and the objective. The excitation light propagates through the sample and excites all fluorophores within the light trajectory in the case of epifluorescence, whereas the propagated excitation laser light at the edge of the objective in the case of TIRF-microscopy will be reflected on the interface between the sample and the coverslip, yielding a standing evanescent light decays exponentially by distance and excites the fluorophores close to the interface (modified from Veigel & Schmidt, 2011).

An Olympus IX81 microscope (see 6.1.2.2) was operated in epifluorescence modus. The fixed membrane sheet preparations were imaged in PBS supplemented with the lipid dye TMA-DPH to verify the integrity of the plasma membrane. The system was set to 192x magnification using optical lenses yielding a pixel size of to 83.3 nm. The microscope was controlled with the CellR Olympus software. Recorded

images were exported as TIFF files and analyzed with ImageJ software. Information about recording times are given in the respective sections.

6.3.2 Total internal reflection fluorescence (TIRF) microscopy

TIRF microscopy is a fluorescence microscopy technique that allows exclusive sample illumination up to 50 – 100 nm distance (in the z-axis) from the interface between glass and sample. This enables specific excitation of a thin optical layer in the close proximity of the glass. In case of adherent cells, this method allows the detailed visualization of fluorophores or fluorophore-coupled proteins in the basal plasma membrane and membrane docked vesicles at a high signal to noise ratio while using whole cells. The physical principle behind this method is total internal reflection occurring at the interface between two media with different refractive indices ($n_{glass} > n_{sample}$), when the angle of the incident light becomes greater than the critical angle (Mattheyses et al., 2010). Total reflection of the incident light creates an evanescent wave on the interface which enters the sample. The intensity of the evanescent illumination decays exponentially with the distance from the interface. Therefore, out of plane signals originating from inner compartments of the cell are strongly diminished (figure 17).

TIRF imaging was performed with an Olympus IX81 microscope coupled to a 488 nm laser using the TIRF modus of the microscope (see 6.1.2.2).

TIRF microscopy was used to study cluster immobilization and stability on living Jurkat cells. Cells were collected and then resuspended in pre-warmed Ringer solution. Cell suspensions were plated on 6-well plates containing poly-L-Lysine coated coverslips at a concentration of ~1.5 × 10^6 cells/well. Cells were adhered in the cell incubator for 20 min and imaged at RT within the next 20 min. Images series were recorded at 2 Hz for 15 s. Images series were analyzed by calculating the Pearson correlation coefficient (PCC) between two successive images. The PCC values obtained from each measurement were averaged and for each

independent experiment all calculated values were averaged using Excel (Microsoft Corporation, Redmon, USA). The pixel, the system magnification and the controlling software were the same as described in the previous section (see 6.3.2).

6.3.3 Confocal laser scanning microscopy (CLSM)

6.3.3.1 Static views

An Olympus FluoView™ FV1000 confocal microscope (see 6.1.2.3) was used to visualize fluorescence signals with optical sectioning of the cell body. An overview image of intact living transfected Jurkat cells was acquired in Ringer solution at a pixel size of 103 nm while experiments performed with immunostaining after permeabilization with Triton X 100 were imaged at a pixel size of 207 nm. The intensity of the utilized laser lines (405 nm, 488 nm and 543 nm) was set to 5 % and the dwell time was adjusted to 8 µs/pixel. In the case of living cells, samples were additionally recorded in the bright-field mode.

6.3.3.2 Fluorescence recovery after photobleaching (FRAP)

FRAP enables studying the dynamics of fluorophore-coupled proteins and the determination of their lateral diffusion coefficient. The FRAP experiments were done using an Olympus FluoView™ FV1000 confocal laser scanning microscope (see 6.1.2.3) on intact, living transfected Jurkat cells adhered on poly-L-Lysine pre-coated glass coverslips in Ringer solution. The measurement was done on the basal plasma membrane of the cells and the image sequences were recorded at 0.5 Hz for 160 s. The recording laser intensity of the utilized laser line (488 nm) was set to 0.2 %, the pixel size was adjusted to 207 nm and the dwell time was set to 40 µs/pixel. The recorded image size was defined by 100 x 100 pixels and bleaching was performed within a 10 x 10 pixel ROI (~2.1 µm x 2.1 µm area) using the 405 nm and 488 nm laser line simultaneously at full intensity. The recording series of each FRAP measurement was initiated with 3 pre-bleach frames, subsequently the sample was bleached for 500

ms at full laser intensity followed by 76 post-bleach recording frames. The overall bleaching effect and/or potential focus drift occurring during the measurement was assessed by recording the fluorescence intensity within a control ROI of the same size placed near the ROI used for bleaching. For background correction another ROI was placed outside of the cell. The recorded intensities of all ROIs were used to calculate the background-subtracted, relative fluorescence intensities within the bleach and control ROIs. The whole measurement was recorded for 160 s. During this time, the system occasionally showed instabilities toward the end of the measurement; therefore only the first 80 s were used for the analysis. The recorded data from the control, bleach and background ROIs were imported to Excel (Microsoft Corporation, Redmon, USA). The background intensities were subtracted from the intensity values of the control and bleach regions. All measurements showing an intensity deviation greater than 15 % in the control ROI after 80 s were excluded from the analysis. This deviation was calculated from the averaged background-corrected fluorescence intensities of the first three and last three (until 80 s) frames. Cells with very high and very low expression levels were also excluded. The background-corrected fluorescence intensities recorded in the bleach ROI were normalized to the average of the three pre-bleach values to calculate the percentage of the fluorescence recovery over the time. For each independent experiment the average of all measured cells was calculated. Finally, the averaged fluorescence recovery was plotted against time using Origin 8 Pro software (OriginLab Corporation, Northampton, USA) and FRAP curves were fitted to the hyperbola equation described in (Ficz et al., 2005).

$$\mathbf{y(t) = y0 + Rec_{Max} \times t / (T_{1/2} + t)},$$

where y0 is the offset, Rec_{Max} is the maximal recovery and $T_{1/2}$ corresponds to the half-maximum recovery time. The calculated half-maximum recovery was used to calculate the diffusion coefficient using the following equation described by Axelrod (Axelrod et al., 1976).

$$\mathbf{D = (w^2 / 4\, T_{1/2})\, \gamma_D},$$

where w is the radius of the bleached area (here: ~1 µm), $T_{1/2}$ is the half-maximum recovery and γ_D is shape correction factor of the bleached area (here: 1.1).

6.3.4 Super resolution microscopy: gated stimulated emission depletion (g-STED)

For a long time the resolution of the light microscopy was limited by the diffraction or spreading of light waves. This effect occurs when light waves of point light sources pass through a small aperture or are focused onto a small spot (Huang et al., 2010) and yields a blurred, widened image of this spot. Blurring is systematic and a feature of the microscope specific point spread function (PSF). For visible light, this results in a resolution limit of ~250 nm in the x, y axis as described by Ernst Abbe about 150 years ago and widely known as the Abbe limit (Abbe, 1873). This means that subcellular structures at distances smaller than the diffraction limit are not resolvable by light microscopy (figure 18). Super resolution microscopy has broken this limit and has allowed the resolution to reach much higher ranges.

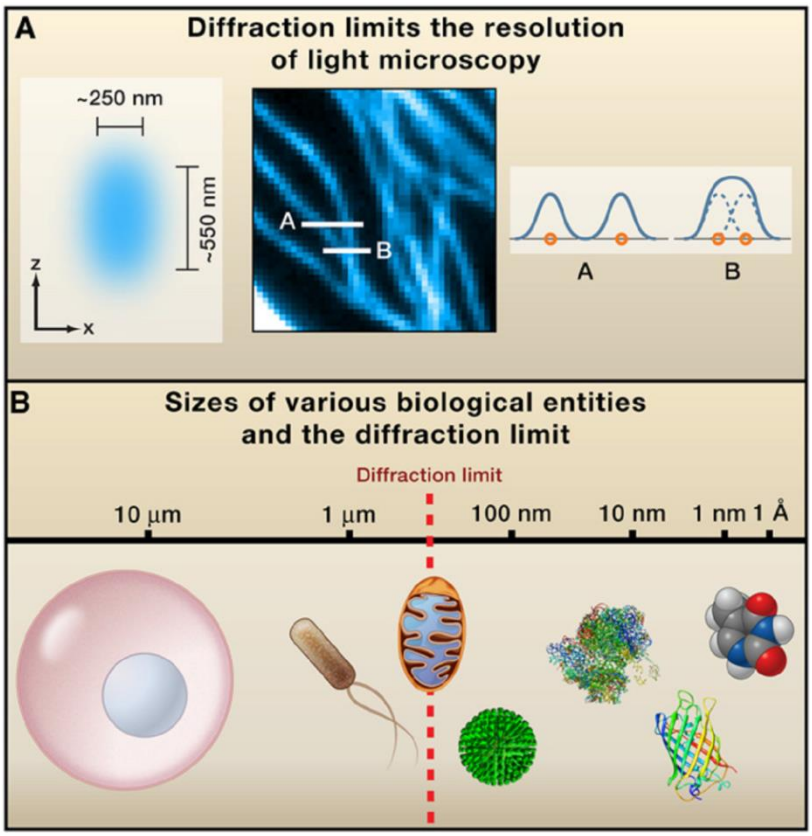

Figure 18. Barrier of the diffraction-limited resolution produced by light microscopes

(A) Signal from a point emitter modulated by the point spread function from a typical objective with high numerical aperture pictured by the cyan ellipsoid, has a width of ~250 nm in the x-axis (lateral direction) and ~550 nm in the z-axis (axial direction). These dimensions define the diffraction-limited resolution of the light microscope; therefore two objects separated by a distance greater than this resolution limit can be resolved and appear as two separate entities. At smaller distance objects appear as a single unresolved entity. These two cases are shown for two line scans on a microtubule image (middle) showing in the right panel two cyan curves A and B, where the scan in A is resolved and the scan in B is unresolved. (B) Various biological structures are shown in a size scale, where the left part to the red dashed line (the diffraction-limited barrier) can be resolved by light microscopy; whereas the right part remains unresolvable. From left to right; a mammalian cell, a bacterial cell, a mitochondrion, an influenza virus, a ribosome, the GFP protein and a small molecule (thymine) (derived from Huang et al., 2010).

The theoretical background of super resolution STED fluorescence microscopy was first described by Hell and Wichmann (Hell & Wichmann, 1994). The STED microscope is a confocal laser scanning microscope with an excitation laser and an additional doughnut-shaped STED laser which overlaps with the excitation beam. The STED laser depletes the excited fluorophores so that only fluorophores in the doughnut center,

which defines the subdiffraction size, remain in an excited state (figure 19) (Willig et al., 2006). STED microscopy has been further developed in the Hell laboratory in order to improve the resolution of the system. The gated STED microscope is based on a conventional STED microscope applying pulsed excitation and continuous depletion together with time-gated detection (figure 19) (Vicidomini et al., 2011). The gated STED microscope can reach a resolution up to ~20 nm, which makes it an excellent tool for accurate measurements of cluster size and organization.

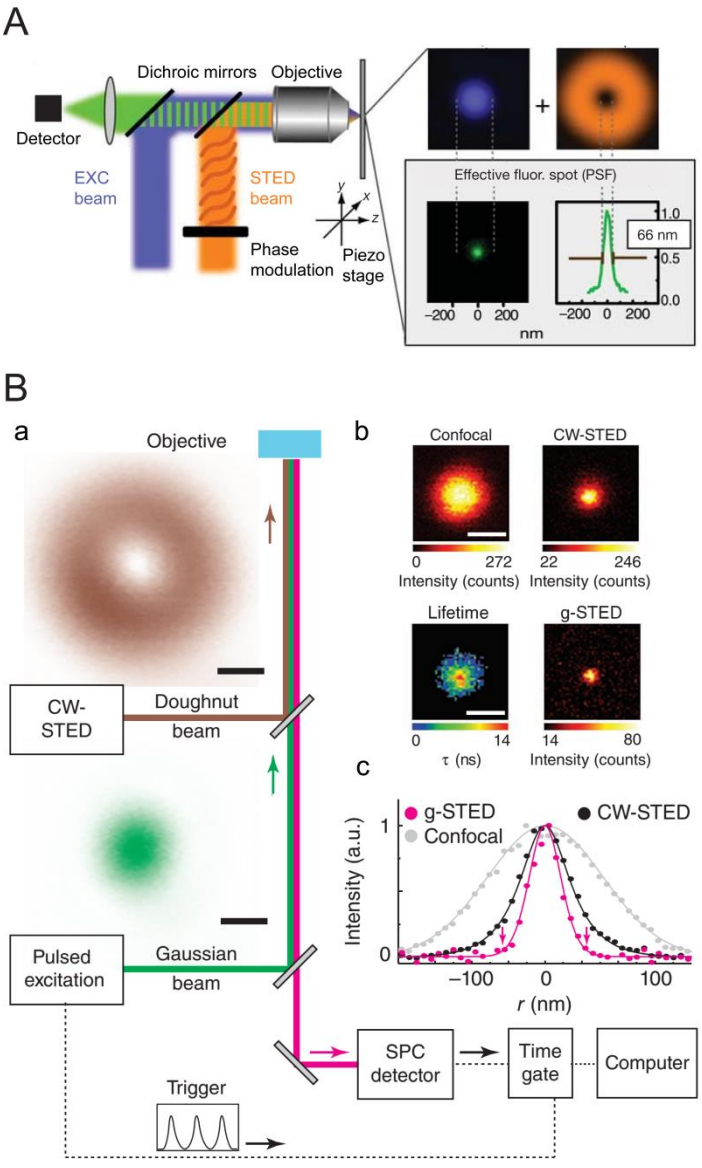

Figure 19. Principle of STED and g-STED super resolution microscopy

(A) Principle of STED microscopy. The excitation laser beam (blue, EXC) is focused to a diffraction-limited excitation spot (blue spot in right panel), while the STED beam (orange), which is able to de-excite molecules, is focused to a doughnut-shaped spot (orange spot in right panel). Superimposition of these two spots reduces the excitation area to the doughnut center, yielding a subdiffraction excitation spot size shown in green in the lower panel, which shows in this example 11-fold reduction in size beyond the diffraction limit (modified from Willig et al., 2006). (B) Principle of gated STED microscopy. (a) As in continuous wave (CW) STED, the excitation (green) and STED (brown) focal spots are superimposed. Gated STED employs a single-photon-counting (SPC) detector, whose detection events of emitted fluorescence light (magenta), are time-gated with respect to the excitation pulses (Trigger) and registered by a computer. The time-gated detection is characterized by the time delay (T_g) of detection after excitation, and the detection period during recording. Therefore, this kind of detection increases the quality of the detected signal via preferential collection of fluorescence from the center of the excited spot (as shown in b). (b) Upper

panels, fluorescence image point sources (beads) for confocal (left) and CW-STED (right). Lower panels, fluorescence lifetime image for the CW-STED recording (left), fluorescence image for g-STED (right, T_g = 15 ns). Only the fluorescence signal from the center of the light sources is collected (g-STED). (e) Normalized intensity profiles through the center of the confocal, CW-STED and g-STED images (modified from Vicidomini et al., 2011).

In this work STED imaging was performed using a TCS-SP8 gated-STED microscope (see 6.1.2.4). Membrane sheets were generated from HepG2 cells expressing CD81-GFP, fixed, quenched and washed as described above (see 6.2.3). However, the signal of bio-synthetized GFP has a short life-time (bleached easily) and is not sufficient for high quality detection. Therefore, the GFP-signal was amplified by immunohistochemistry labelling of GFP with a commercial fluorescent dye (Alexa Fluor® 488). After membrane sheets generation, sheets were blocked for 1 h at RT in 3 % BSA in PBS and then incubated overnight at 4 °C with anti-GFP antibody (clone 3E6) (mouse monoclonal, #A11120, Invitrogen) diluted (1:100) with 1 % BSA in PBS. Next, membrane sheets were washed 4 times with PBS and directly incubated for 2 h at RT with the secondary antibody Alexa Fluor® 488 donkey anti-mouse (#A21202, Invitrogen) diluted (1:100) with 1 % BSA in PBS. Coverslips were mounted on microscopy slides in 15 µl mounting medium (Prolong® Gold Antifade Mountant; #P10144, Invitrogen) and cured for 24 h at RT. Finally, the edges of the coverslips were sealed with clear nail polish and stored at 4 °C. Membrane sheets were also generated from cells co-expressing CD81-GFP and EWI-2-RFP proteins. Imaging was performed first by recording conventional confocal overview images in the red channel for EWI-2-RFP expression and in the green channel for CD81-GFP expression.

The overview images in the red channel were recorded at 400 Hz scan speed with STED laser turned off. Excitation was realized using the pulsed white light laser at 558 nm and 28 % power detecting fluorescence between 570 – 700 nm using the hybrid detector at 200 gain and with a 0 – 6.5 ns time gate and a pixel size close to 70 nm ± 0.5. For the green channel, overview images were acquired using similar settings with 1.4 % excitation laser power at 488 nm and detection between 495 – 571 nm at

200 gain gating from 0.1 – 6.5 ns. STED images were recorded at 200 Hz scan speed at 40 % STED laser power, excitation with the 488 nm line of the pulsed white light laser at 14 % power and detection between 495 – 507 nm using the hybrid detector at 200 gain gating between 1 – 6.5 ns. The pixel size was close to 20 nm ± 0.5. STED images were assembled from six individually recorded scans and averaged using ImageJ.

6.4 Pseudovirion induced endocytosis

Pathogen endocytosis is mediated by cell surface components, which gate its entry. CD81-GFP/CD81-Δδ-GFP expressing Jurkat cells were used to study pathogen entry during infection with pseudovirions (PsVs) prepared from the human papilloma virus 16 (Spoden et al., 2012) (see 6.1.8). 10^6 cells were used for each sample. First, cells were collected by centrifugation, resuspended in 5 ml pre-warmed full medium and transferred into 25 cm^2 flasks. The medium was supplemented with the fluid phase marker sulforhodamine101 (#s7635, Sigma-Aldrich, St. Louis, MO, USA) at a final concentration of 20 µM. Afterwards, the cell cultures were infected (except for controls) by carefully pipetting of 2 µl PsVs, which corresponds to 0.42 µg total protein or 0.2 µg of the capsid protein L1 of HPV16. The control and infected cell culture samples were incubated for 10 min in the cell incubator and were gently shaken from time to time to assure homogeneity of the culture and avoid cell sedimentation. This short incubation period was sufficient for the PsVs to bind to the membrane and to be taken up into early endosomes (data not shown). Subsequently, cells were collected by centrifugation for 3 min at 800 rpm using an Allegra X-15R centrifuge (Beckman Coulter, Brea, CA, USA), the cell pellet was resuspended directly in 1 ml pre-warmed Ringer solution and plated onto two (0.5 ml aliquot each) poly-L-Lysine coated coverslips dispersed in 6-well plates. Afterwards, the cells were adhered for 20 min in the cell incubator and either fixed directly or after membrane sheet preparation. Cells or membrane sheets were then imaged in PBS supplemented with TMA-DPH and 100 nm Tetraspeck beads, which served to correct lateral shifts that may occur during filter changes.

Microscopy was performed using the Olympus IX81 microscope (see 6.1.2.2) in the epifluorescence modus. Samples were imaged in the green, red and blue channels to analyze protein distribution (GFP), endosomes (fluid phase marker) and plasma membrane (TMA-DPH), respectively. The recorded images were aligned using the Align Slice plugin of ImageJ, and imported into the program CorelDRAW (Ottawa, Canada). The data were analyzed manually by counting endosomes (visualized in the red channel) per cell base colocalizing pixelwise with protein clusters in the green channel.

Infection with PsVs for 10 min, as described above, was performed to study the early step of pathogen endocytosis at the cell membrane. In a second set of experiments, a longer incubation time was chosen to allow the PsVs to enter the cell body. In addition, sulforhodamine was omitted and instead PsVs were stained in the red channel. 5×10^5 transfected Jurkat cells were incubated under constant agitation with 5 µl of PsVs for 1 h at 37 °C. Afterwards, cells were adhered and fixed as previously described. Cells were permeabilized for 2 min in 0.2 % Triton X-100 in PBS, washed twice with PBS for 10 min and blocked for 30 min with 1 % BSA in PBS. The pseudovirions were then immunostained using the rabbit antibody anti HPV-L1 (K75) raised against L1 protein of HPV16. The incubation with the first antibody diluted (1:1,000) with 1 % BSA in PBS was performed for 1 h at 37 °C followed by two washing steps (first with PBS and then with 1 % BSA in PBS for 10 min). Cells were incubated with the secondary antibody anti-rabbit (Alexa Fluor® 546 donkey anti-rabbit IgG (H+L), #A10040, Invitrogen) diluted (1:300) in 1 % BSA in PBS supplemented with Hoechst dye diluted (1:10,000) for 1 h at 37 °C. Afterwards, cells were washed twice with PBS for 10 min. Finally, cells were embedded by mounting coverslips on microscopy slides as described above (see 6.3.4).

Samples were imaged using at Olympus FluoView™ FV1000 confocal microscope (see 6.3.3.1) starting with the identification of transfected cells

in the green channel, followed by optical section scans at different z-positions in the blue, green, red and bright-field channels.

6.5 Microscopy data analysis methods

The analysis of raw microscopy data was performed using ImageJ software (Schneider et al., 2012). This software facilitates the analysis of defined ROIs, the generation of images stacks and the calculation of the fluorescence intensities. Moreover, the software was supplemented with different plugins for the calculation of the correlation coefficient between images or lateral shifting of one image in an images stack. ImageJ was also used to import raw microscopy data into other graphic programs and for figure editing. In some cases, events were counted manually on assembled images generated with CorelDRAW.

6.5.1 Fluorescence intensity analysis

For each experiment identical microscope settings were used for all days. The settings were identical regarding the microscope, optical equipment, magnification, illumination intensity and exposure times. The average fluorescence intensity in a ROI was corrected by subtracting the average intensity of an adequate ROI in the background.

6.5.2 Pearson correlation coefficient

PCC is used to quantify the degree of colocalization of signals in two images. PCC is unaffected by changes in the intensity offset (Adler & Parmryd, 2010). PCC values range from 1 (perfect correlation) to -1 (perfect negatively correlation or mirror image) with 0 for a random distribution and absence of any relationship. The correlation coefficient was calculated by the following equation described by Adler:

$$r = \Sigma (R_i - R_{av}) \times (G_i - G_{av}) / \sqrt{(\Sigma (R_i - R_{av})^2 \times \Sigma (G_i - G_{av})^2)},$$

where R_i is the fluorescence intensity of individual pixels in the first (here the red) image and R_{av} is its mean intensity, accordingly G_i and G_{av} are

the fluorescence intensity of individual pixels and the mean intensity of the second (here the green) image at the same pixels.

The correlation coefficient calculation was done with the plugin Colocalization_Indicies (Kouichi Nakamura, Kyoto University) installed in ImageJ program. For the correction of the lateral shift that occasionally occurred during imaging, the ImageJ plugin Align Slice (Gabriel Landini, University of Birmingham) was used prior to PCC calculation. This plugin allows manual correction of image drift in the x- and y-axis: Corrections were done with reference to Tetraspeck beads or to 3 - 4 prominent structures in the image.

6.5.3 Coclustering assay

Using the PCC (see 6.5.2), the coclustering assay allows the determination of the degree of colocalization between two fluorescently labeled proteins. Due to the limitation of the optical system and experimental processes the value of 1 cannot be reached even for the correlation of a double-tagged protein (r = 0.63) (Sieber et al., 2006). With our system, I was able to reach a PCC close to this value (r = ~0.6).

Membrane sheets (see 6.2.3) from co-transfected Jurkat cells expressing mRFP and mGFP labeled proteins were imaged in PBS supplemented with TMA-DPH for visualization of the membrane sheets and 100 nm Tetraspeck beads for the correction of lateral shifts that occasionally occurred during filter changes. An Olympus IX81 microscope (see 6.1.2.2) was used in the epifluorescence modus. Imaging with green and red filters allows specific recording of the green or the red tagged proteins. The green and red images were analyzed after lateral drift correction using the Align Slice plugin prior to PCC determination. The correlation coefficient was determined within a ROI of ~20 – 30 μm^2 which was placed on the membrane sheet in the blue channel and subsequently used for duplicating this section in the green and red channel. The PCC between both duplicated sections was determined using the Colocalization_Indicies plugin for ImageJ (see 6.5.2). The PCC values calculated from individual

membrane sheets were averaged for each independent experiment. The exposure times were 1 s and 2 s in the green and red channel, respectively.

6.5.4 Distribution of the expression levels

The expression level of a fluorescently tagged protein is, in an ideal case, linearly proportional to the fluorescence intensity of the expressed protein. The high difference of the expression levels between analyzed proteins in the same experiment or the high deviation of the expression level between different individual experiments can influence the result of the analyzed data. To control the expression levels of individual events in different experiment, the frequency of the expression levels was plotted in histograms. The background corrected fluorescence intensities in the red and green channels for mRFP and mGFP tagged proteins, respectively, were determined (see 6.5.1). The fluorescence intensities were arranged in bins of 1000 (a.u) width starting from 0 and the absolute frequency counts were determined using Excel. Finally, the frequency counts were plotted against the intensity bins showing the expression level distribution of individual samples. The fluorescence intensity in the red channel was lower than that in the green channel even though the exposure time in the red channel was two-fold higher than in the green channel (for 6.5.3).

6.5.5 Autocorrelation analysis

Autocorrelation analysis is a convenient tool to calculate the radial average size of objects in an image or to analyze the trend in radial size between different images. This method was developed and validated in this work.

This analysis was performed using the ImageJ software. First, a ROI was used to define and duplicate a region within the original image yielding a reference image for the analysis. Subsequently, the ROI was repeatedly shifted by 1 pixel into one direction in the original image using the Align Slice plugin followed by duplication of image in the ROI in the new

position. The duplicated images were used for PCC calculation between the reference image using the Colocalization_Indicies plugin. The PCC starts at 1 for the initial position (pixel shift = 0) and decreases upon shifting. The PCC values were plotted against the pixel shift yielding an exponential autocorrelation decay curve. The most important feature of the curve is the position at 50 % decay, at which half of a cluster or structure of the shifted image still correlates with its original image. The distance of displacement needed to reach the 50 % colocalization is an estimate of the average radial size of the present structures in the analyzed image. For better determination of this value, the autocorrelation decay curves were fitted using the following function:

$$y = 1 - (a \times x) / (b + x),$$

where a and b are arithmetic parameters that can be determined through curve fitting and then used to calculate the x value indicating the half-correlation position setting y = 0.5. The calculated x value corresponds to the number of shifted pixels to reach the 50 % autocorrelation point. For TIRF and epifluorescence images, the autocorrelation decay curves were averaged for each independent experiment and then fitted using this function to calculate the 50 % decay value (see above). STED micrographs were analysed by Dr. Jan-Gero Schlötel. In brief, the GDSC stack correlation plugin was used, after the intensity of each pixel was increased by one to avoid zero values that could not be processed. Autocorrelation analysis was done on three different ROIs for each membrane sheet. Then, the curves were averaged and fitted using a simple exponential decay function. The 50 % decay values determined for analyzed membranes were then averaged for each independent experiment.

7 Results

The introducing of FPs into life sciences has largely influenced the design of experiments. Also, in this study in most experiments FP-tagged constructs are used and analysed by microscopy. A construct similar to the C-terminally GFP-tagged CD81 construct cloned in this work was also generated and used in previously published works to study its functions during HCV entry (Coller et al., 2009) or cell-mediated immune response (Mittelbrunn et al., 2002). In this work, CD81-GFP was overexpressed in HepG2 and Jurkat cells. The membrane protein expression distribution was analysed in membrane sheets and it was confirmed that overexpressed and endogenous CD81 behave similarly as described below (see figure 20). Membrane sheets represent unroofed cells, and are prepared by applying a 100 ms ultrasound pulse on cells adhered onto glass coverslips. This sonication pulse generates pure mechanical shearing forces that rip off the upper part of the cell thus leaving behind only the basal plasma membrane attached to the coverslip. This two dimensional preparation enables studying membrane protein expression and distribution in the cell membrane with a high signal to noise ratio.

7.1 Expression of CD81-GFP in HepG2 and Jurkat cells

7.1.1 CD81-GFP is expressed at the cell membrane and is correctly oriented

Membrane sheets generated from HepG2 or Jurkat T cells expressing CD81-GFP were fixed and immunostained for CD81 using an anti-CD81 antibody raised against an extracellular epitope of CD81-LEL. First, I checked whether CD81-GFP is correctly expressed and oriented in the plasma membrane to exclude any possibility of flipping or missorting occurring during protein biosynthesis. The anti-CD81 antibody epitope should be located in the extracellular space between the glass coverslip and the tightly attached membrane sheets. Hence, the antibody has to diffuse between the coverslip and the membrane sheet from the edge to

the centre to reach the epitopes located in the middle of the membrane sheet. In the case of Jurkat T cells, which generate larger membrane sheets, the diffusion limitation prevented the antibody from reaching the centre of the sheet; accordingly, I saw a staining gradient starting bright at the periphery with a dark spot in the middle of the membrane sheet indicating the unstained area (figure 20C, middle upper panel). This observation confirms that the epitope of the antibody is located between the extracellular site and the coverslip indicating that the overexpressed CD81 is correctly oriented in the cell membrane.

7.1.2 Endogenous and overexpressed CD81 molecules are localized in the same clusters

Immunostained membrane sheets of transfected cells were imaged in the green and red channels. The GFP-tag of CD81-GFP was directly imaged in the green channel, while immunofluorescence signals were recorded in the red channel. In HepG2 cells, which do not express endogenous CD81, immunofluorescence originates only from the overexpressed CD81-GFP construct. However in Jurkat T cells, the antibody additionally binds to endogenously expressed CD81. Images recorded in the green and red channel show distribution of CD81 in spotty structures that overlap with each other (figure 20A and C). Moreover, the PCC between the red and the green images show a very good correlation between GFP and antibody signals in both cell types. In the case of HepG2 cells, for which all CD81-proteins are double labelled with both an antibody and GFP-tag, the PCC is close to a previously published value that indicates ideal correlation (Sieber et al., 2007). In Jurkat T cells, which also express endogenous CD81, the PCC is also close to this ideal value which indicates that the overexpressed and endogenous CD81 do not separate into distinct clusters.

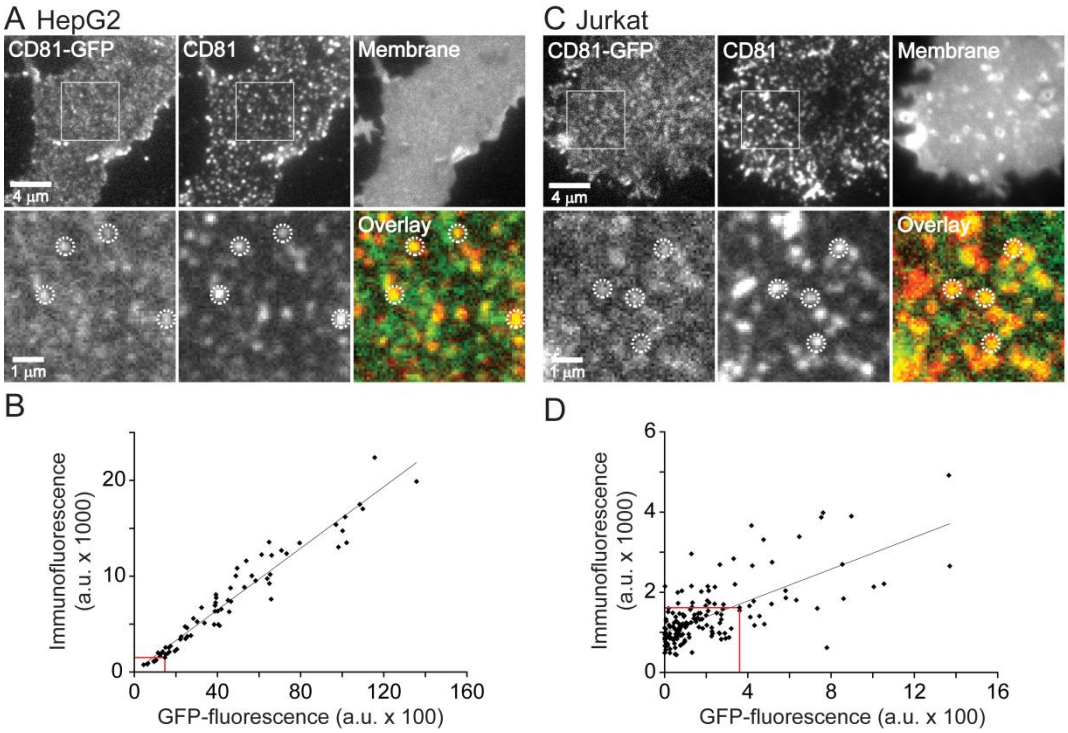

Figure 20. Immunostaining of overexpressed and endogenous CD81 in HepG2 and Jurkat cells

(A) HepG2 cells, which do not express endogenous CD81, were transfected with CD81-GFP, sheeted, fixed and immunostained for CD81 using an anti-CD81 antibody recognizing an extracellular epitope (Flint et al., 1999). Upper left panel, overexpressed CD81-GFP is clustered in plasma membrane protein domains and not homogenously distributed. Upper middle panel, the immunostaining signal shows CD81 molecules assembled in spotty structures. Upper right panel, the membrane was visualized using the lipophilic dye TMA-DPH. The lower panels show magnified views of the white square ROIs indicated in the upper panels. Lower right panel, overlay of the magnified views showing a high overlap between the GFP and the immunostaining channels. The Pearson correlation coefficient between the two channels gives a value of 0.57 ± 0.09 (mean ± SD; n = 70 membrane sheets from 3 independent experiments) which is comparable to a previous measurement of 0.63 (Sieber et al., 2006) from a double tagged protein and accepted as a reference for perfect colocalization. (B) Fluorescence intensities in the analysed membrane sheets in red (immunostaining) and green (GFP-tag) channels show a linear relationship between both signals. The linear regression intercepts close to 0 confirms the zero level of endogenous CD81 in HepG2 cells. (C) Membrane sheet from a Jurkat T cell overexpressing CD81-GFP (panels in similar order as for A). Similar to HepG2 cells, overexpressed CD81-GFP in Jurkat T cells is non-homogenously distributed but also clustered in membrane protein domains. The antibody staining was more sensitive for CD81 clustered in protein domains that were stronger in Jurkat cell (middle panels). Large Jurkat membrane sheets show after immunostaining a fluorescence intensity gradient from edge to the centre (upper middle panel) which indicates the correct orientation of the molecule in the membrane. In this case, the antibody diffusion is limited in the tight space between membranes and coverslips so that epitopes in the center of the membranes are not always reached. This effect was only observed for Jurkat membrane sheets since these are much larger than that those obtained from HepG2 cells. Note that membranes were directly fixed and not treated with

detergent. The calculated PCC between the two channels yielded similarly high values 0.52 ± 0.08 (mean ± SD; n = 32 membranes from 4 independent experiments) and close to the value obtained from HepG2 cells, confirming that endogenous and overexpressed CD81 cluster together and do not form separate clusters (compare also the overlay in the lower right panel). (D) The scatter plot of the green and the red fluorescence signals shows a linear relationship between GFP- and immunostaining signals. The offset, where the linear regression intercepts with the y-axis in the absence of CD81-GFP overexpression, indicates the level of endogenous CD81. In most of the analysed membrane sheets, the ratio between overexpressed and endogenous CD81 is close to 1 indicating that the overexpression generally doubled the cellular CD81 levels. Dotted circles in A and C indicate the high colocalization of randomly chosen spots in the green and the red channels. Red line projections in B and D indicate the membrane sheets presented in A and C, respectively. Note that the immunostaining and GFP intensities in B and D are not comparable due to different incubation times with antibodies and different recording times (for detailed information see 6.2.4) (derived from Homsi et al., 2014).

In the case of Jurkat T cells, an offset for immunostaining signals was observed (i.e. immunostaining signal, but not GFP signal), which corresponds to the endogenous CD81 level. For most sheets, CD81 overexpression hardly doubled the total CD81 content (figure 20D). In addition, the scatter plot shows a high variance of measurements from the regression line for Jurkat T cells (figure 20D), whereas the values show a very low variance in HepG2 cells and the measurements are closely placed to the regression line (figure 20B). This large scattering observed in Jurkat cells results from the additional immunostaining of highly variable endogenous CD81. Moreover, the high correlation between endogenous CD81 and overexpressed CD81-GFP confirms that both CD81 proteins partition into the same clusters (figure 20C and figure legend).

7.2 CD81-GFP overexpression levels compared to endogenous levels in HepG2 and Jurkat intact cells using FACS

Immunostaining of CD81/CD81-GFP was also performed with intact HepG2 and Jurkat T cells overexpressing CD81-GFP. In this setup, the anti-CD81 antibody again can only access the extracellular domains of the CD81 protein. Therefore, stronger staining of CD81-GFP expressing whole cells would confirm cell surface expression and correct orientation of the overexpressed CD81-GFP. I performed this analysis using FACS (see 6.2.8). The immunostaining fluorescence intensities for CD81

detected in the red channel (APC-A filter) were plotted against the fluorescence intensities of the overexpression levels detected in the green channel (FITC-A filter) using a logarithmic scale (figure 21). As seen in (figure 20), HepG2 cells lack endogenous CD81 and the counted events show a line-like distribution starting from the gating origins (figure 21A). In contrast, a large scattering of the counted events was observed with Jurkat T cells. These showed an offset of the immunostaining seen by the shift of the entire cell population to the upper quadrant indicating the presence of endogenous CD81 (figure 21B). Moreover, the linear relationship between CD81-GFP signal and staining signal suggests that also under high expression level no CD81 is retained in cytosol. I conclude that cytograms in figure 21A and B correlate perfectly with the microscopy results already shown in (figure 20B and D), respectively.

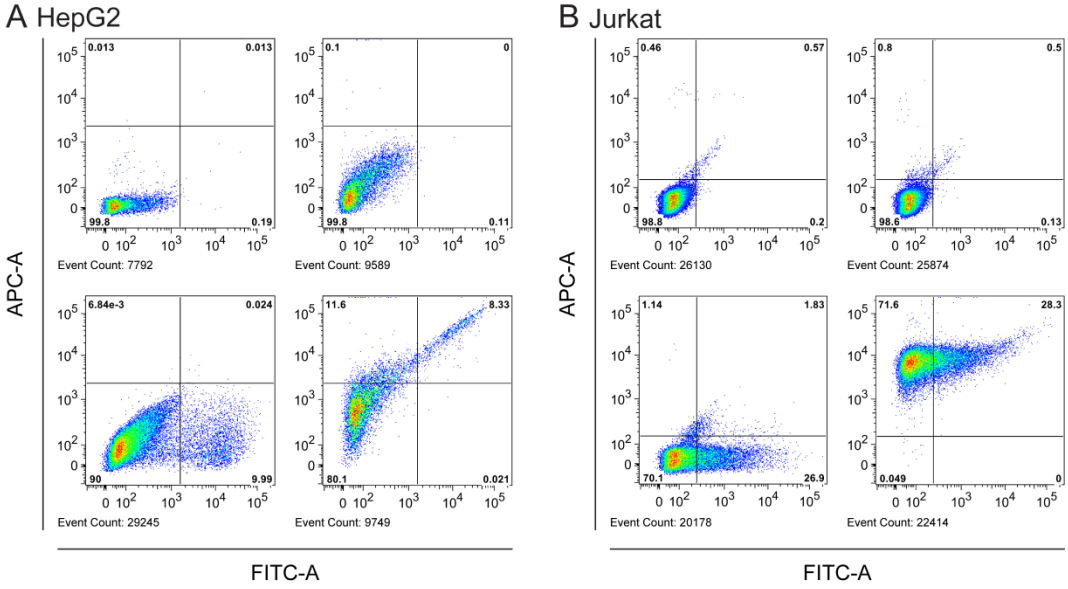

Figure 21. Overexpressed and endogenous CD81 levels in HepG2 and Jurkat cells analysed by flow cytometry.

(A) Intact HepG2 cells overexpressing CD81-GFP were immunostained for CD81 (same antibody used as in figure 20) and analysed with a flow cytometer using FITC-A and APC-A filters for GFP and red immunostaining signals, respectively. Two-parameter cytograms at a logarithmic scale show the scattering of measured events in the green and red channels. Upper left cytogram, untreated and non-transfected cells used as a control cell population (for more details see 6.2.8). Upper right cytogram, non-transfected cells treated with only the secondary antibody used for staining control and gating. Lower left cytogram, untreated transfected cells allowed assessment of the expression level. Lower right cytogram, transfected and stained cells with first and secondary antibodies. The scattering of events in a line-like fashion indicates a linear relationship between the

red and the green signals. Furthermore, successful staining confirms the correct orientation of the overexpressed CD81-GFP protein. Moreover, linearity between CD81-GFP signal and staining signal suggests that also under high expression no CD81 is retained in cytosol. An imaginary regression line would cross the origins of the gated quadrants which again confirms that HepG2 cells lack endogenous CD81. (B) Intact Jurkat cells overexpressing CD81-GFP and immunostained for CD81; upper cytograms, left, untreated and non-transfected cells; right, non-transfected cells treated with secondary antibody. Lower cytograms, left, transfected and untreated cells; right, transfected and stained cells for CD81. The counted events show a high degree of scattering and a linear trend between the two signals indicating the linear relation between red and green channel with an offset in the staining at the absence of CD81-GFP signal corresponding to the endogenous CD81 level. The large scattering of the counted events is due to the endogenous CD81 offset signal. Furthermore, the slope of an imaginary regression line is lower than the one predicted in A. This is in line with figure 20 indicating a high endogenous CD81 level and an overall lower overexpression level of CD81-GFP in Jurkat cells. The histograms show representative results from one out of three independent experiments. For each experiment and condition 5,000 – 30,000 events were counted.

7.3 Increased CD81 concentration generates more clusters

Overexpressed CD81 forms apparently more clusters in the membrane (compare the spotty structures in the green channel images of figure 20). However, the various clustering grade could not be completely resolved due to the diffraction limit of the epifluorescence microscopy. To study the clustering behaviour of CD81 at various concentrations of overexpressed CD81 STED superresolution microscopy experiments were performed using HepG2 cells, which lack endogenous CD81. At low CD81 concentration a linear relationship between CD81 expression levels and cluster density was observed: At densities of up to 40 clusters/μm^2 doubling the CD81 concentration resulted in an almost twofold increase in cluster density (figure 22C; inset). At higher CD81 concentrations, cluster density slowly reached a plateau phase (figure 22C). The plateau phase is due to the limited ability to resolve properly individual clusters even at superresolution conditions which leads to underestimation of the actual cluster number (figure 22; see membrane sheets #3 and #4 at STED microscopy resolution in B). Hence, the data showed that CD81 expression correlate linearly with the cluster density over a wide range of expression levels. In conclusion, these observations indicate that additional CD81 molecules assemble in new clusters rather than

increasing the size of clusters or being free, uniformly distributed molecules.

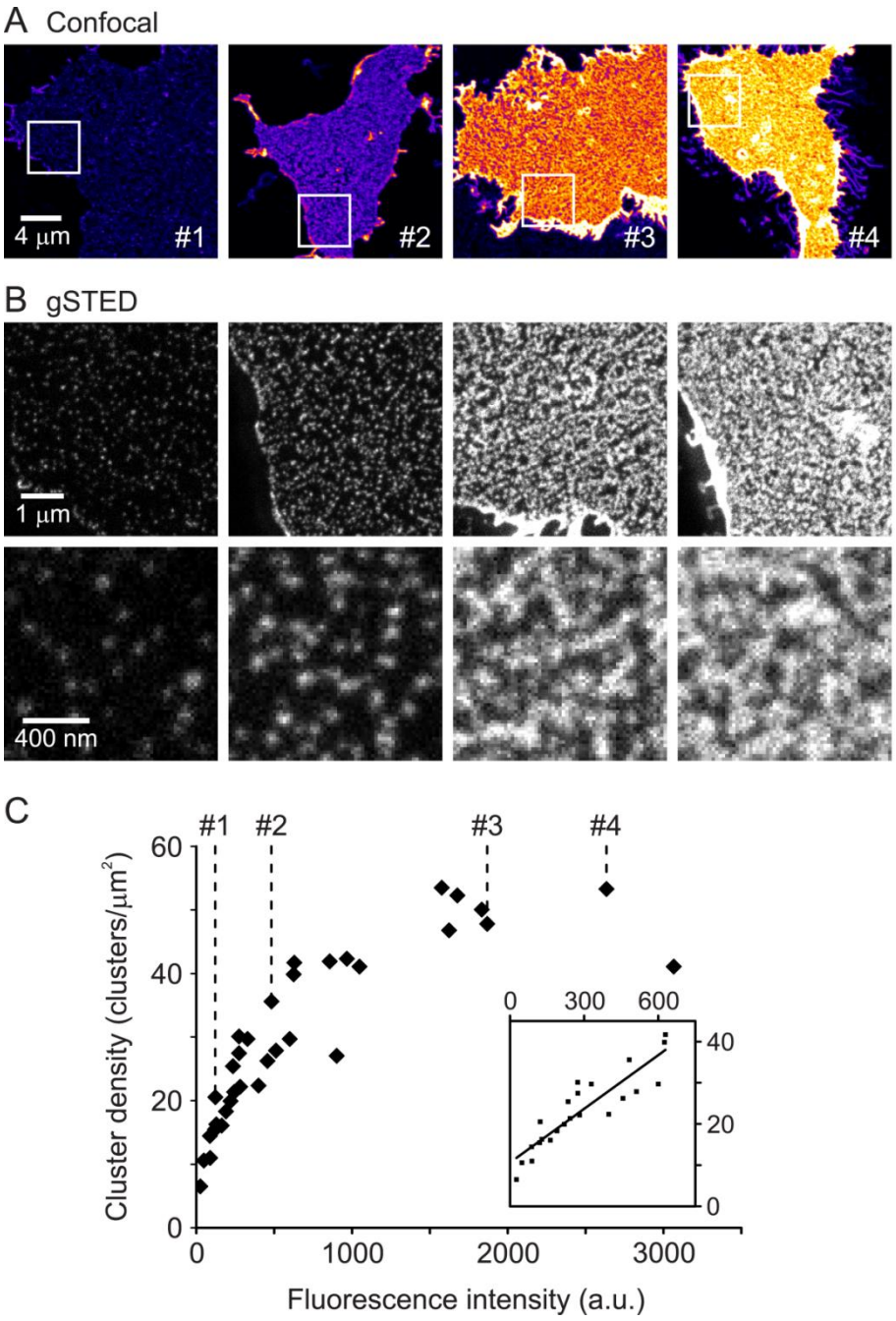

Figure 22. Elevated CD81 concentrations lead to an increase in cluster number but apparently not in cluster size.

HepG2 cells (which lack endogenous CD81) were transfected with CD81-GFP, sheeted and imaged with gated STED microscopy (for more details see 6.3.4). The GFP signal was enhanced by immunostaining with anti-GFP antibody (see 6.3.4). (A) Series of four confocal images (#1 to #4) showing membrane sheets with increasing CD81 concentration prepared from cells with varying CD81 expression levels presented at the same scaling using a fire lookup table. The measured immunofluorescence intensity was

used to quantify the CD81 concentration. (B) The overviews in A were imaged by gated STED microscopy and shown are STED micrographs sections of the area indicated in the white squares ROIs in A. Three ROIs (one shown in the lower panel) were selected from the STED overview image and used for manual cluster counting; the average from the three ROIs was used to calculate the cluster density for the respective membrane sheet. (C) The calculated cluster densities were plotted against the CD81 concentration for each appropriate sheet. The membrane sheets shown in A are labelled #1 to #4 in the scatter plot. The cluster density and the CD81 concentration present a linear relationship at low CD81 concentrations (see also the inset in C). At high CD81 concentration levels, it was hard to distinguish between individual clusters so that the curve reached a plateau. The data are collected from three independent experiments for each 8 – 13 membrane sheets were analysed (data provided by Dr. Jan-Gero Schlötel and Prof. Thorsten Lang; derived from Homsi et al., 2014).

7.4 Generation of CD81 variants

I aimed studying the clustering mechanism of CD81. Hence, I focused on the characterization of the protein domain(s) or feature(s) crucial for CD81 assembly into cluster and CD81 enriched microdomains. The strategy to generate CD81 constructs was based on the crystal structure of the LEL published by Kitadokoro (Kitadokoro et al., 2001; Kitadokoro et al., 2002) and the 3D structure of CD81 described by Seigneuret (Seigneuret, 2006) which illustrates the different protein domains of CD81 (figure 23A). Kitadokoro and Seigneuret described the CD81-LEL (subdivided in α- β- γ- δ- and ε-domain) as the most important CD81 region, which is responsible for protein targeting, dimerization and interaction. In addition, CD81 palmitoylation has been described to play a prominent role in TEM formation (Hemler, 2005). Referring to this information, I generated a palmitoylation deficient mutant by substitution all six juxtamembrane cysteines for alanine (see 6.2.1). Moreover, I generated also a couple of deletion mutants, where domain(s) in the LEL were subsequently deleted (deleted domains are highlighted in red in the illustrations generated at atomic realistic scale in figure 23B). The following CD81 deletion constructs were generated: $\Delta\alpha\beta$ lacking aa 115 – 155; $\Delta\gamma\delta$ lacking aa 156 – 190; $\Delta\gamma$ lacking aa 156 – 174 and $\Delta\delta$ lacking aa 176 – 186 and effect of deletion/mutation on TEM formation was tested as described in the following sections. Size and expression of the generated constructs were tested using western blot analysis (see Appendix 1 A).

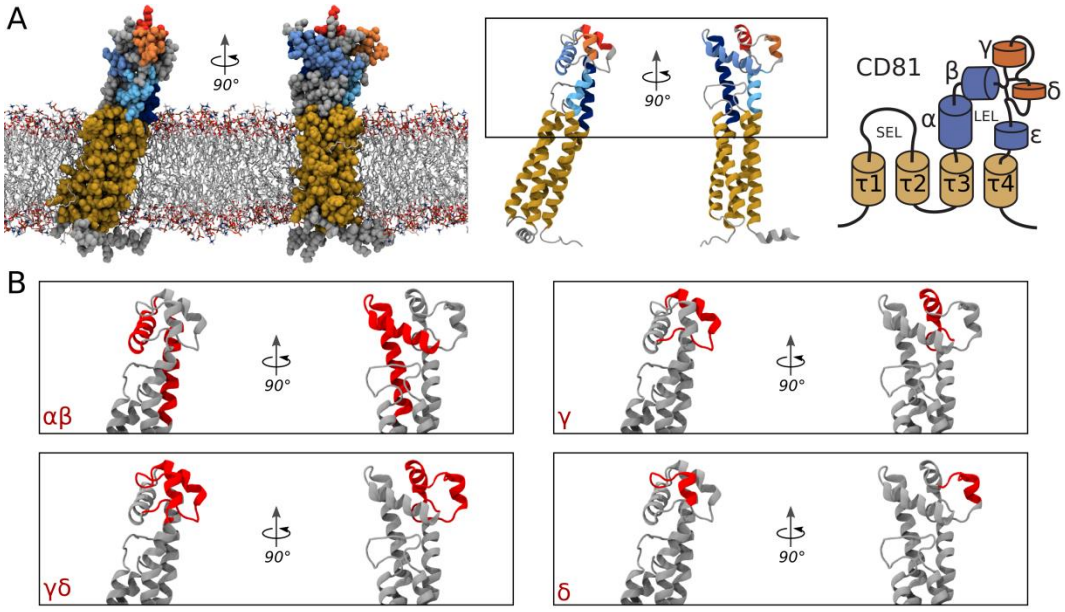

Figure 23. CD81 deletion mutants

(A) Left, atomistic model of a human CD81 molecule based on previously published data from Seigneuret (Seigneuret, 2006). The CD81 molecule is embedded in a lipid bilayer comprising pre-equilibrated POPC (1-palmitoyl-2-oleoyl-sn-glycero-3-phosphocholine) molecules (Poger & Mark, 2010), and simulated using the LAMBADA and InflateGRO2 routines (Schmidt & Kandt, 2012). Middle, ribbon representation; right, pictogram of CD81 structure which will be used for the next figures. The transmembrane domains (τ1 – τ4) are depicted in gold, the constant domain in blue and the variable domain in orange; SEL, small extracellular loop; LEL, large extracellular loop. (B) Magnified view of the extracellular domain with the deleted domains αβ, γ, γδ and δ highlighted in red (this corresponds to the constructs Δαβ, Δγ, Δγδ and Δδ, respectively). Molecular illustrations were generated using VMD (Humphrey et al., 1996) and the integrated STRIDE routine (Frishman & Argos, 1995) (figure provided by Dr. Thomas Schmidt, based on figure 10 and derived from Homsi et al., 2014).

7.5 The CD81 δ-domain is essential for targeting of CD81 into CD81 enriched microdomains

I used the constructs described above (figure 23B) to identify the protein domain(s) and/or the role of palmitoylation necessary to drive CD81 molecules into CD81 enriched microdomains. I overexpressed wild-type CD81-RFP together with either wild-type CD81-GFP or GFP-tagged CD81 mutant in Jurkat T cells and then analysed whether the green and red overexpressed constructs were enriched in the same domains (figure 24). This quantification was done by calculating the PCC as a co-clustering grade between the red and the green channels. The PCC has the advantage of being independent from the offset and background in the

analysed channels (see 6.5.5). The wild-type constructs CD81-RFP and CD81-GFP yielded a high correlation coefficient and were enriched in the same domains (figure 24A), which confirms that cells did not discriminate between red- and green-labelled constructs and packed both together. Substitution mutations of the six juxtamembrane cysteines for alanines which suppress palmitoylation did not show major effects on co-clustering (figure 24C). This indicates that palmitoylation plays a secondary role in CD81 clustering. The deletion of the α- and β-helical domains, which make up almost half of the LEL, should strongly affect the structural conformation of the rest of the helices (see figure 23B). Even though the protein was so strongly modified, it was still able to enrich into CD81 microdomains (figure 24C). This suggests that the described dimerization via the αβ-region (Drummer et al., 2005; Kitadokoro et al., 2001; Kitadokoro et al., 2002) is not essential for domains integration. The variable domain of the LEL was described to play the major role in protein-protein interactions and functions. I thus expect that deletion of the variable domain thoroughly affects domain co-clustering. Indeed, upon deletion of the variable region and its two flanking cysteines (Δ 156 – 190; see figure 23B; Kitadokoro et al., 2001; Levy & Shoham, 2005a) the domain targeting was strongly decreased (figure 24C). The variable region is composed of two helical domains separated by a disulfide bridge, the γ-domain (Δ 156 – 174) and the δ-domain (Δ 176 – 186) see (figure 23B) (Kitadokoro et al., 2001). Deletion of the γ-domain did not affect domain co-clustering and the construct almost maintained wild-type behaviour, whereas deletion of the δ-domain alone decreased domain targeting to a level similar to that seen when deleting the entire variable region (figure 24B and C). This observation indicates that the δ-domain is essential for domain targeting. Therefore, the clustering and assembling of CD81 into CD81 enriched microdomains is driven by the δ-domain.

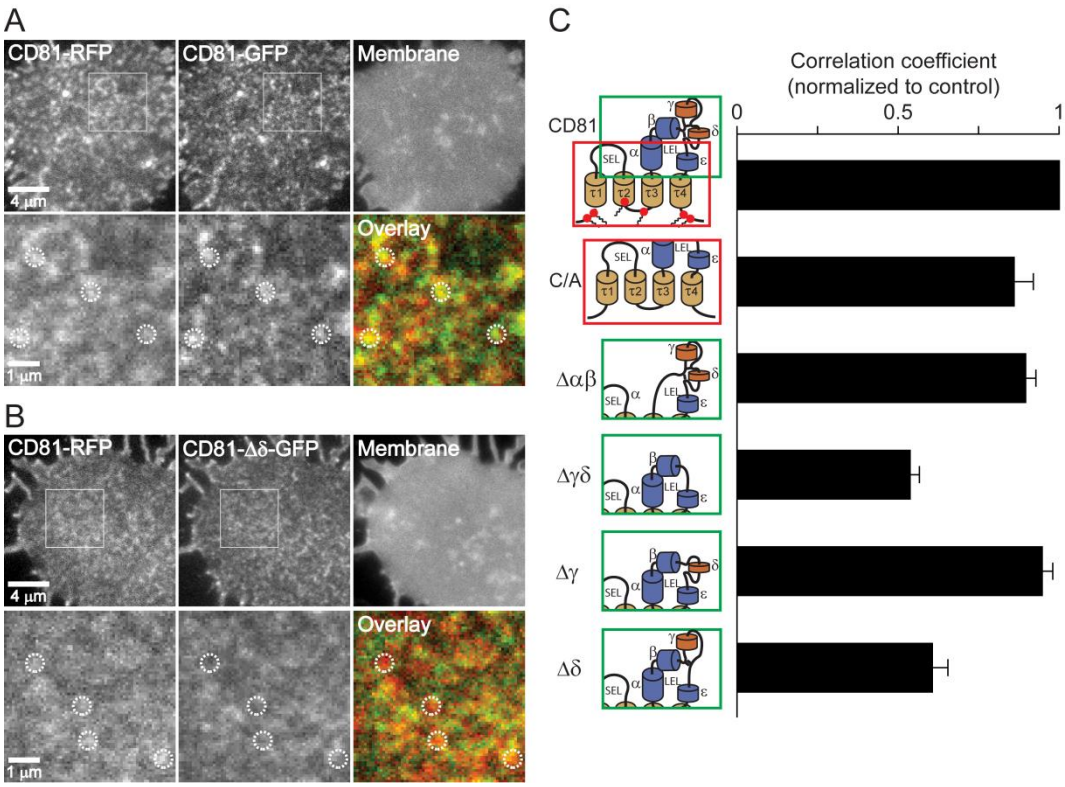

Figure 24. The δ-domain is required for targeting CD81 into CD81-enriched microdomains.

Membrane sheets generated from Jurkat cells were co-transfected with wild-type CD81-RFP and either wild-type CD81-GFP (A) or CD81-Δδ-GFP (B). Images were recorded in the red (RFP), green (GFP) and blue (TMA-DPH for membrane visualisation) channel. The wild-type versions of CD81 tagged either with RFP (CD81-RFP) or GFP (CD81-GFP) are assembled in the same domains. In contrast, deletion of the δ-domain strongly affects colocalization of CD81-Δδ-GFP and full-length CD81-RFP. Dotted circles mark identical localizations and indicate protein clusters in the RFP, GFP and overlay micrographs which overlap in A and do not overlap in B. (C) The bar chart compares the PCC between the maximum colocalization observed with CD81-RFP/CD81-GFP (set to 1) and modified colocalizations by CD81-RFP/GFP-labelled CD81 variants. The constructs are represented in the pictograms (derived from figure 10 and 7.4) from top to bottom: CD81, wild-type; C/A, all palmitoylation site of juxtamembrane cysteines were substituted with alanines; Δαβ, Δγδ, Δγ and Δδ, deletion of the respective domains of the LEL. Red solid circles with acyl chains represent cysteine palmitoylation sites. The bar chart shows the mean PCC ± SE (n = 3 – 10 independent experiments); for each experiment 5 – 22 membrane sheets were averaged and normalized to control CD81-GFP (derived from Homsi et al., 2014).

7.6 All CD81 constructs show comparable cell surface expression levels

The expression levels observed on membrane sheets analysed in figure 24 was slightly variable, making it possible that differences in co-

clustering are not due to domains deletion/mutation but intrinsically different expression levels. To exclude this possibility, the fluorescence intensities from the analysed membrane sheets were determined to compare overexpression levels of mutated constructs compared to the control (wild-type CD81). I calculated the relative fluorescence intensity after background correction in the green and red channel of each individual membrane sheet. The determined values were binned and plotted as intensity distribution histograms (figure 25). The frequency of the fluorescence intensities shows both a comparable width of distribution between each construct and its respective control and also comparable overexpression levels for all constructs. This result confirms that the effect seen in figure 24 is not caused by differing expression levels. In addition, western blot analysis experiments in Jurkat cells showed also comparable expression levels between CD81-GFP and CD81-$\Delta\delta$-GFP; moreover, no degradation products were observed for both constructs (see Appendix 1 B and Appendix 2).

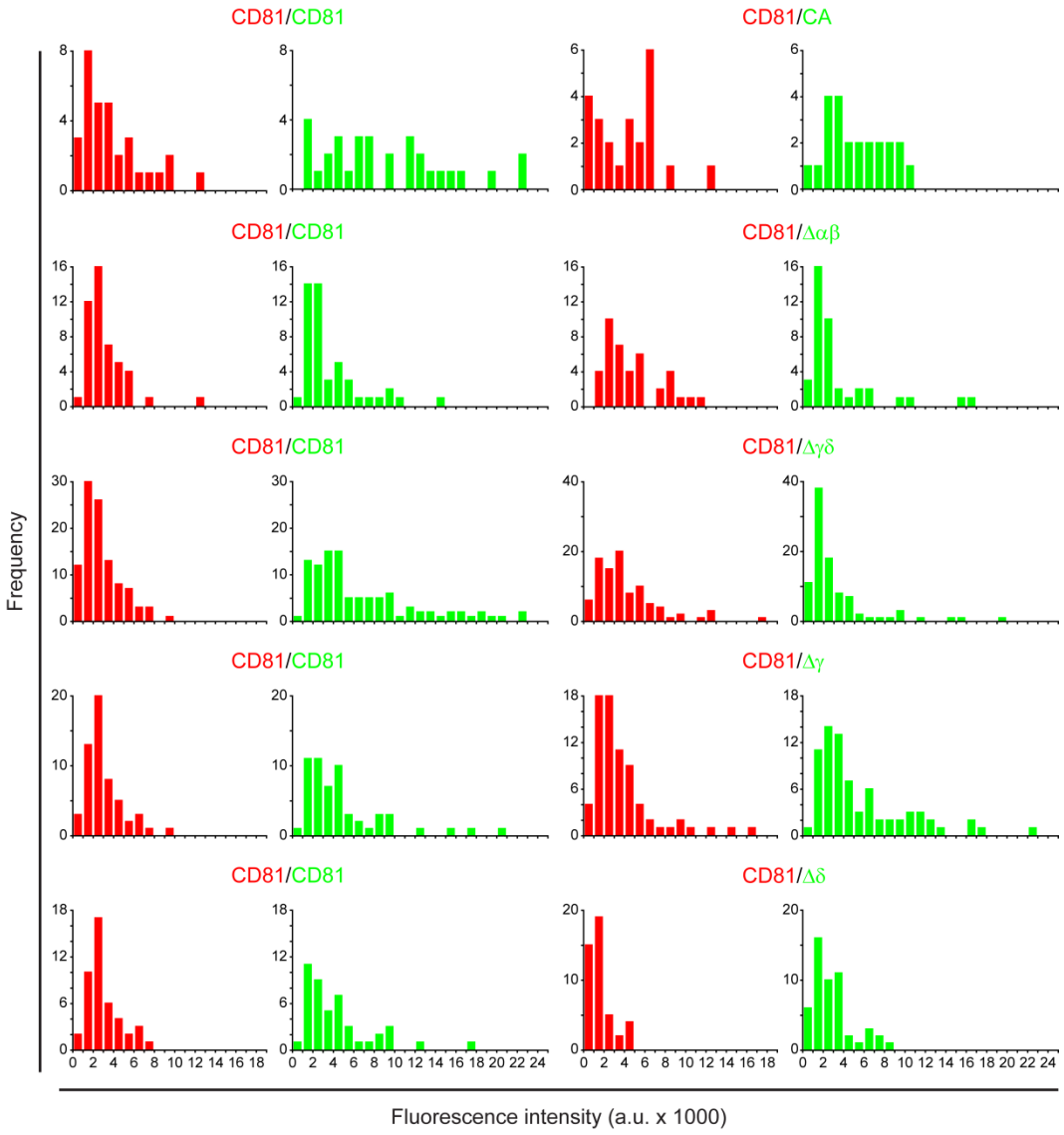

Figure 25. Expression level distributions of CD81-RFP/CD81-GFP and CD81-RFP/GFP-labelled constructs in individual membrane sheets.

Histograms show the frequency distribution of the fluorescence intensities in the red (RFP) or green (GFP) channel from individual membrane sheets. Plots illustrate absolute frequency counts of individual event intensities within 1000 a.u. bin width starting at 0. Note that the exposure time in the red channel was two-fold the green channel (see 6.5.3). All analysed membrane sheets from different experiments of the respective construct and its appropriate control were pooled together. Each panel shows two red/green histogram pairs; first pairs show CD81-RFP/CD81-GFP control to which the averaged PCC of the tested construct shown in the second histogram pairs were normalized (derived from Homsi et al., 2014).

7.7 CD81-GFP and CD81-Δδ are similarly distributed and mainly found at the cell membrane in living Jurkat cells

The CD81-Δδ is the most important construct analysed in figure 24 because it showed the most profound effect on CD81 domain targeting (figure 24B and C). This effect was not due to different overexpression levels compared to wild-type CD81-GFP (figure 25). Next, I set out to analyse the subcellular distribution of CD81-Δδ-GFP compared to wild-type CD81-GFP, since mutations could involve the risk of disturbed protein trafficking from the intracellular compartments such as Golgi apparatus or the endoplasmatic reticulum to the plasma membrane. This could ultimately lead to retention of the protein in these subcellular structures. Using confocal laser scanning microscopy, I was able to check the distribution of the overexpressed protein in living Jurkat cells transfected either with CD81-GFP or CD81-Δδ-GFP. The confocal scans verify that CD81-Δδ-GFP and CD81-GFP show a similar subcellular distribution; none of the proteins is strongly retained in the subcellular compartments (figure 26). The results represented in (figures 25 and 26) confirm that CD81-Δδ-GFP similar to CD81-GFP reaches the cell surface. This observation reinforces the specific effect of the δ-domain deletion seen in (figure 24).

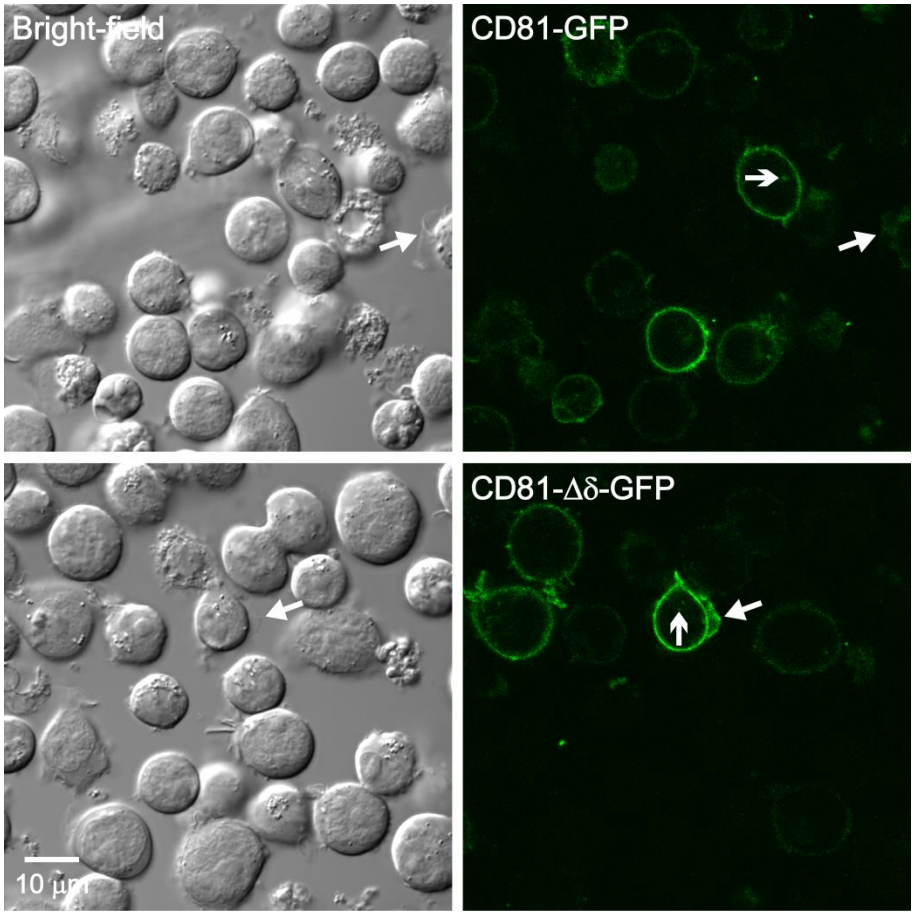

Figure 26. CD81-GFP and CD81-Δδ-GFP distribution in live Jurkat cells

Suspension of live Jurkat cells expressing either CD81-GFP or CD81-Δδ-GFP imaged with confocal microscopy after cell sedimentation onto uncoated glass coverslips in pre-warmed Ringer solution at RT. Upper panel, cells expressing CD81-GFP; lower panel, cells expressing CD81-Δδ-GFP; left, bright-field overviews; right, confocal micrographs in GFP channel. GFP expression was almost exclusively found at the plasma membrane showing a ring-like pattern for both constructs indicating that the overexpressed proteins were nearly all located at the plasma membrane. Some cells formed lamellipodia detected as green extensions seen also in the bright-field image (compare closed arrows in both pictures). Only in some cases, a weak intracellular accumulation of GFP signal (indicated by open arrows) was observed, which probably represents CD81 retention in the Golgi apparatus (Mittelbrunn et al., 2002). Images are shown at arbitrary scalings from one representative experiment out of four experiments in total (derived from Homsi et al., 2014).

7.8 Immunoprecipitation of endogenous CD81 is less efficient with CD81-Δδ compared to wild-type CD81

The lacking overlap between CD81-RFP and CD81-Δδ-GFP suggests that both proteins interact less efficiently compared to CD81-RFP/CD81-GFP. To validate the crucial effect of the δ-domain deletion seen with a

microscopic assay, I performed immunoprecipitation experiments to study the interaction ability of the CD81-Δδ with endogenous CD81. Jurkat T cells overexpressing either CD81-GFP or CD81-Δδ-GFP were solubilized with the mild detergent CHAPS to preserve tetraspanin-tetraspanin interactions (Charrin et al., 2009; Yáñez-Mó et al., 2009). Endogenous CD81 was successfully precipitated via CD81-GFP with GFP-Trap® A beads, whereas CD81-Δδ-GFP was far less able to pull down endogenous CD81 (figure 27A), albeit it was efficiently pulled down by beads. Comparative quantification of pulled down endogenous CD81 via either CD81-GFP or CD81-Δδ-GFP show a ~70 % decrease upon deletion of the δ-domain (figure 27B). However, the remaining weak band of the precipitated CD81 that is observed when using CD81-Δδ-GFP suggests that both proteins are still able to interact, possibly via their α/β-domains. It thus appears that the interaction between CD81 proteins is mainly δ-domain dependent. The immunoprecipitation results in combination with the microscopy observations seen in figure 24, where CD81-Δδ-GFP is less enriched in CD81 domains, indicates that the deletion of the δ-domain affects possibly CD81 dimerization (in this case independently from α/β-domains) or disturbs the interaction with other TEM components which causes the loss of the clustering pathway and leads to the missorting of the domain targeting. In addition, dimerization may be essential for domain targeting and it could be the first step of TEM formation.

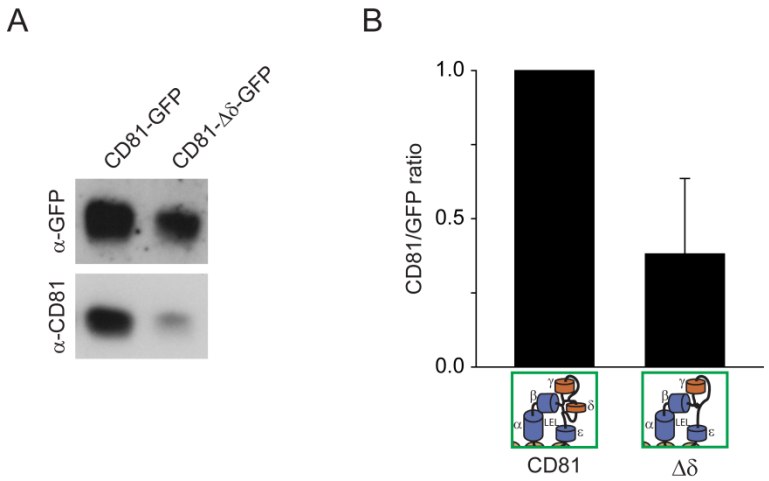

Figure 27. Immunoprecipitation of endogenous CD81 with either overexpressed CD81-GFP or CD81-Δδ-GFP

10^7 Jurkat cells expressing either CD81-GFP or CD81-Δδ-GFP were lysed in 1 % CHAPS lysis buffer and used for immunoprecipitation. (A) Upper panel, immunoprecipitated CD81-GFP and CD81-Δδ-GFP using GFP-Trap® A beads were detected via immunoblotting with anti-GFP. Lower panel, co-precipitated endogenous CD81 detected by immunoblot anti-CD81. (B) The ability of CD81-GFP or CD81-Δδ-GFP to co-precipitate endogenous CD81 was quantified by calculating the ratios between the endogenous CD81 band and the band of the co-precipitated overexpressed GFP-construct. In some experiments, the input levels of both constructs were not the same; to correct for this variation the CD81/CD81-Δδ-GFP ratio was normalized to the ratio of CD81/CD81-GFP and plotted in a histogram, showing a huge decrease in the ability of CD81-Δδ-GFP to precipitate endogenous CD81 compared to CD81-GFP. Values are given as mean ± SD (n = 3 independent experiments) (derived from Homsi et al., 2014). Western blot analysis and quantification were done in collaboration with Dr. Konstanze Scheffer and Dr. Luise Florin from the University of Mainz.

7.9 The CD81 δ-domain is essential for protein partner interaction

Immunoprecipitation experiments on cells solubilized under mild detergent treatment using CHAPS indicated that the δ-domain is a prerequisite for CD81-CD81 interaction/dimerization. Next, I performed additional immunoprecipitation experiments to study the effect of δ-domain deletion on protein partner interactions using similar conditions as in (figure 27). Cell lysates containing similar levels of endogenous CD81 and CD9 as well as comparable amounts of overexpressed CD81-GFP or CD81-Δδ-GFP (figure 28A), were used for an immunoprecipitation pull down assay for GFP-tagged proteins. The immunoprecipitation experiment showed

that upon deletion of the δ-domain, CD81-Δδ-GFP was not able to precipitate neither endogenous CD9 nor endogenous CD81 (as seen before (figure 27A)). In contrast, wild-type CD81-GFP pulled down both endogenous CD81 and CD9 (figure 28B). This confirms that the δ-domain is crucial for partner protein interaction.

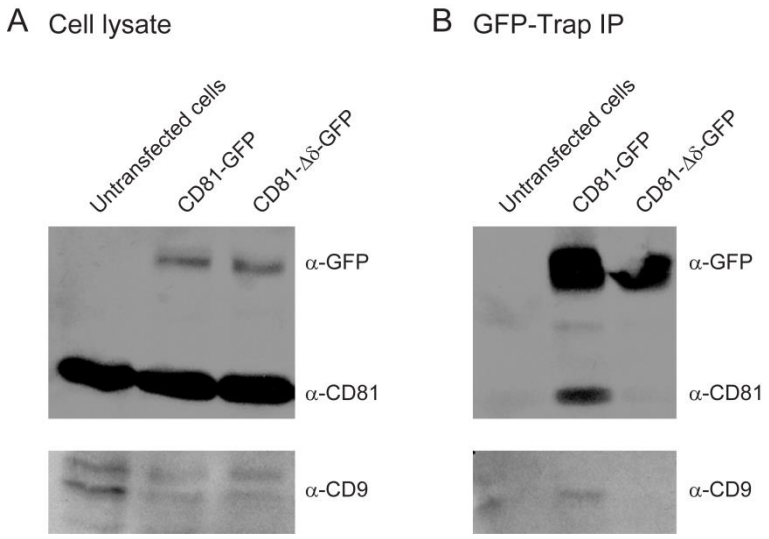

Figure 28. Immunoprecipitation of endogenous CD9 and CD81 via either overexpressed CD81-GFP or CD81-Δδ-GFP.

10^7 Jurkat cells expressing either CD81-GFP or CD81-Δδ-GFP were lysed in 1 % CHAPS lysis buffer (EWI/2-RFP was also co-expressed). (A) Cell lysate used directly as input, showing similar expression levels of overexpressed CD81-GFP and CD81-Δδ-GFP as well as of endogenous CD81 and CD9. (B) Material pulled-down from GFP-Trap® A beads showing a huge decrease of the precipitated endogenous CD81 via CD81-Δδ-GFP when compared with CD81-GFP. The interaction of CD81-Δδ-GFP with endogenous CD9 was almost completely abolished when compared to CD81-GFP. Immunoblotting was done in collaboration with Dr. Konstanze Scheffer and Dr. Luise Florin from the University of Mainz.

7.10 δ-domain dependent CD81 microdomain assembly is also observed in HepG2 cells

The effect of the δ-domain deletion on CD81 domain targeting seen in Jurkat cells (figure 24) was observed both in a microscopic assay figure 24 and by immunoprecipitation figures 27 and 28. To exclude that this mechanism exists only in one cell type, I repeated the assay of wild-type and mutant CD81 co-clustering with HepG2 cells. Similar to Jurkat cells, co-clustering was strongly reduced when the δ-domain was deleted figure

29. As for Jurkat T cells, CD81-Δδ in HepG2 cells was sorted into distinct clusters from wild-type CD81 (figure 29B). In addition, CD81-Δδ was not uniformly distributed, but clustered in separate structures in both cell lines though rather less clustered structures were observed in HepG2 cells. From the microscopic and biochemical observations, I conclude that the targeting of CD81 into CD81 domains is essentially driven by the δ-domain independently from the cell type, while other LEL domains and palmitoylation are not a prerequisite, but may play a secondary role.

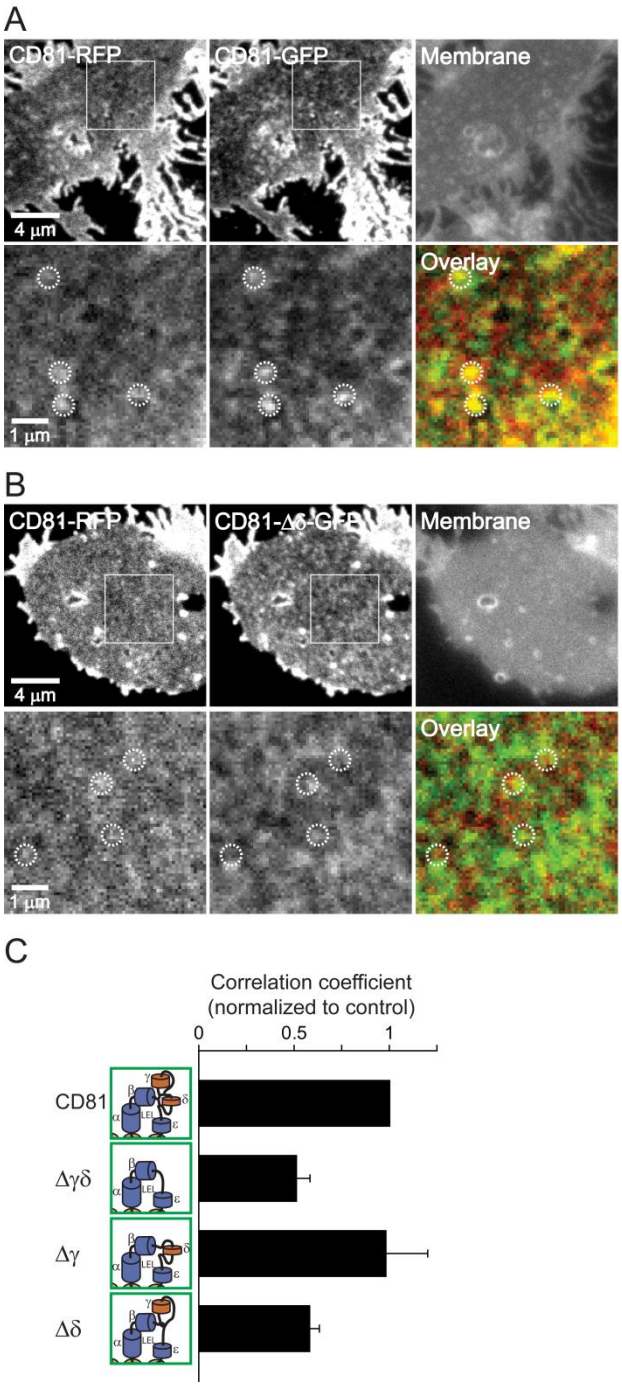

Figure 29. Clustering of CD81 into CD81 enriched domains in HepG2 cells

Membrane sheets generated from HepG2 cells co-transfected with wild-type CD81-RFP and either wild-type CD81-GFP (A), CD81-Δγδ-GFP, CD81-Δγ-GFP or CD81-Δδ-GFP (B). Samples were recorded, presented and analyzed as described in figure 24. The high colocalization observed for wild-type CD81-RFP and wild-type CD81-GFP (A) was lost when using CD81-Δδ-GFP (B). Dotted circles indicate identical regions in the images. (C) The PCC was analysed as described in figure 24 and is shown as mean ± SE (n = 3 – 5 independent experiments, in each 5 – 19 membrane sheets were averaged and normalized to control). For pictogram description see the legend of figure 24 (derived from Homsi et al., 2014).

7.11 Lateral diffusion of CD81 is regulated by the δ-domain

In the experiments described so far, I analysed CD81 domain targeting from a static viewpoint. In the following, I aimed to study CD81 domain behaviour over time using a dynamic approach. The specific features of TEMs or large tetraspanin webs are their circular shape and their stable position (Barreiro et al., 2008; Espenel et al., 2008). Therefore, TEM structures (formed by CD81) should be, in comparison to non-TEMs (formed by CD81-Δδ), less dynamic and more stable in shape and position. Consequently, I studied the apparent lateral diffusion of CD81 or CD81-Δδ by applying FRAP measurements in living cells (figure 30). Living Jurkat cells overexpressing either CD81-GFP or CD81-Δδ-GFP were adhered on poly-L-Lysine coated coverslips and recorded in pre-warmed Ringer solution at RT. CD81-Δδ diffused into the bleached area faster than wild-type CD81 (figure 30A and B). Consequently, I calculated the apparent lateral diffusion coefficients for CD81 and CD81-Δδ. The determined diffusion coefficient value for CD81 was 0.03 $\mu m^2/s$ which is comparable to previously published values in polarized (0.07 $\mu m^2/s$) and non-polarized (0.11 $\mu m^2/s$) HepG2 cells (Harris et al., 2013). The lower value I determined here in Jurkat cells may be caused by differences in domain size between Jurkat and HepG2 cells (domain size should be higher in Jurkat cells). This point could be addressed in further experiments studying the size of clusters (see figures 36 and 39). In contrast, CD81-Δδ showed a strongly increased diffusion coefficient (figure 30C). These results indicate that restriction in lateral diffusion of CD81 is dependent on the δ-domain.

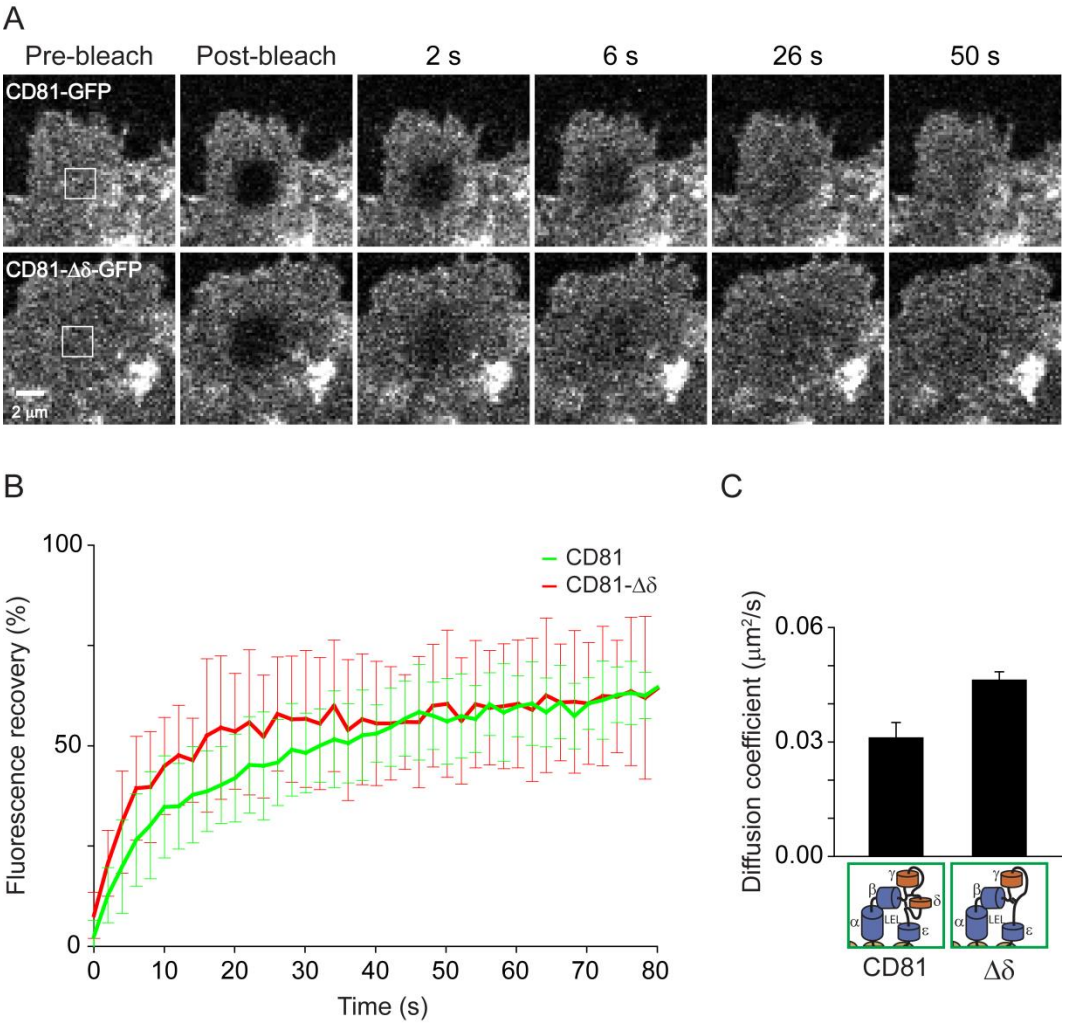

Fiugure 30. Determination of CD81-GFP and CD81-Δδ-GFP apparent lateral diffusion coefficients via fluorescence recovery after photobleaching (FRAP) measurements in living Jurkat cells

(A) Live Jurkat cells were adhered on poly-L-Lysine pre-coated glass coverslips expressing CD81-GFP (upper panel) or CD81-Δδ-GFP (lower panel) and were recorded at 0.5 Hz in pre-warmed Ringer solution at RT. Image sequences of living Jurkat cells shown from left to right, before bleaching (pre-bleach) of a bleaching area indicated by the white square ROI (10 x 10 pixel; ~2.1 µm x 2.1 µm), after bleaching (post-bleach) and at 2, 6, 26, and 50 s after bleaching, indicating the fluorescence recovery of the bleached area by diffusion mediated substitution of bleached with unbleached molecules from the neighborhood. (B) FRAP recovery curves of CD81-GFP (green) and CD81-Δδ-GFP (red) showing a faster recovery of CD81-Δδ-GFP comparing to CD81-GFP. For each independent experiment, the averages of the background corrected normalized recovery traces of 3 – 11 cells were calculated and plotted over time (average traces of one day shown in B; error bars illustrate the standard deviation between individually measured cells; (A) represents one measurement of CD81-GFP and one of CD81-Δδ-GFP derived from B). The plotted scatters were fitted to determine the half-times of the fluorescence recovery that was used to calculate the lateral diffusion coefficients (for more details see 6.3.3.2). (C) Calculated diffusion coefficients of CD81-GFP and CD81-Δδ-GFP indicating an increase of the lateral diffusion for CD81-Δδ-GFP. Values are given as mean ± SE (n = 4 independent experiments) (derived from Homsi et al., 2014).

7.12 CD81 domain stability and dynamics are controlled by the δ-domain

As described in the previous paragraph 7.11, TEMs or large tetraspanins webs are stable in shape and position. Next, I studied CD81 and CD81-Δδ domain stability by exanimating cluster dynamics using TIRF microscopy. As in figure 30, I performed similar experiment on living Jurkat cells using TIRF microscopy which enables studying domain stability and behaviour over time. Almost all observed CD81 domains were stable over seconds (figure 31A). In contrast, CD81-Δδ clusters showed high instability even between two successive frames of a 0.5 s time interval (here I show images separated by 1.5 s time interval); therefore they may translocate and/or disassemble very quickly (figure 31B). Moreover, the analysis of the whole recorded frames in (figure 31A and B) for CD81 and CD81-Δδ, respectively, showed constant domain stability for CD81 and constant domain instability for CD81-Δδ over time (see figure 31C and D). The deletion of the entire variable region did not further change the dynamics of clusters. In contrast, upon deletion of the γ-domain alone the platforms retained their stability and behaved comparably to wild-type CD81 (figure 31E). The observed effects of the δ-domain on cluster stability, dynamics, targeting and interaction confirm that CD81 is enriched in stable platforms or larger TEMs and that its interaction with other TEM components is driven by the δ-domain.

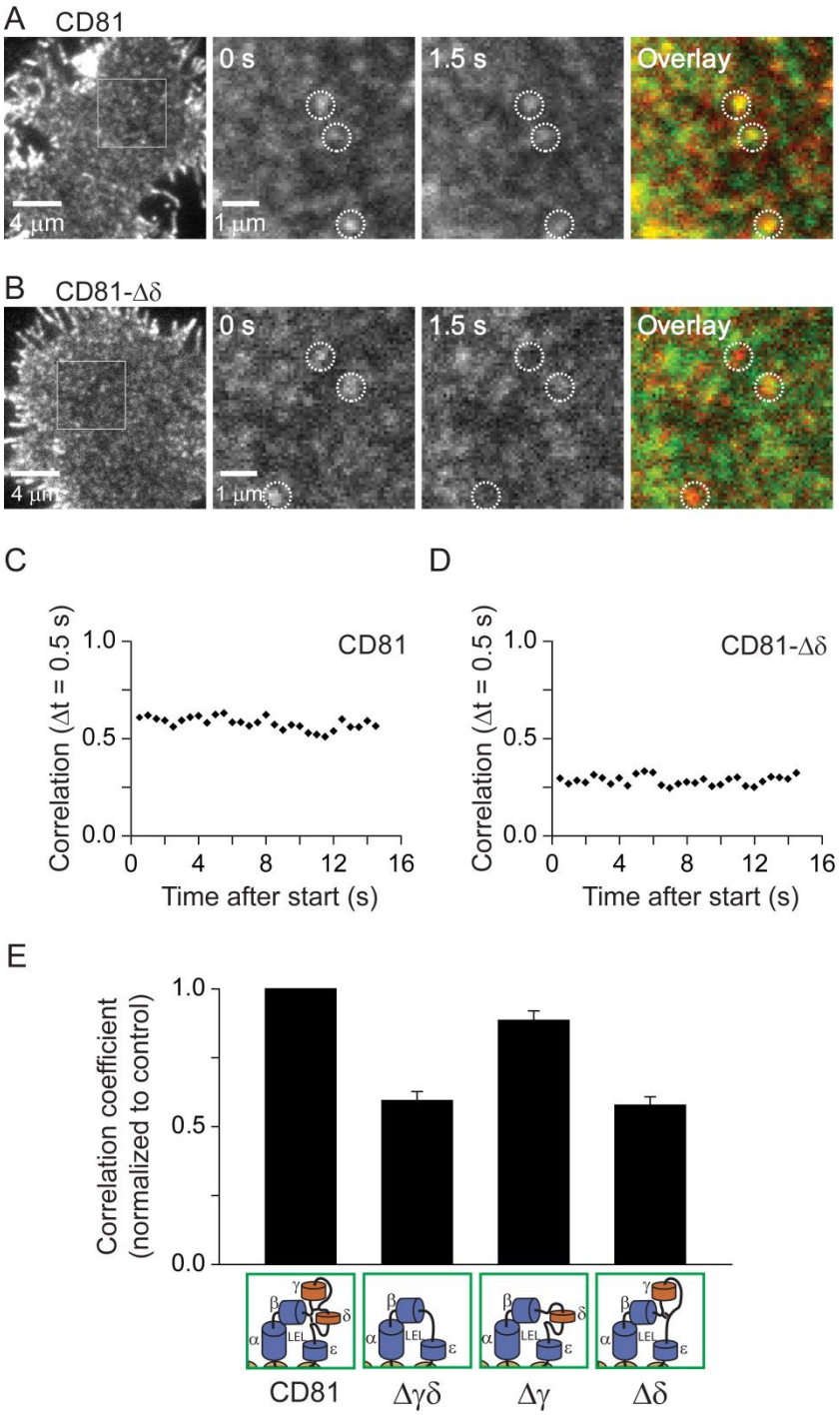

Figure 31. Cluster immobilization assay to study CD81 and CD81 deleted δ- and/or γ-domain dynamics

Live intact Jurkat cells overexpressing CD81-GFP (A) or CD81-Δδ-GFP (B) were adhered on pre-coated glass coverslips and imaged at 2 Hz in pre-warmed Ringer solution at RT using TIRF microscopy. (A and B) Starting from left, overview of the imaged cell followed by two magnified views of the white squared ROIs (indicated in the overview image) from two recorded images separated by 1.5 s and overlay. Wild-type CD81 domains remain unchanged over time while CD81-Δδ-GFP are fluctuating. Dotted circles mark domains in the first image and were transferred to identical regions in the second image. Note that the yellow color indicating overlap is mainly observed for wild-

type CD81. (C and D) For the entire movies the PCC between two successive frames was determined and the values were plotted against the recording time of the second image of the correlated pair. Plots in C and D are derived from the recordings in A and B, respectively, illustrating the high lateral dynamics over time seen by CD81-Δδ-GFP (D) compared to CD81-GFP (C). (E) Cells expressing GFP-labeled CD81, CD81-Δγδ, CD81-Δγ or CD81-Δδ were recorded as described above; at each time point the average PCC was calculated and for each construct the mean of the entire averaged traces was calculated. Values are given as mean ± SE (n = 4 independent experiments; for each experiment 5 – 8 cells were averaged and normalized to control) (derived from Homsi et al., 2014).

7.13 Association of CD81 with CD9 requires the CD81 δ-domain

I elevated the concentration of CD9 in combination with either CD81 or CD81-Δδ and tested the association of CD81/CD81-Δδ with CD9 domains. Compared to the overlap with CD81 wild-type seen in figure 24, I found that CD81 overlapped less with CD9 and in general less colocalized domains were observed in both channels (figure 32A) indicating that the interaction of CD81 with CD9 is secondary. PCC quantification shows upon deletion of the δ-domain a strongly decreased overlap (figure 32B). These microscopy observations not only suggest that the interaction with CD9 is secondary, as shown before with the biochemical approach (Serru et al., 1999), but also indicate that the association is δ-domain dependent. Moreover, the association of CD81 and CD9 may occur mainly within TEMs, since the enrichment of CD81 and CD9 in the same domains indicates the presence of large tetraspanin complexes (Hemler, 2005; Rocha-Perugini et al., 2013; Rubinstein et al., 1996; Serru et al., 1999).

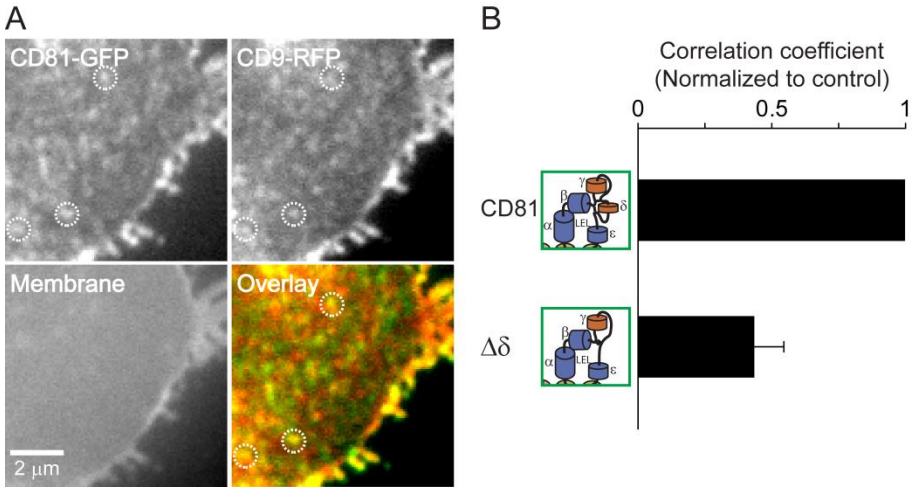

Figure 32. The interaction between CD81 and CD9 is δ-domain dependent

(A) Membrane sheet generated from a Jurkat cell co-overexpressing CD81-GFP and CD9-RFP. Upper panel, recordings in the green and red channels visualized CD81-GFP and CD9-RFP, respectively; lower panel, membrane stained by the lipid dye TMA-DPH and overlay of the images in the upper panel. (B) The co-localization of CD81-GFP or CD81-Δδ-GFP with CD9-RFP was analysed by PCC calculation as described in figure 24. The deletion of the δ-domain strongly decreased the PCC. Dotted circles indicate identical pixel locations. Values are given as means ± SE (n = 3 independent experiments; for each experiment and condition values from 13 – 20 membranes sheets were averaged and the mean of CD81-Δδ-GFP was normalized to control) (derived from Homsi et al., 2014).

7.14 Autocorrelation analysis as a suitable tool for estimating average radial sizes

For several questions an unbiased method for measuring the average size of membrane domains is required. To this end I turned to autocorrelation analysis for analysis of a variety of questions. This method was validated in this work using beads in different sizes and numbers (figure 33A). Bead size was determined via full width at half maximum (FWHM) approach (figure 33B) or autocorrelation approach ((figure 33C); 2 x 50 % autocorrelation). Both approaches delivered comparable values indicating that the autocorrelation analysis is suitable for determining cluster sizes. In conclusion, autocorrelation analysis delivered an acceptable value to estimate average radial size or to at least detect size trends.

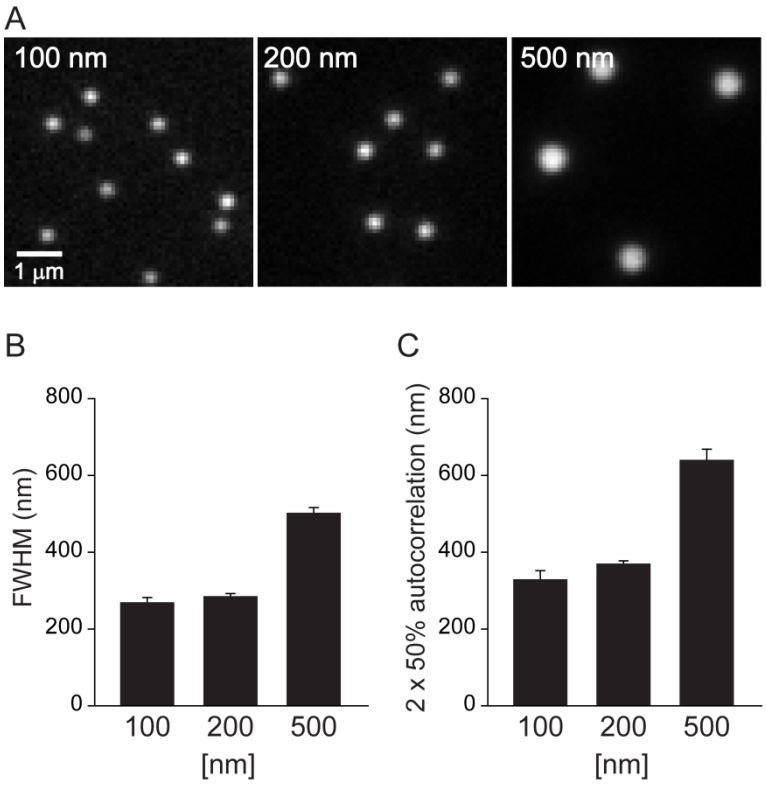

Figure 33. Autocorrelation analysis a convenient tool to measure average size

(A) 100 nm, 200 nm or 500 nm beads were imaged in the green channel and analyzed within a region of interest with a variable number of beads, by linescans (B) and autocorrelation analysis (C). (B) The linescan measurements of individual beads were plotted and fitted using Gaussian formula. Fitted curves were used to determine the full width at half maximum (FWHM), which corresponds to the size of the bead. The determined FWHM values of all beads in one image were averaged. For each bead size five images were analyzed and the means of the averaged FWHM values were calculated. Values are given as means ± SD (n = 5 individual images). (C) The autocorrelation analysis was performed by calculation the PCC between the initial ROI and duplicated ROIs after one pixel shift in the same direction starting by the initial position, yielding 1 and performed to reach a value close to zero (see 6.5.5). The object size is proportional to the pixel shift needed to decrease the correlation coefficient to 50 %, at which the shift is a rough estimate of the average radial size of all particles in the analyzed image. To facilitate the comparison of FWHM values, which refer to the diameter, with the autocorrelation values, I multiplied the autocorrelation values by 2. I noticed that the point spread function of the fluorescence microscope blurs the bead size; this effect was especially seen for bead sizes in the range of the microscope resolution limit (100 nm and 200 nm beads). The autocorrelation measurements were comparable to those resulted from the FWHM approach with an acceptable overestimation of 10 – 20 %. Consequently the measured values do not represent physical absolute values, but rather allow to estimate size and to detect trends of size differences (derived from Homsi et al., 2014).

7.14.1 Autocorrelation analysis suggest that CD81 regulates cluster distribution within the cell membrane

As mentioned above, tetraspanins play an important role in different cellular processes including mobility, morphology and adhesion (see 4.4). In addition, several reports described that CD81 regulates protein organization and cluster distribution within the cell membrane, so that tetraspanins are considered as master organizers of the plasma membrane (Cambi & Lidke; Hemler, 2005). The results shown in figure 31 indicate that upon deletion of the δ-domain CD81-Δδ clusters showed high instability and highly disordered distribution (figure 31B and D). Interestingly, disordered integrin clusters were observed upon CD81 depletion. In a collaboration with Dr. Thomas Quast from the Kolanus' laboratory (University of Bonn), dendritic cells (DCs) derived from human monocytes (Mo-DCs) were treated with siRNA to knockdown CD81 (for more information see Quast et al., 2011). Intact Mo-DCs treated either with control siRNA or CD81 siRNA were stimulated with lipopolysaccharide (LPS), adhered onto fibronectin-coated coverslips, fixed, immunostained for the integrin CD29 and imaged using epi- and TIRF-microscopy (Quast et al., 2011). In contrast to the homogenous localization of CD29 clusters seen with control siRNA (figure 34A, upper panels), CD81 siRNA treated cells showed a disordered accumulation of CD29 clusters in the plasma membrane (figure 34A, lower panels). For studying CD29 integrin cluster size and shape, TIRF images were used which have better resolution and higher quality (high signal to noise ratio) (figure 34A, right panels and magnified views). CD29 cluster sizes at central and peripheral regions of the cell were analysed using the autocorrelation analysis (for more information see 6.5.5 and figure 33). The analysis showed no significant differences in size between CD29 clusters after depletion of CD81 (CD81 siRNA) (figure 34B). Moreover, CD29 cluster size and distribution were similar between central (figure 34B, left panel) and peripheral membrane regions (figure 34B, right panel). Though their size was in the rage of diffraction limit and it cannot

be entirely excluded a possibility of minimal size changes. These observations indicate that upon CD81 depletion, CD29 clusters retain their size, but lose their correct distribution. These observations are in line with previous reports confirming that CD81 organizes cluster distribution in the cell membrane and that tetraspanins play a role as master organizers of the cell membrane.

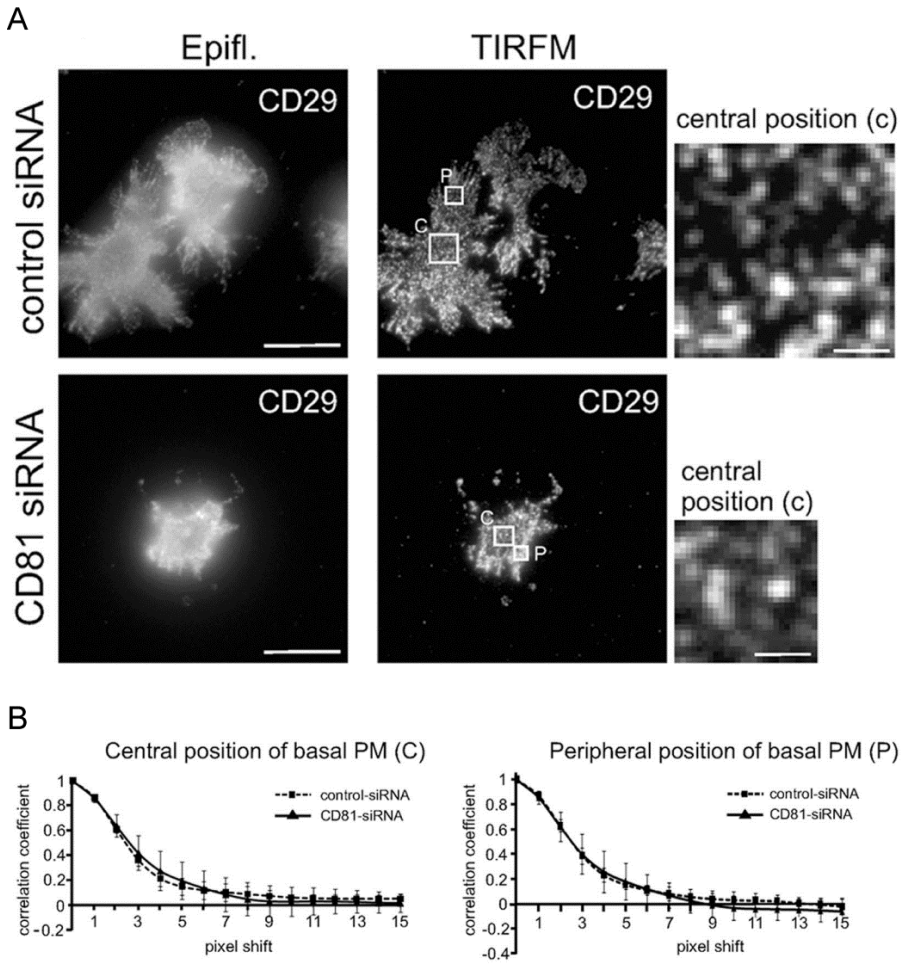

Figure 34. CD81 organizes CD9 cluster distribution in the cell membrane

(A) Intact Mo-DCs treated with either control siRNA (upper panels) or CD81 siRNA (lower panels), were stimulated with LPS, fixed, immunostained for CD9 and adhered onto fibronectin-coated (5 µg/cm^2) glass coverslips. Cells were imaged via epifluorescence (left panels) or TIRF (right panels and magnified views) microscopy. White ROIs indicate regions analyzed by autocorrelation analysis in the central 50 x 50 pixels ((c), further magnified at the right side) and peripheral 20 x 20 pixels (p) positions. Scale bars represent 10 and 1 µm for overviews and magnified views, respectively. (B) Autocorrelation decay curves of CD29 clusters in the central (right) and peripheral (left) regions of the basal plasma membrane (PM). For autocorrelation analysis, the image within a ROI was duplicated and correlated with the original position starting at 1 and then correlated with new positions after displacement pixel-wise up to 15 pixels (for more details see 6.5.5 and figure 33). This procedure was done in four different directions (up,

down, right and left). For each displaced pixel in all direction, four PCC values were averaged yielding an autocorrelation curve for the analyzed ROI. Finally, autocorrelation curves were averaged from five individual cells. Graphs show autocorrelation curves of control siRNA (dashed line) and CD81 siRNA (solid line); error bars represent standard deviation (n = 5). Pixel size was adjusted to 83.3 nm. Cells were prepared and immunostained by Dr. Thomas Quast (modified from Quast et al., 2011).

7.14.2 Autocorrelation analysis is able to answer various questions about protein clustering

In collaboration with Dr. Linda Diehl and Julita Kaczmarek (University Clinic of Bonn), a similar autocorrelation analysis (see figure 34) was performed to study the clustering behavior and distribution of the T cell receptor (TCR) and the lymphocyte function-associated antigen 1 alpha polypeptide (LFA-1 or CD11a). TCRβ and CD11a are recruited into cellular supra-molecular activation cluster (c-SMAC) and play an important role in cell-to-cell immune synapse (IS) formation (Kaczmarek et al., 2014). In brief, TCRβ and CD11a cluster size, distribution and density were studied on liver sinusoidal endothelial cells (LSEC), which are antigen-presenting cells (APC), derived either from wild-type mice (B6) or B7H1 immune response suppressor factor deficient mice ($B7H1^{-/-}$). LSEC cells were stimulated with ovalbumin (OVA) and incubated with naïve CD8 T cells for different incubation times (1, 4 and 24 h) and then fixed and immunostained for either TCRβ or CD11a (for more information see Kaczmarek et al., 2014). The same autocorrelation analysis like in figure 34 was performed showing that the lack of B7H1 signaling did not alter clusters size and distribution neither of TCRβ nor of CD11a (figure 35A). In addition, no significant difference in cluster density was observed for both TCRβ and CD11a between B6 and $B7H1^{-/-}$ cells (figure 35B). The results shown in figures 34 and 35 and validated in figure 33 indicate that the autocorrelation analysis can be used in a wide range of applications. It is further used for studying TEMs size and growth under different conditions (see figures 36 and 39). In addition, this simple method can build a bridge between the biophysical background and its biologic or physiologic effects. In conclusion, various interesting questions could be

addressed via autocorrelation analysis method, which could represent a general tool to study cluster size, behavior and distribution.

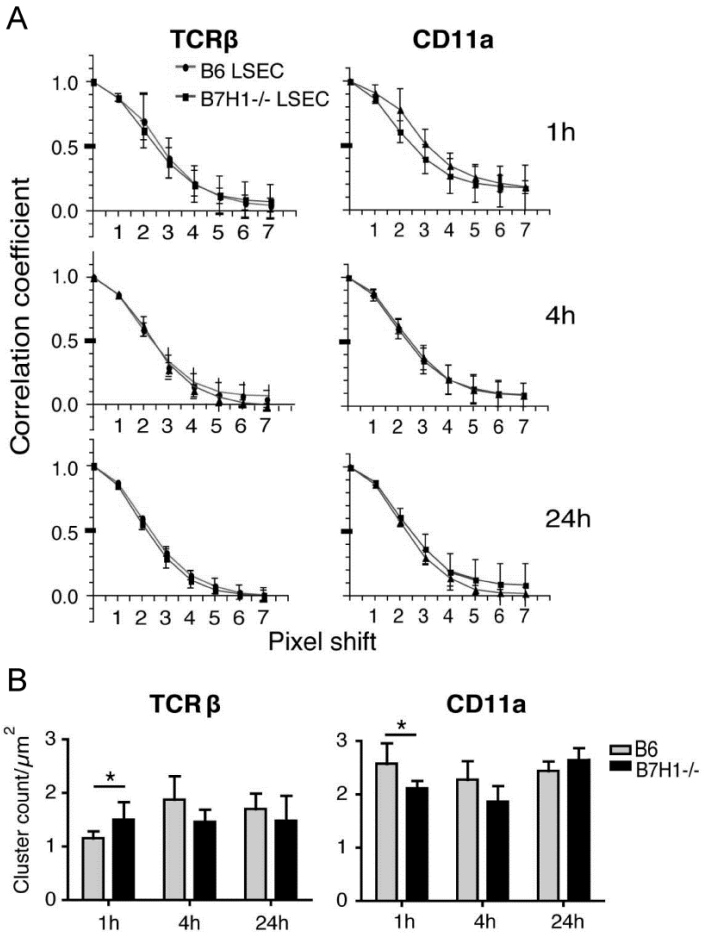

Figure 35. TCRβ and CD11a clusters distribution studied with autocorrelation analysis

B6 and B7H1$^{-/-}$ LSEC were stimulated with OVA co-cultured with naïve CD8 T cells for 1, 4 and 24 h, fixed and stained for either TCRβ or CD11a. (A) Autocorrelation decay curves (see figure 34) showed no changes in cluster size of TCRβ or CD11a between B6 LSEC (red line) and B7H1$^{-/-}$ LSEC (black line). One pixel represents 83.3 nm. Values are means of five cells (n = 5) and error bars represent standard deviation. (B) Clusters were counted within square ROIs of (~3.7 µm x 3.7 µm). No significant differences of cluster density were observed. Density is given as means ± SE (n = 5). Cells were prepared, immunostained and imaged by Dr. Linda Diehl and Julita Kaczmarek. *p≤0.05 (modified from Kaczmarek et al., 2014).

7.15 The CD81 δ-domain is required for large TEMs or tetraspanin webs and it is essential for primary interaction

Tetraspanins associate with Ig superfamily proteins to form TEMs (Boucheix & Rubinstein, 2001; Hemler, 2003; Stipp et al., 2003). EWI-2, related to the Ig superfamily, is a primary binding partner of CD81 which forms stable complexes with CD81 by direct protein-protein interaction with high stoichiometry (Charrin et al., 2003; Clark et al., 2001; Stipp, Kolesnikova et al., 2001; Stipp, Orlicky et al., 2001; Stipp et al., 2003). This direct interaction is mediated via the short cytoplasmic tail and the glycine-zipper motif in the TM from the EWI-2 side, and the TM3, TM4 and some additionally participation of the extracellular domains from CD81 (Homsi et al., 2014; Montpellier et al., 2011). In the following it was tested how an increase of EWI-2 affects the domains formed by CD81.

7.15.1 CD81 enrichment in large TEMs via the δ-domain and primary interactions

The concentration of EWI-2 was elevated to promote the generation of TEMs. I aimed to check whether CD81 and CD81-Δδ are able to establish primary interactions with EWI-2 to form complexes that incorporate further into TEMs. Jurkat cells co-overexpressing EWI-2-RFP and either CD81-GFP or CD81-Δδ-GFP were analysed as described in figure 24. CD81 and EWI-2 co-enriched in the same domains (figure 36A and C), indicating that within CD81 clusters primary interaction with EWI-2 lead to co-enrichment in TEMs. In contrast, CD81-Δδ clusters did not co-enrich/were not able to interact with EWI-2 indicating that CD81-Δδ clusters are not TEMs (figure 36B and C).

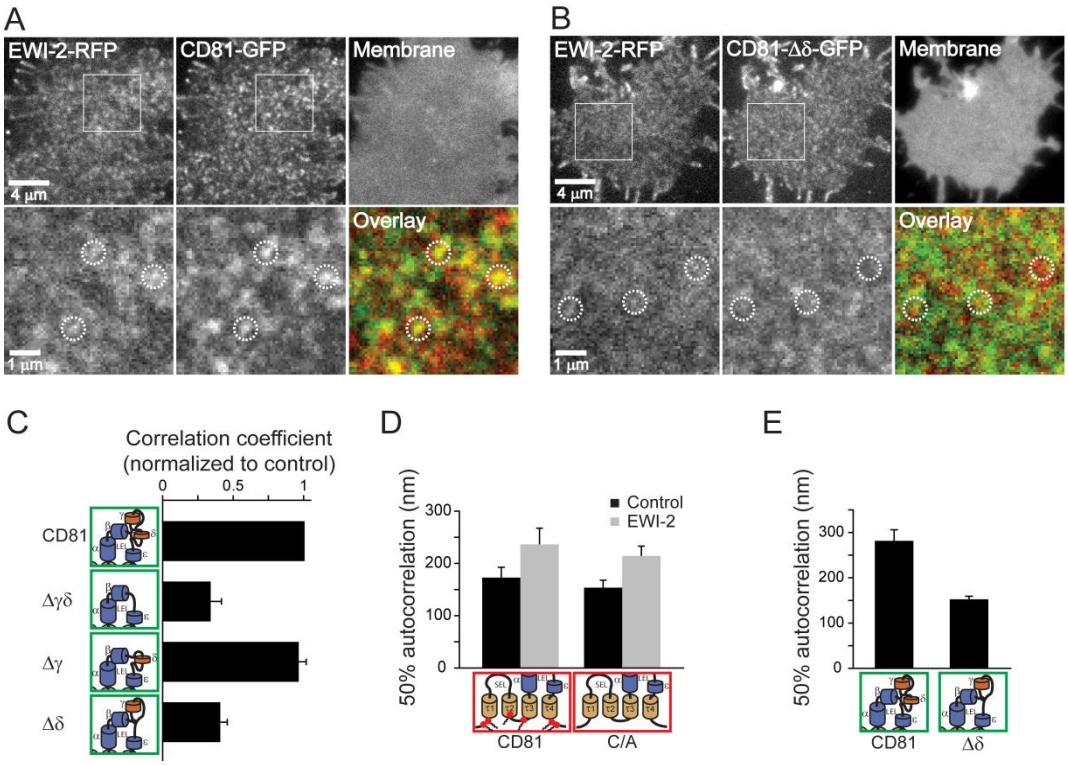

Figure 36. The CD81 δ-domain is necessary for building large TEMs

(A and B) Membrane sheets generated from Jurkat cells co-overexpressing EWI-2 (CD81 interaction partner) RFP-tagged together with CD81-GFP (A) or CD81-Δδ-GFP (B). Upper panels from left to right, membrane sheet imaged in red, green and blue channels to visualize EWI-2-RFP, CD81-GFP (A) or CD81-Δδ-GFP (B) and membrane integrity (using the lipid dye TMA-DPH), respectively. Lower panels from left to right, magnified views from the respective marked area of the white square ROIs in the upper panels and overlays. EWI-2-RFP showed a less clustered pattern when co-overexpressed with CD81-Δδ-GFP. Dotted circles indicate identical overlaps. (C) The co-localization between the green and the red signals was determined by calculating the PCC. The co-localization between EWI-2 and the clusters in the green channel strongly decreased specifically upon deletion of the δ-domain. Values are given as mean ± SE (n = 3 independent experiments; for each experiment values from 5 – 20 membrane sheets were averaged and normalized to control). (D) Autocorrelation analysis of cells expressing CD81-GFP or CD81-C/A-GFP without (black bars) or in combination with EWI-2-RFP (gray bars). Autocorrelation analysis (for more explanation see figure 33) was performed on the images recorded in the green channel indicating that EWI-2 induces domains size growth of both CD81 and the palmitoylation deficient mutant C/A. Values are given as means ± SE (n = 3 independent experiments; for each experiment values from 7 – 8 membrane sheets were averaged). (E) Autocorrelation analysis of cells co-expressing EWI-2-RFP and CD81-GFP or CD81-Δδ-GFP. Analysis was performed on images recorded in the green channel showing almost three-fold larger domain size (referring to area and assuming circular shape) formed by CD81-GFP when compared to CD81-Δδ-GFP and co-expression of EWI-2-RFP. Values are given as means ± SE (n = 3 independent experiments; for each experiment values from 7 – 11 membrane sheets were averaged). The CD81-GFP/EWI-2-RFP conditions in D and E are identical. The smaller effect by D, can be explained by the presence of 38 % of very low EWI-2 expressing cells to only 22 % in E (derived from Homsi et al., 2014).

7.15.2 Domain targeting effect is not caused by incomparable expression levels

In addition to CD81 domain targeting (figure 24), domain dynamics (figure 30) and domain stability (figure 31), the association of CD81 with EWI-2 is also δ-domain dependent (figure 36C). Fluorescence intensities analysis as described in (figure 25) revealed that this effect was not caused by incomparable expression levels between EWI2-RFP/CD81-Δδ-GFP and EWI2-RFP/CD81-GFP (figure 37). In addition, I analysed the expression levels of CD81-GFP and CD81-Δδ-GFP under identical conditions via western blot analysis which showed comparable CD81-GFP and CD81-Δδ-GFP expression (see Appendix 2). As incomparable expression levels can be excluded as basis of the observed effect, I concluded that the δ-domain regulates CD81 primary interactions and TEM integration.

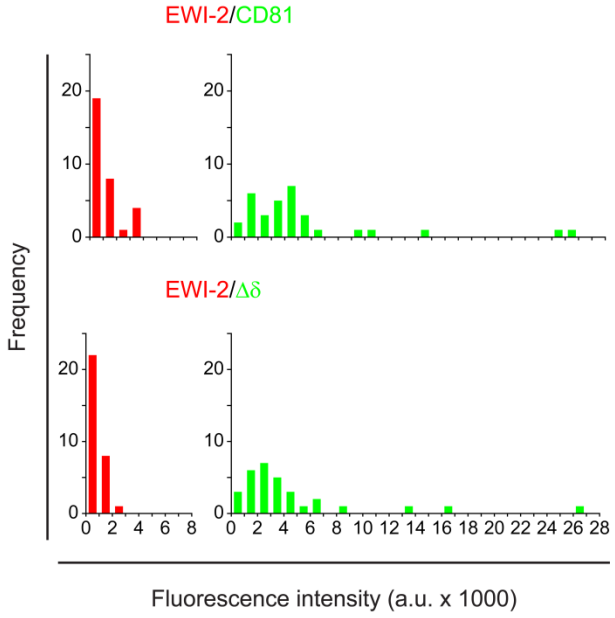

Figure 37. Expression level distribution of CD81-RFP/CD81-GFP and CD81-RFP/CD81-Δδ-GFP constructs in individual membrane sheets of the analyzed data in (figure 36C)

Histograms show the distribution of the fluorescence intensities from individual analyzed membrane sheets in the red (RFP) or the green (GFP) channel prepared and plotted as described in figure 25. Note that the exposure time in the red channel was two-fold the exposure time in the green channel. Histograms show comparably distributed expression levels in the red and the green channel of the mutant and the control.

7.15.3 Development of large TEMs is palmitoylation independent

Appearance of large bright platforms was observed upon elevation of the EWI-2 concentration and only in the presence of wild-type CD81 (figure 36A). Using autocorrelation approach (figure 33) I analysed the structure size, which was strongly increased by overexpression of EWI-2 (figure 36D and E) and only observed in the presence of the δ-domain (figure 36E). This effect was not dependent on palmitoylation of CD81 (figure 36D). The determined platform size of ~560 nm for CD81 domains (figure 36E) is clearly above the resolution limit and even correcting for the blurring effect reduces the value by only ~10 %. In contrast, the size of CD81-Δδ clusters is limited by diffraction, and therefore only an upper estimate can be provided while the real size may be much smaller. These findings show that CD81 and EWI-2 interact with each other (figure 36A and C) and that, assuming a circular shape of CD81 platforms, EWI-2 induces an increase in the area size of individual CD81 clusters by a factor of 3 (figure 36E), an effect which was not dependent on palmitoylation (figure 36D). In contrast, this interaction is δ-domain dependent (figure 36B and C). Therefore, upon EWI-2 elevation CD81-Δδ clusters did not grow and remained close to diffraction-limited size (figure 36E).

7.16 The microscopic observations correlate with the biochemical results

The microscopic observations showed different degrees of overlap between CD81 and putatively interacting proteins (figure 38). The highest PCC value I calculated was determined between CD81 and CD81 (0.6; figure 24), followed by the value derived for the overlap between CD81 and EWI-2 (0.53; figure 36). These high PCC values, which are close to the value for perfectly overlapping probes as determined in figure 20, indicate a strong interaction related to a primary interaction. In contrast, the determined PCC between CD81 and CD9 was much lower (0.35; figure 32), reflecting the presence of a secondary interaction. Therefore,

the level of interactions observed in immunoprecipitation and biochemical experiments as described above (primary and secondary interactions or interactions level 1 and level 2) is also reflected by the degree of overlap determined via microscopic approaches.

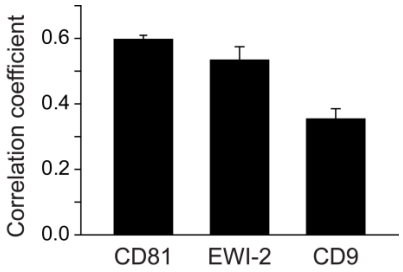

Figure 38. The absolute values of the PCC between CD81 and CD81, EWI-2 or CD9 document large agreement between microscopic and biochemical approaches for studying CD81 interactions

The histogram illustrates the average absolute values of the correlation coefficients between CD81-GFP and CD81-RFP (figure 24; n = 15), CD81-GFP and EWI-2-RFP (figure 36; n = 6) and CD81-GFP and CD9-RFP (figure 32; n = 3); the correlation values indicate the degree of interactions that correlates well with the published biochemistry results (derived from Homsi et al., 2014).

7.17 Elevation of primary interaction partners per se is not sufficient to form large TEMs

The microscopic observations shown in figure 36 suggest that CD81 interacts with EWI-2 which induces the formation of larger tetraspanin platforms, caused by increased primary complexes driven by the elevation of the primary interaction partner EWI-2. This proposition is well in line with previous work, where EWI-2wint (EWI-2 without its N-terminus, a natural cleavage product of EWI-2 Rocha-Perugini et al., 2008) influences the mobility of CD81 and reduces its global diffusion due to an increase in the proportion of confined molecules (Potel et al., 2013). The cluster-missorting seen for CD81-$\Delta\delta$-GFP (figure 36B and C) could be caused by a lowered stabilizing effect of the CD81-LEL on the interaction with EWI-2. Such interactions should still be possible since CD81 and EWI-2 interact also via their TMs and intracellular domains (Montpellier et al., 2011). The same experiment as shown in figure 36 was performed in HepG2 cells by overexpressing CD81 with and without EWI-2 (figure 39A). Here no

increase in CD81 domain size upon elevation of EWI-2 was observed (figure 39B and C). This finding suggests that elevation of primary complexes induces the platform growth seen in Jurkat cells, but per se is not sufficient to drive the primary complexes into large TEMs or webs. In addition, the determination of CD81 cluster size in HepG2 cells at increased resolution using STED microscopy (figure 39C) suggests that CD81 clusters in HepG2 cells are smaller than those in Jurkat cells (figure 36D). Albeit, this could not be definitely resolved, since the autocorrelation analysis in (figure 36D) was not yielded from STED images. However, multiplying the determined 50% autocorrelation value by two (in figure 36D) yields an estimate of the CD81 cluster size in Jurkat cells which appears to be slightly greater than the resolution limit (compare with figure 33C). Therefore, the observed differences in CD81 cluster size between HepG2 and Jurkat cells may explain the different lateral diffusion coefficient for CD81 calculated in this work for Jurkat cells (figure 30C) which was lower compared to slightly higher values previously published for HepG2 cells (Harris et al., 2013).

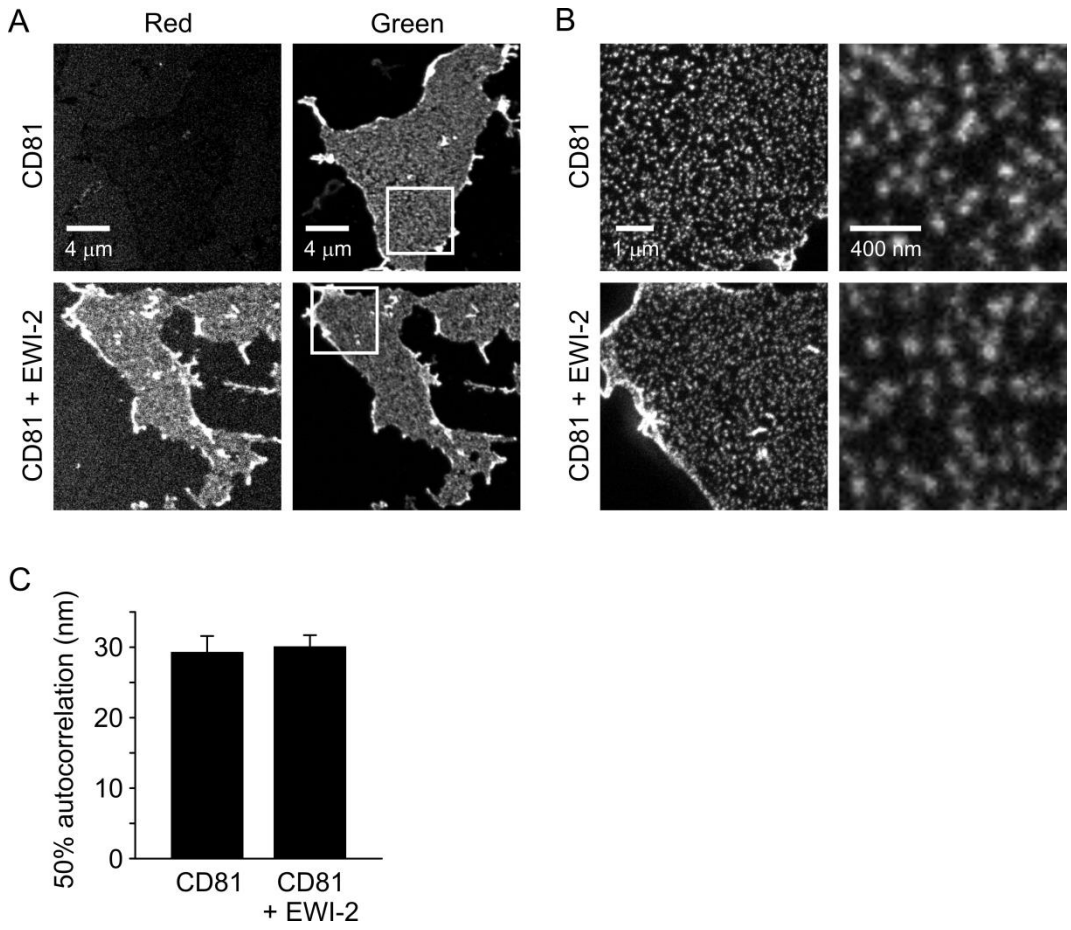

Figure 39. The expression of EWI-2 did not increase CD81 cluster size in HepG2

Membrane sheets derived from figure 22 in addition with membrane sheets prepared at the same day from HepG2 cells co-transfected with CD81-GFP and EWI-2-RFP were used for autocorrelation analysis on STED-micrographs. CD81-GFP clusters were imaged using STED microscopy as described in figure 22. (A) Confocal images documenting the expression of EWI-2-RFP (red channel) and/or CD81-GFP (green channel). Upper panels, membrane sheet #2 from figure 22 A visualized in the red and green channels and shown at grey scale look up table, indicating the expression of CD81-GFP and the absence of EWI-2-RFP expression. Lower panels, membrane sheet prepared from a cell co-overexpressing EWI-2-RFP and CD81-GFP. Red images as well as green images were shown at same scaling, respectively. (B) Left, STED micrographs corresponding to the areas within the white squares in A derived from STED image overviews. Three ROIs (one shown in the right panel) on the STED overviews were selected for cluster size analysis by autocorrelation analysis (see 6.5.5). Same scaling using the grey look up table was used for all STED images. (C) Autocorrelation analysis results showing that the CD81-cluster size in HepG2 membrane sheets remains small even upon overexpression of EWI-2-RFP. Values are given as means ± SE (n = 3 independent experiments; for each experiment 5 – 13 membrane sheets were averaged). Data analyzed by Dr. Jan-Gero Schlötel and Prof. Thorsten Lang (derived from Homsi et al., 2014).

7.18 The CD81 δ-domain is necessary to form functional CD81 microdomains

As mentioned above, CD81 plays an important role during pathogen entry, which is driven by either direct interaction with CD81 independently from assembling into TEMs like by HCV (Rocha-Perugini et al., 2009) or by providing pathogen entry and/or exit platforms via building TEMs or tetraspanin webs like by HIV (Nydegger et al., 2006) or HPV (Scheffer et al., 2013; Spoden et al., 2008). Here, I aimed at studying the function at significance of the δ-domain during the formation of large TEMs to be used for pathogen induced endocytosis. As pathogen model, I used pseudovirions (PsVs) derived from HPV type 16 (see 6.1.8) to test whether CD81-GFP platforms are able to promote PsVs uptake and whether for this process the δ-domain is essential.

7.18.1 Pathogen-induced endocytosis analysed on membrane sheets

The treatment of Jurkat cells overexpressing CD81-GFP with PsVs strongly changed the pattern of CD81-GFP in the cell membrane and induced the formation of membrane sheet-associated endosomes overlapping with CD81 accumulated platforms (figure 40A). In contrast, in the absence of the δ-domain no changes of the CD81-Δδ-GFP distribution were seen, and PsV induced endosomes were rarely detected (figure 40B). Quantification of endosomes per cell base showed only for CD81-GFP a huge PsV-induced endocytosis whereas in the absence of the δ-domain endocytosis remained at control levels (figure 40C). These findings are completely new in the virology field and indicate that only in the presence of physiological large CD81 platforms or TEMs the PsV-induced endocytosis takes place. Therefore, the pathogen endocytosis is δ-domain dependent and HPV PsVs require physiological CD81 platforms for their proper uptake.

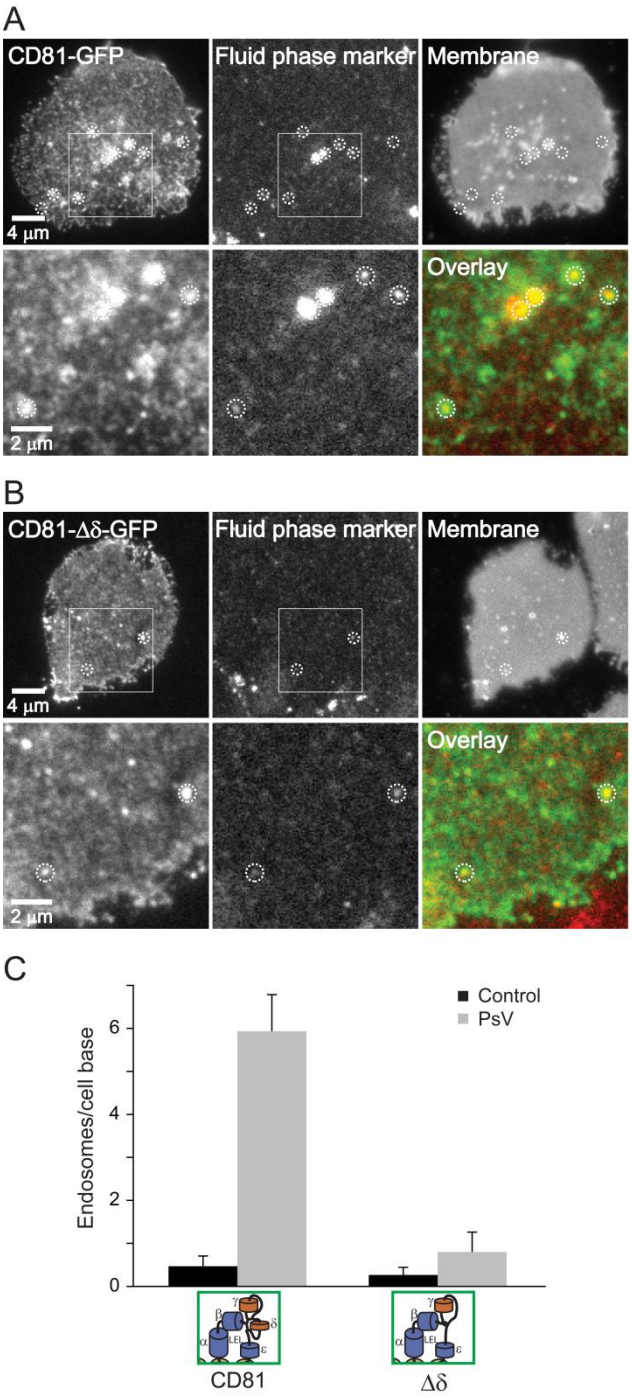

Figure 40. CD81 δ-domain is necessary for virus endocytosis

Jurkat cells expressing either CD81-GFP (A) or CD81-Δδ-GFP (B) were incubated in the presence of a fluid phase marker (20 µM sulforhodamine) for 10 min at 37 °C with (A and B) or without (control) HPV pseudovirions (PsVs). Cells were then adhered onto PLL-coated glass coverslips for 20 min at 37 °C; membrane sheets were generated and imaged in the green channel (CD81-GFP or CD81-Δδ-GFP), red channel (visualizing integrated fluid phase marker in form of red spots indicating sealed organelles associated with the plasma membrane), and blue channel (visualizing membrane integrity via the lipid dye TMA-DPH). (A) Treatment of cells with PsVs dramatically changed the pattern of CD81 distribution and led to accumulation of CD81 domains that

often overlap with an endosome; similar pattern could be seen in the TMA-DPH image that also often overlap with the accumulated CD81 domains indicating a huge deformation of the plasma membrane and the presence of a multiple lipid bilayer stack due to the formation of a membrane-engulfed endosome. (B) The same treatment with PsVs did not affect the clustering pattern of CD81-Δδ-GFP, and this construct was hardly detected in endocytic organelles. Upper panels from left to right, images recorded in the green, red and blue channels; lower panels, magnified views of the white square ROIs indicated in the upper panels and overlays. Dotted circles indicate identical pixel localizations. (C) Pixelwise overlapping endosomes with GFP-accumulations within cell bases were counted and the average of the quantified endosomes from different membrane sheets was calculated. Values are given as mean ± SE (n = 3 independent experiments; for each experiment and condition 5 membrane sheets were analysed and quantified) (derived from Homsi et al., 2014).

7.18.2 Pathogen-induced endocytosis analysed on intact cells

As in figure 40, the same experiment was repeated with whole cells omitting the sonication step. Only for the green channel TIRF microscopy was used selectively showing the GFP-signal distribution in the basal cell membrane. This experiment confirms the formation of PsV-triggered CD81-GFP platform accumulations overlapping with membrane-associated endosomes on intact cells (figure 41A) whereas in the absence of the δ-domain no changes were detected (figure 41B). Please note that the red channel was recorded using epifluorescence microscopy showing a high fluorescence background from the cell body. Even at this low signal to noise ratio, I was able to distinguish endosomes within the focal plane overlapping with CD81 platforms in the green channel, though at lower sensitivity yielding an accordingly lower number of detected endosomes per cell base (figure 41C).

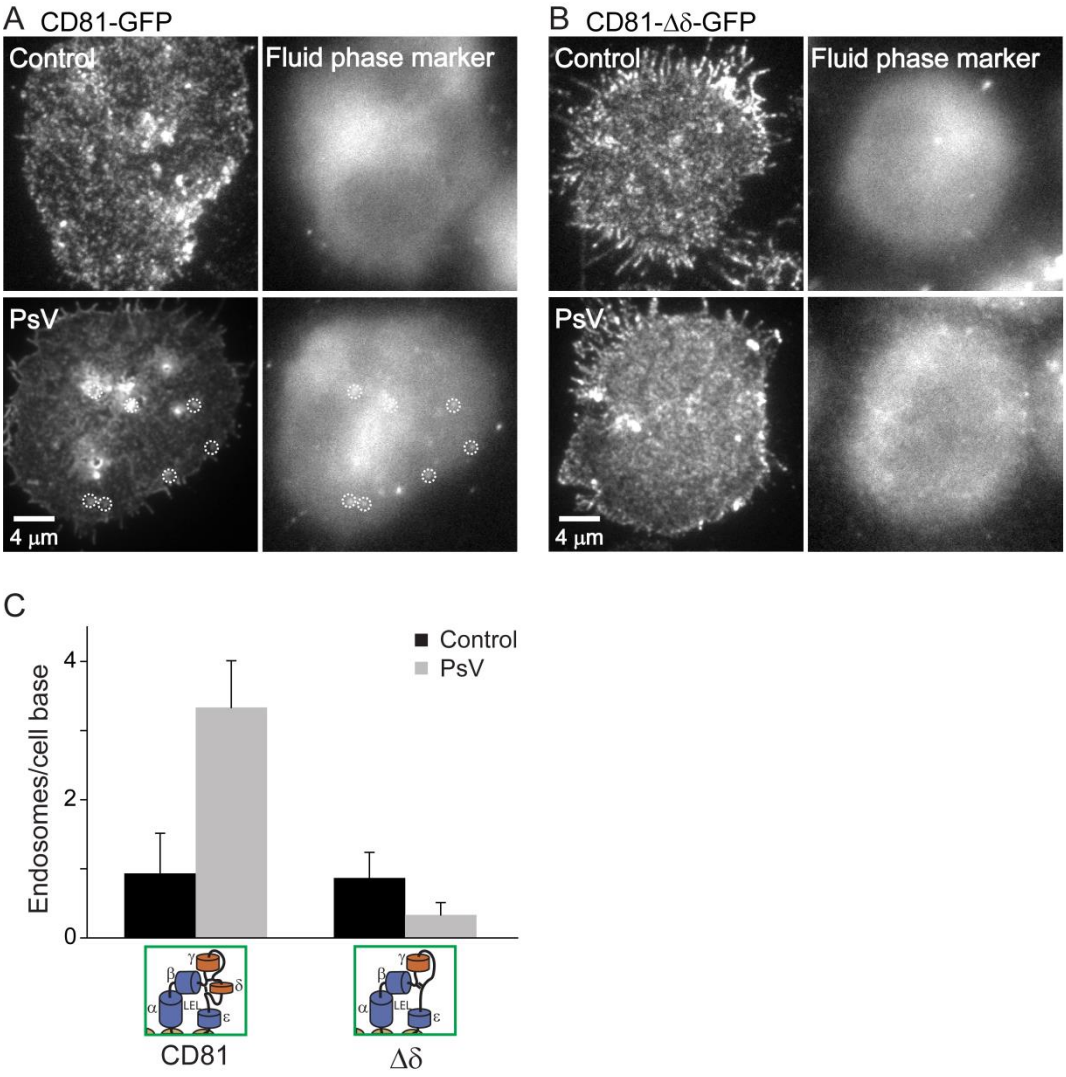

Figure 41. Deletion of CD81 δ-domain affects PsV endocytosis

(A – C) Jurkat cells overexpressing either CD81-GFP (A) or CD81-Δδ-GFP (B) were incubated with (A and B upper panels) or without (A and B lower panels; control) HPV pseudovirions (PsVs) for 10 min at 37 °C in the presence of a fluid phase marker (20 µM sulforhodamine) as described in figure 40. Cells were adhered onto PLL-coated coverslips for 20 min at 37 °C and directly fixed, washed and imaged in the green channel (left panels) using TIRF microscopy visualizing overexpressed CD81-GFP or CD81-Δδ-GFP or in the red channel (right panels) using epifluorescence microscopy to detect internalized fluid phase marker in form of endosomes. Epifluorescence images show strong out of focus background signals coming from internal compartments of the cells decreasing the signal-to-noise ratio; in spite of the noisy signal in the red channel, it was possible to count endosomes in close proximity to the cell membrane. As seen in figure 40A, pseudovirions changed the pattern of CD81 domain distribution in form of huge and bright accumulations of domains that from ring-like structures engulfing sealed endosomes overlapping with red spots in the red channel and possibly not completely sealed endosomes which are not visible in the red channel (A; lower panel). This effect was not seen in the control images (A; upper panel). (B) The pattern of CD81-Δδ-GFP remains unchanged upon treatment with PsVs and rarely endosomes were observed. (C) Quantification of endosomes overlapping with GFP-accumulations (CD81-GFP or CD81-

Δδ-GFP). Values are mean ± SE (n = 3 independent experiments; for each experiment and condition 5 cells were analysed).

7.18.3 Pseudovirions uptake analysed on intact cells using confocal microscopy

In figures 40 and 41, a short incubation time with PsVs was chosen to observe PsV-induced endosomes that are located at the focal plane of the basal membrane and are still associated with it. Next, I increased the incubation time with PsVs to let the endosomes propagate into the cell body. For a more specific detection of PsVs containing endosomes, I used anit-HPV-L1 antibody (see 6.1.4.1) to immunostain PsV particles after cell permeabilization. Using confocal microscopy, I was able to detect immunostained PsV particles widely distributed throughout the cytosol. Internalized PsV particles were only seen in cells overexpressing CD81-GFP where they overlapped with CD81-GFP accumulations (figure 42A; upper panels). In contrast, in the absence of the δ-domain, hardly any stained PsV particles inside the cells were observed. Rather, some PsV particles were attached to the outer surface of the cells. In addition, no large CD81-Δδ accumulations were detected after PsVs infection (figure 42A; lower panels). Quantification of cells containing one or more GFP-accumulations inside the cell body overlapping with immunostained HPV-L1 particles showed a strong decrease of internalized viral particles upon overexpressing of CD81-Δδ (figure 42B).

This finding indicates that CD81-Δδ clusters are not able to generate platforms suitable for PsVs uptake; therefore the δ-domain is crucial for CD81 to build or to integrate into functional platforms which are capable to act as pathogen entry points.

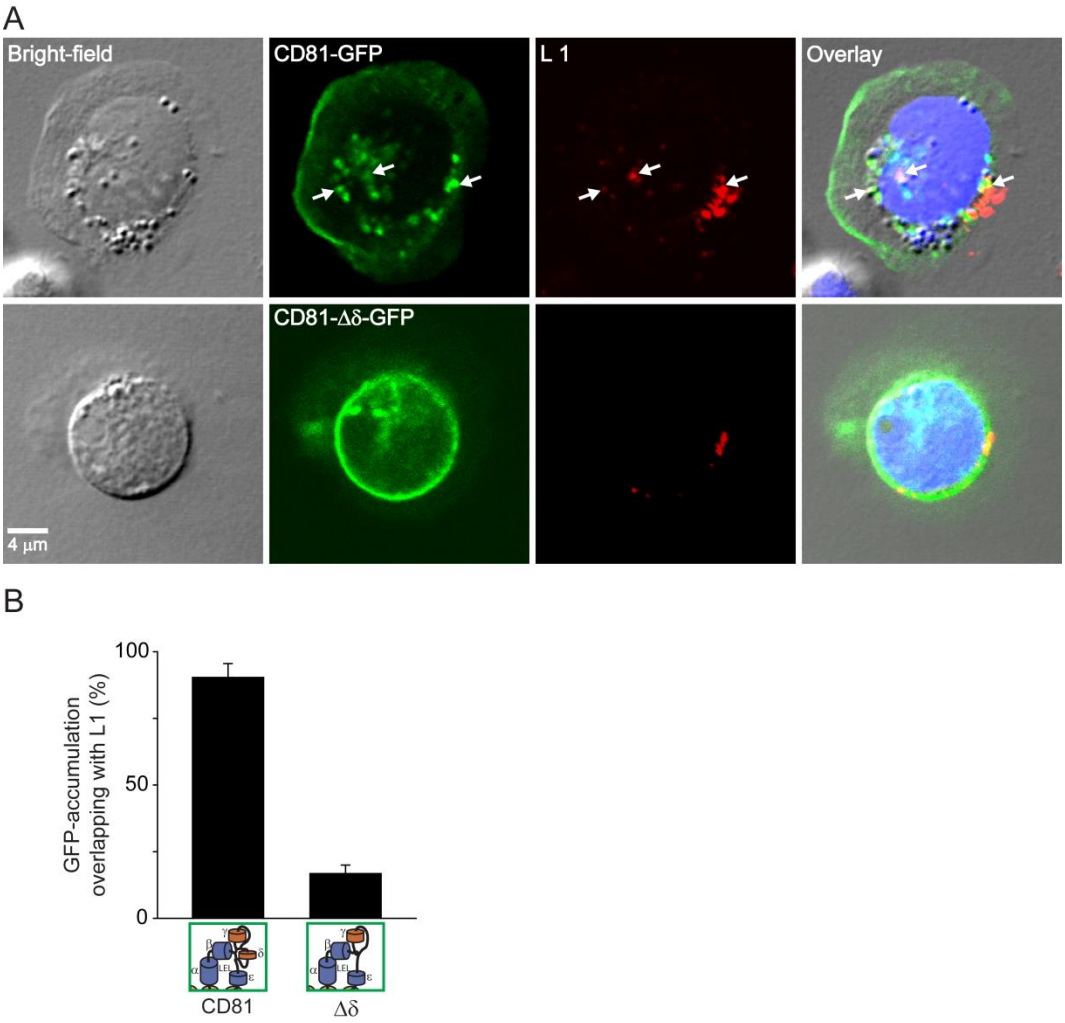

Figure 42. Internalized PsV particles analysed by confocal microscopy

(A) Jurkat cells expressing either CD81-GFP (upper panels) or CD81-Δδ-GFP (lower panels) were incubated for 1 h at 37 °C with PsVs, adhered for 20 min at 37 °C onto PLL-coated glass coverslips, fixed, permeabilized and immunostained for the PsV protein L1. Jurkat cells have a large nucleus and a small cytosolic volume, and during cell adhesion the plasma membrane spreads out and attaches tightly to the coverslips in a manner that most cytosolic compartments are found at the bottom of the adhered cells in a thin planar section beyond the coverslip, where the recorded confocal scans were taken. Sometimes, due to the membrane spreading across the coverslip, the cell membrane was pulled down and closely associated to the nucleus even in the proximity of the coverslip (lower panel). From left to right, bright-field images, confocal scans in the green channel (CD81-GFP or CD81-Δδ-GFP), confocal scans in the red channel (immunostained L1 PsV protein) and overlays. Internalized PsVs and/or PsVs that co-localized with GFP-accumulations were observed by cells overexpressing CD81-GFP (upper panels) but hardly seen in cells overexpressing CD81-Δδ-GFP. These accumulations of CD81-GFP overlapping with stained viral particles are likely largely identical to the previously observed accumulations of CD81-GFP overlapping with the fluid phase marker in membrane sheets (figure 40) and intact cells (figure 41). Arrows indicate identical locations in different channels. Images are shown at arbitrary scaling. (B) Cells that contain at least one overlapping GFP-accumulation (CD81-GFP or CD81-Δδ-GFP) with stained viral particles were counted and the percentage of all analysed

cells was calculated. Values are given as mean ± SE (n = 3 independent experiments; for each experiment and condition 9 – 11 cells were analysed) (derived from Homsi et al., 2014).

8 Discussion

8.1 Organization of proteins in the cell membrane

The basic structure of the cell membrane has been a very important issue for researchers since the discovery of cell organelles. The topic has maintained its importance until today, since many questions have not been answered yet. Cell membrane components and their behavior have been studied over years. The principle structure has been discussed in several models starting from Danielli and Davson's model (1935) to Singer and Nicolson's model (1972) (see 4.3). Singer and Nicolson's model revolutionized the concept of the membrane basic structure and introduced the cell membrane as a fluid of a lipid bilayer in which proteins are inserted and are able to diffuse freely. This dynamic description opened new windows to study the lateral organization of membrane components. The main biological question about lateral organization within the membrane is how proteins can build specific clusters and be sorted in different microdomains. This important phenomenon is still not completely understood. After elucidation of the membrane basic structure as mentioned before, the lateral organization within the cell membrane has been further investigated and explained with different models e.g. the picket fence model in which proteins are captured in diffusion compartments formed via protein interaction with cell cytoskeleton (Kusumi et al., 2005) or the lipid raft model in which the proteins are enriched in lipid rafts generated by clustering of sphingolipids and cholesterol in the outer membrane of the lipid bilayer (Chen et al., 2004; Lingwood & Simons, 2010). Nonetheless, the mechanisms suggested are neither able to explain the high degree of micropatterning, nor the high specificity of segregation observed for two isoforms of a protein that share a high degree of structural similarity (Kai et al., 2006; Low et al., 2006; Uhles et al., 2003). Therefore, specific interaction between proteins should be the main force which drives proteins to segregate preferentially into their appropriate domains.

Another suggested model to explain the high protein micropatterning is the cluster phase model (Destainville, 2008; Homsi et al., 2014; Meilhac & Destainville, 2011). This model is based on the competition between short-range attractions (few times the thermal energy K_BT; Alberts et al., 2008; Phillips, Kondev et al., 2009) at ~1 nm between proteins in a dense phase, and long-range repulsions (close to or lower than the thermal energy) at ~10 nm (Meilhac & Destainville, 2011). Consequently, at these specific and sensitive interaction ranges small variations of the attractive forces can result in huge changes in protein clustering including protein segregation or sorting into specialized, distinct clusters. This is due to the counterbalanced cost in entropy by the gain of stabilizing interactions (Homsi et al., 2014; Meilhac & Destainville, 2011). In contrast to the classical view mentioned above, the cluster phase model takes into account the dynamical interaction of the attractive forces. Therefore, binary interaction which may occur within a short protein-protein interaction motif cannot generate a stable state over long time scale. However, dynamic metastable interactions which have the ability to generate permanent cycles of flexible interactions that break up through thermal agitation and can explain why in cluster phases most molecules are free to diffuse inside clusters (Espenel et al., 2008). Moreover, this kind of interaction features allow molecules to enter and leave clusters and diffuse freely in the membrane to reach another cluster and integrate into it. This concept suggests that modulation of these weakened flexible forces could have a huge effect on molecule segregation. This point of view has been observed in other studies showing that small modifications of a single protein domain can induce protein missorting or abolish clustering (Schreiber et al., 2012). Such observations cannot be explained with the classical view which only focused on the loss of one direct primary interaction in which case only the number of binary complexes decreases, but would not influence the capability of the protein to segregate into clusters or to build completely distinct clusters. Theoretically, the cluster phase predicts that an increased concentration of interaction partners has an influence on the number rather than on the size of clusters (Destainville & Foret, 2008). This behavior has been

experimentally observed in (Sieber et al., 2006). In contrast, growth of clusters is predicted to occur if attractive forces are increased as a result between attractive and repulsive forces.

In conclusion, the cluster phase model could be an alternative approach to describe and understand the lateral organization of the cell membrane based on the dynamic features of protein interactions.

8.2 TEMs and approaches for studying static and dynamic features

As outlined in the introduction, TEMs constitute a highly stoichiometric assembly of several proteins driven by an unknown mechanism. TEMs were mainly studied using biochemical approaches such as immunoprecipitation and density gradient centrifugation. Microscopy, in contrast has rarely been used. Biochemical methods yield a static view not able to deliver any information about the dynamics of TEM components during assembly or to differentiate between TEMs at different growth states. Focussing for many years on this single strategy for studying TEMs was a weakness in this research field and has delayed the understanding of the proper mechanism that drives these proteins assemblies.

The first report that studied tetraspanin and TEM behavior in a dynamic view was (Espenel et al., 2008) who used microscopic approaches such as single-molecule analysis to compare trajectories of different tracked single tetraspanins and to calculate the lateral diffusion coefficient of a single tetraspanin while entering and leaving a TEM. This new dynamic information in the tetraspanin field has inspired other groups to suggest the first dynamic model of TEM building based on these microscopic results (see figure 9) (Charrin et al., 2009). The microscopic approaches have revolutionized the concept of TEMs being just static protein assemblies or macro-clusters of different protein components, but suggested that TEMs are rather dynamic assemblies of proteins which are in a continuous dynamical interaction network with their surroundings.

Here, I studied the dynamics of CD81 using FRAP microscopy and I showed, as will be discussed in detail in the following, that CD81 diffusion depends on the δ-domain (see figure 30). Using TIRF microscopy, my data indicate that the δ-domain is necessary for building TEMs because this specific domain is required for TEM stability over time (see figure 31). This kind of information was collected using dynamic imaging approaches. In addition, static microscopy approaches have been used in parallel to biochemical approaches. Astonishingly, the static microscopic methods I used in this work perfectly correlated with previously reported biochemical results (see figure 38). Moreover, the immunoprecipitation results in this work shown in figures 27 and 28 correlated also with the microscopic observations because upon deletion of the δ-domain not only loss in co-clustering but also interaction with protein partners were weakened. I conclude that microscopic methods could introduce realistic approaches for studying microdomains in both static and dynamic ways, and open new avenues to extend our understanding about tetraspanins and TEM mechanism and protein clustering in general with respect to the classical biochemical approaches.

8.3 Fluorescent protein labelling of CD81 does not alter its function

FP-tagging of proteins always varies concerns regarding physiological behavior. However as mentioned before, similar C-terminally FP-tagged CD81 constructs have been successfully used in previous studies by other groups (Coller et al., 2009; Mittelbrunn et al., 2002). Additionally, the microscopic findings are perfectly in line with previous data based on immunoprecipitation experiments (see 8.2), indirectly indicating that FP-tagging does not seriously alter the behavior of CD81. Moreover, the new immunoprecipitation data generated in this work confirms that CD81-GFP still binds to both endogenous CD81 and CD9 (figures 27 and 28). Finally, the immunostaining experiments for endogenous CD81 (see 7.1) confirm that CD81-GFP is co-enriched with endogenous CD81 with a high degree of correlation and both molecules form clusters together (figure 20). In

conclusion, all observations strongly indicate that FP-tagging does not alter the physiological function and behavior of proteins.

8.4 Mechanisms of CD81 web formation and stabilization

The lateral association of tetraspanins includes different categories of interactions (Berditchevski & Rubinstein, 2013). These different interaction stages are classified on the basis of their resistance to detergents. The first-level of interaction is direct and maintained after harsh detergent treatment (Yáñez-Mó et al., 2009). These tetraspanin-partner interactions are assumed to be the most stable interactions mediated by tetraspanin molecules. In contrast, the second-level of interactions is formed by tetraspanin-tetraspanin contacts and can only survive mild detergent treatment (Charrin et al., 2009; Yáñez-Mó et al., 2009). In some reviews, the interactions are classified in level 1 referring to direct interactions including direct tetraspanin-tetraspanin interactions or tetraspanin dimerization and level 2 referring to the secondary interactions mediated by palmitoylation (Hemler, 2005). Therefore, the first level or tetraspanin-partner interactions constitute the initial step of TEM formation; and in our case, the interaction between CD81 and EWI-2 plays this crucial role in the organization of TEMs. The assembly of tetraspanins and their partners in TEMs or web is assumed to result from a network of interactions that grows to form TEMs, which represent large supra-molecular complexes.

I studied the lateral association of CD81 in two cell types and I found that the δ-domain is essential for CD81 organization and assembly in CD81 rich clusters or platforms. The δ-domain is required for physiological clusters able to grow and to form larger platforms in the presence of EWI-2, however only in Jurkat cells. My data confirm that the primary interaction between CD81 and EWI-2 is crucial for TEM formation, but is not per se sufficient. Instead, additional interactions with other factors are required for TEM growth and assembly, probably also including a CD81 dimerization step, as observed by the disturbed association of CD81 with CD81-Δδ in the immunoprecipitation experiments.

During the characterization of the CD81 domain(s)/feature(s) important for CD81 assembly, I deleted the α- and β-helices responsible for weak hydrophobic interactions which are required for hydrophobic CD81 dimerization or I removed the palmitoylation sites. These changes led only to minor differences in clustering behavior. The analysis of the molecular distribution in the plasma membrane from a static view cannot exclude that weak interactions, palmitoylation or other regions of the CD81 molecule do play a role during protein biosynthesis and trafficking in the endoplasmatic reticulum or Golgi-apparatus or that their absence may affect the mean residence time of CD81 in TEMs at a long time range. However, the data are in line with previous work showing that palmitoylation deficient CD9 only has a slightly increased diffusion coefficient (by ~20 %) and almost retains its fraction of confined molecules (with a small ~10 % reduction) (Espenel et al., 2008). Taken together, this confirms that palmitoylation may play a secondary stabilizing role by tetraspanin interactions.

Referring to these results, I conclude that CD81 clustering requires the δ-domain which is also essential for CD81 to colocalize with CD9 (figure 32) or EWI-2 (figure 36). Therefore, the δ-domain is crucial for tetraspanin domain clustering and represents the starting point to form large TEMs. Additionally, it regulates TEM development and dynamics.

The above observation is interesting because the variable domain of the LEL specifies tetraspanins (it has a different aa sequence for each tetraspanin member), and it is varied in length and secondary structure (Seigneuret et al., 2001). If it is possible that δ-domains in all tetraspanin had the same function, they would be essential for the formation of large TEMs each specifically with distinct binding partners. This suggestion is in accordance with previously published studies showing that a chimera CD9 molecule carrying only the LEL of CD81 behaves like CD81 in viral entry (Zhang et al., 2004).

8.5 Are there other co-factors necessary for TEM growth?

In this work I was able to detect TEM growth upon increasing the concentration of EWI-2 protein which represents a primary interaction partner of most important tetraspanin molecules including CD81 and CD9 (Charrin et al., 2003; Kolesnikova et al., 2003; Sala-Valdés et al., 2006). Moreover, EWI-2 plays a central role in TEM building and ensures the connection to the actin cytoskeleton through its direct association with ERM-proteins (Sala-Valdés et al., 2006). As discussed above (see 8.1), cluster growth is theoretically predicted when attractive forces are increased (see 4.3.4 and figure 7). This effect was observed in Jurkat cells when increasing the EWI-2 concentration (figure 36). However, increasing the EWI-2 concentration had no effect in HepG2 cells (figure 39). These observations indicate that TEM growth may be regulated by other factors, which may have to be present to initiate the growth process. Previous reports showed that some tetraspanins interact directly with integrins and form complexes e.g. CD81/α4β1, CD151/α3β1 and CD151/α6β1 which are very stable and resistant to digitonin detergent treatment. Moreover, these tetraspanin/integrin complexes are affected by altered integrin expression (Serru et al., 1999). Another report documented a similar effect of integrin expression on tetraspanin clustering, where α3β1 and α6β4 integrins promoted CD9 clustering (Yang et al., 2006). Additionally, EWI-2 is identified as a prominent cell-surface partner for α4β1 integrin and at the same time a CD81 primary protein partner (as mentioned above). Hence, these three proteins form the EWI-2-CD81-α4β1 complex which is promoted by EWI-2 overexpression (Kolesnikova et al., 2003). Thus, α4β1 integrin together with EWI-2 and CD81 influence clustering and protein complex building. CD81 and EWI-2 were overexpressed together in HepG2 and Jurkat cells; therefore, an important issue is to check whether Jurkat or HepG2 cells express the third complex member α4β1. Interestingly, both integrin components α4 and β1 of α4β1 are expressed in Jurkat cells (Kolesnikova et al., 2003), whereas only β1 integrin is expressed in

HepG2, while α4 is missing (Londrigan et al., 2000) or at least in a monolayer-culture (Ohno et al., 2009). Hence, these observations taken together with the literature indicate that α4 may be also a prerequisite for complex building. In addition, α4β1 integrin plays an important role in cell motility and fibronectin matrix assembly (Wu et al., 1995). More precisely, in Jurkat cells the α4 integrin associates physically with praxillin (a signaling adapter). Praxillin binds to α4 at high stoichiometry and connects the α4 tail to other integrins to form a complex (Liu et al., 1999). Finally, CD81 is described as a central linker between EWI-2 and α4β1 (Kolesnikova et al., 2003). I may suggest that the simultaneously presence of EWI-2, CD81 and α4β1 conceivably together with other molecules or co-factors such as praxillin is necessary to form big cluster or TEM, an effect seen here only in Jurkat cells.

8.6 Does CD81 really constitute a master organizer of the plasma membrane?

CD81 is ubiquitously expressed in nearly all cell types (Oren et al., 1990). Moreover, the participation of CD81 in different cellular processes (see 4.5.2) indicates that this protein plays a central role in cell membrane organization. The depletion of CD81 leads to acute physiological disorders seen in $CD81^{-/-}$ knockout mice which developed humeral immune response disorder (Tsitsikov et al., 1997), spontaneous formation of multinuclear giant cells (Takeda et al., 2003), protein biosynthesis disorders (Shoham et al., 2003), low fertility (Rubinstein et al., 2006) as well as altered, lymphocyte proliferative responses (Miyazaki et al., 1997), neurobehavioral sensitivity (Michna et al., 2001), brain (Geisert et al., 2002) and retinal pigment epithelium (Pan et al., 2011) development. In addition, CD81 is involved in pathogen entry (see table 1 and 4.5.2). Most of these effects occur at the plasma membrane and are dependent on the correct distribution and function of different cell surface components. As shown in (figure 31B and D), the non-functional, δ-domain-deleted version of CD81 (CD81-Δδ) showed a highly disordered clustering behaviour and a high degree of domain instability. In addition, overexpression of CD81-

Δδ, even in the presence of endogenous CD81 in Jurkat cells, affected pathogen induced endocytosis (compare figures 40, 41 and 42). These results indicate that protein domain formation and distribution may play a key role in cellular processes mediated by cell surface, and that CD81 may be a central protein indispensable for domain organization, building and distribution. Furthermore, the affected pathogen entry in the presence of both CD81-Δδ and endogenous CD81 seen in this work indicates that CD81- Δδ plays a dominant negative role by acting antagonistically to wild-type CD81. Moreover, CD81 knockdown induced serious disorder of integrin clusters figure 34, and also affected cell adhesion and motility (Quast et al., 2011). This important phenotype observed upon depletion of CD81 via siRNA is in line with the previous findings and all data confirm that CD81 constitutes a master organizer of the plasma membrane that plays an important role in membrane protein clustering and distribution.

8.7 Cluster phase as an alternative, more realistic explanation for tetraspanins web formation

According to previous concepts of TEM or web building, the classical view of TEM formation suggests that a large TEM is generated by a defined sequence of interactions which connects proteins with each other to form a network and allows them to grow laterally to form supra-molecular clusters.

In contrast, the static and dynamic results found in this work, which cannot be explained by this classical view of TEM building, indicate that the issue of TEM organization and protein micropatterning mechanisms is rather controlled by a more physical, dynamical, simple explanation related to the cluster phase model discussed above (see 8.1).

My data have shown that the deletion of the δ-domain (only 11 aa) leads to protein segregation in different clusters; such moderate attraction forces, which involve only few residue-residue interactions represent the specific interactions which control the preferential interaction of proteins to be integrated into specific clusters. This indicates that a very specific

interaction between proteins plays the main role in protein organization and controls the micropatterning mechanisms. These moderate interactions represent the metastable interactions described by the cluster phase model (see 8.1) which may explain the ability of a single tetraspanin molecule to diffuse freely inside clusters and even change between clusters after a free diffusion step in the membrane as seen by (Espenel et al., 2008).

Therefore, the δ-domain interactions (metastable interactions) play an essential role to ensure higher energetic affinity and thermodynamically more stable attractions between CD81 and its partners, in addition to other less specific attraction forces. As shown above, the deletion of the δ-domain heavily disturbs the colocalization between CD81-Δδ and CD9 (figure 32) or EWI-2 (figure 36).

Astonishingly, the theoretical concept of the cluster phase model has been reinforced by many experimental results found in this work. First, for a wide range of CD81 concentrations more, but similarly sized clusters were observed (figure 22). This validates the suggestion described by (Destainville & Foret, 2008), that the increased concentration of a cluster component has minor effects on cluster size but dramatically increases the number of clusters, similar to previous observations seen by (Sieber et al., 2006). Second, the deletion of a small single protein domain (the δ-domain) has induced protein missorting and abolished TEM clustering (see figures 24, 32 and 36). These findings cannot be explained with the classical view which only focusses on the loss of one direct primary interaction, but rather reinforce the presence of metastable interactions controlling protein organization as described in 8.1. Finally, the cluster phase model suggests that growth of clusters is predicted to occur upon increasing of attractive forces. This suggestion was also validated with my findings and observed upon increasing the EWI-2 concentration (see figure 36) or the presence of soluble interaction partners on the surface represented by the PsVs (see figures 40 and 41). Therefore, the new findings in this work represent an alternative explanation, in which the

mechanism controlling TEM building may be based on the cluster phase model.

In conclusion, the arguments of previous reports on the cluster phase theory are reinforced in this work and support the hypothesis described in (Homsi et al., 2014) namely that CD81 and its partners form cluster phases driven by free-energy gain, which results from weak interactions e.g. via hydrophobic interfaces or palmitoylation or by more specific interactions involving the δ-domain (see Appendix 3). This work opens new avenues for a better understanding of the TEM building and represents a new dynamical concept of protein lateral organization that may inspire future suggestions on TEM building mechanisms or protein organization models.

8.8 Are all observed CD81-enriched platforms TEMs?

The microscopy data in this work document that over a wide concentration range CD81 is assembled in domains. These domains are enriched with CD81, but the possibility of presence of other TEM and non-TEM components cannot be excluded. In addition, the data deliver several arguments indicating that the CD81 platforms observed represent TEMs. In particular the large CD81 microdomains represent bona fide TEMs. The primary interaction partner EWI-2, which is known as an essential TEM component, is recruited into the CD81 domains increasing their size. In addition, the tetraspanin CD9, whose association with CD81 occurs only into TEMs also co-enriches with CD81 domains. Moreover, the CD81 domains show lower lateral mobility, more robust morphology and higher stability compared to non-TEM CD81-Δδ clusters that do not overlap neither with EWI-2 nor with CD9. Finally, the CD81 domains represent physiological platforms able to promote PsV-triggered endocytosis. These arguments confirm that the studied CD81 platforms in this work actually represent TEMs. Such detail seen by microscopic approaches would not be revealed in biochemical experiments. This paints out the importance of studying TEMs with microscopic approaches that in the future may give

more detailed answers about the significance of heterogeneity of observed TEMs.

8.9 The role of CD81 TEMs in pathogen entry

8.9.1 CD81 organized in TEMs is required for HPV endocytosis

The CD81 molecule has been described in many studies as an important player in pathogen entry (see table 1) (Monk & Partridge, 2012; van Spriel, Annemiek B & Figdor, 2010). As mentioned before, the mechanism that drives pathogen entry is dependent on the type of pathogen (see 4.5.2). For example, direct association with CD81 is required for the early steps of HCV entry (Potel et al., 2013; Rocha-Perugini et al., 2009). In contrast, the organization of CD81 into TEMs is a prerequisite for pathogen entry in the case of *Plasmodium* (Silvie et al., 2006) and HIV (Krementsov et al., 2010; Nydegger et al., 2006). In addition, HPV endocytosis is also gated via TEM association, where virus particles together with CD81-containing TEMs co-internalize into endosomes in an actin mediated, but clathrin-, caveolin-, and dynamin-idependent pathway (Scheffer et al., 2013; Scheffer et al., 2014). My data confirm that the organization of CD81 into functional platforms is required for HPV pseudovirions triggered endocytosis, which is strongly affected by perturbation of TEM assembly. Hence, these observations confirm also that HPV endocytosis is mediated by TEMs which generate linkage to the actin cytoskeleton, since CD81 directly binds to EWI-2 and both interact further with ERM-proteins (Coffey et al., 2009; Gordón-Alonso et al., 2012; Sala-Valdés et al., 2006; Stipp et al., 2003) which generate association with cell cytoskeleton (Arpin et al., 2011). Therefore, CD81 plays a key role by TEM building and the formation of functional CD81 platforms requires the δ-domain.

8.9.2 Possibilities to treat pathogen entry by inhibition of CD81 organization

The most popular strategy for interfering with pathogen entry is the application of antibodies raised against CD81 or especially the LEL of CD81 (Meuleman & Leroux-Roels, 2008; Silvie et al., 2003; Spoden et al., 2008). In this work I identified a much smaller domain (the δ-domain including only 11 aa) to play the key role in CD81 organization and pathogen entry. Therefore, it would be sufficient to interfere with this small domain by using an aptamer which is much cheaper and easier to produce, and can inhibit CD81 platform formation and consequently affect viral entry. Moreover, this therapeutical strategy could be clinically very convenient and much easier to realize.

9 Conclusion and outlook

In this work I identified the function of the δ-domain of CD81, a small protein domain of only 11 aa that according to the data controls tetraspanin clustering and TEM building, and plays a key role in the formation of functional tetraspanin webs.

In collaboration with Prof. Dr. Nicolas Destainville, based on these findings, an improved, general TEM building model is suggested, which is stimulating new ideas and concepts in the field of the tetraspanin research. However, the complete TEM building mechanism including all its necessary components is still not completely known. Based on these findings, future works should identity more potential key players for TEM organization, such as integrins, immunoglobulin superfamily members, and other critical tetraspanins (e.g. CD82, CD151, etc…). More protein candidates could be determined by immunoprecipitation analysis with endogenous CD81 after TEM building (e.g. during EWI-2 overexpression). Using gated STED super resolution microscopy, clustering behavior and cluster size could be studied at different stages of TEM formation. In this way, the size and shape of TEMs could be analyzed over a large concentration range of CD81 and/or EWI-2 in the cell membrane.

Moreover, referring to super resolution images, TEMs could be quantitatively analyzed to estimate the real proportions of different TEM components, revealing the relationship between the concentration of different TEM components and TEM number, size and shape.

Additional experiments using dynamic approaches are also required to understand the mechanism of TEM building over time.

The understanding of the physiological function of TEMs also has high importance in the therapeutical field. Deletion of the δ-domain of the CD81 protein affected the formation of physiologically active TEMs and consequently HPV entry. Therefore, additional infection experiments on different cell lines and different pathogens could reinforce my findings and

generalize the role of the δ-domain in pathogen entry. Additionally, the small size of the δ-domain (only 11 aa) making it an interesting target for future therapeutic strategies.

Finally, TEMs constitute a membrane microdomain with key roles in diverse cellular processes, but the mechanism of their formation is still not completely clear to date. My data supplemented with the suggested TEM building model open new windows to study the mechanisms and principles of TEM formation using modern microscopic analysis.

10 Literature

Abbe, E. (1873). *Beltrage zur theorie des mikroskops und der mikroskopischen wahrnehmung …* [Bonn].

Adler, J. & Parmryd, I. (2010). Quantifying colocalization by correlation: the Pearson correlation coefficient is superior to the Mander's overlap coefficient. *Cytometry A* **77** (8), 733–742.

Alberts, B., Wilson, J. H. & Hunt, T. (2008). *Molecular biology of the cell*, 5th edn. New York, N.Y., Abingdon: Garland Science.

Arpin, M., Chirivino, D., Naba, A. & Zwaenepoel, I. (2011). Emerging role for ERM proteins in cell adhesion and migration. *Cell Adh Migr* **5** (2), 199–206.

Avery, J., Ellis, D. J., Lang, T., Holroyd, P., Riedel, D., Henderson, R. M., Edwardson, J. M. & Jahn, R. (2000). A cell-free system for regulated exocytosis in PC12 cells. *J. Cell Biol.* **148** (2), 317–324.

Axelrod, D., Koppel, D. E., Schlessinger, J., Elson, E. & Webb, W. W. (1976). Mobility measurement by analysis of fluorescence photobleaching recovery kinetics. *Biophys. J.* **16** (9), 1055–1069.

Barreiro, O., Zamai, M., Yáñez-Mó, M., Tejera, E., López-Romero, P., Monk, P. N., Gratton, E., Caiolfa, V. R. & Sánchez-Madrid, F. (2008). Endothelial adhesion receptors are recruited to adherent leukocytes by inclusion in preformed tetraspanin nanoplatforms. *J. Cell Biol.* **183** (3), 527–542.

Bartosch, B., Dubuisson, J. & Cosset, F.-L. (2003). Infectious Hepatitis C Virus Pseudo-particles Containing Functional E1-E2 Envelope Protein Complexes. *Journal of Experimental Medicine* **197** (5), 633–642.

Berditchevski, F. & Odintsova, E. (2007). Tetraspanins as regulators of protein trafficking. *Traffic* **8** (2), 89–96.

Berditchevski, F. & Rubinstein, E. (2013). *Tetraspanins.* Dordrecht, New York: Springer.

Berditchevski, F., Odintsova, E., Sawada, S. & Gilbert, E. (2002). Expression of the palmitoylation-deficient CD151 weakens the association of alpha 3 beta 1 integrin with the tetraspanin-enriched microdomains and affects integrin-dependent signaling. *J. Biol. Chem.* **277** (40), 36991–37000.

Boucheix, C. & Rubinstein, E. (2001). Tetraspanins. *Cell. Mol. Life Sci.* **58** (9), 1189–1205.

Burlone, M. E. & Budkowska, A. (2009). Hepatitis C virus cell entry: role of lipoproteins and cellular receptors. *J. Gen. Virol.* **90** (Pt 5), 1055–1070.

Cambi, A. & Lidke, D. S. *Cell membrane nanodomains: From biochemistry to nanoscopy*.

Campbell, R. E., Tour, O., Palmer, A. E., Steinbach, P. A., Baird, G. S., Zacharias, D. A. & Tsien, R. Y. (2002). A monomeric red fluorescent protein. *Proc. Natl. Acad. Sci. U.S.A.* **99** (12), 7877–7882.

Chang, C. H., Takeuchi, H., Ito, T., Machida, K. & Ohnishi, S. (1981). Lateral mobility of erythrocyte membrane proteins studied by the fluorescence photobleaching recovery technique. *J Biochem* **90** (4), 997–1004.

Charrin, S., Le Naour, F., Oualid, M., Billard, M., Faure, G., Hanash, S. M., Boucheix, C. & Rubinstein, E. (2001). The major CD9 and CD81 molecular partner. Identification and characterization of the complexes. *J. Biol. Chem.* **276** (17), 14329–14337.

Charrin, S., Le Naour, F., Silvie, O., Milhiet, P.-E., Boucheix, C. & Rubinstein, E. (2009). Lateral organization of membrane proteins: tetraspanins spin their web. *Biochem. J.* **420** (2), 133–154.

Charrin, S., Manié, S., Oualid, M., Billard, M., Boucheix, C. & Rubinstein, E. (2002). Differential stability of tetraspanin/tetraspanin interactions: role of palmitoylation. *FEBS Lett.* **516** (1-3), 139–144.

Charrin, S., Le Naour, F., Labas, V., Billard, M., Le Caer, J.-P., Emile, J.-F., Petit, M.-A., Boucheix, C. & Rubinstein, E. (2003). EWI-2 is a new component of the tetraspanin web in hepatocytes and lymphoid cells. *Biochem. J.* **373** (Pt 2), 409–421.

Chen, Y., Yang, B. & Jacobson, K. (2004). Transient confinement zones: A type of lipid raft? *Lipids* **39** (11), 1115–1119.

Claas, C., Stipp, C. S. & Hemler, M. E. (2001). Evaluation of prototype transmembrane 4 superfamily protein complexes and their relation to lipid rafts. *J. Biol. Chem.* **276** (11), 7974–7984.

Clark, K. L., Zeng, Z., Langford, A. L., Bowen, S. M. & Todd, S. C. (2001). PGRL Is a Major CD81-Associated Protein on Lymphocytes and

Distinguishes a New Family of Cell Surface Proteins. *The Journal of Immunology* **167** (9), 5115–5121.

Coffey, G. P., Rajapaksa, R., Liu, R., Sharpe, O., Kuo, C.-C., Krauss, S. W., Sagi, Y., Davis, R. E., Staudt, L. M. & other authors (2009). Engagement of CD81 induces ezrin tyrosine phosphorylation and its cellular redistribution with filamentous actin. *J. Cell. Sci.* **122** (Pt 17), 3137–3144.

Coller, K. E., Berger, K. L., Heaton, N. S., Cooper, J. D., Yoon, R. & Randall, G. (2009). RNA interference and single particle tracking analysis of hepatitis C virus endocytosis. *PLoS Pathog.* **5** (12), e1000702.

Cormier, E. G., Tsamis, F., Kajumo, F., Durso, R. J., Gardner, J. P. & Dragic, T. (2004). CD81 is an entry coreceptor for hepatitis C virus. *Proc. Natl. Acad. Sci. U.S.A.* **101** (19), 7270–7274.

Danielli, J. F. & Davson, H. (1935). A contribution to the theory of permeability of thin films. *J. Cell. Comp. Physiol.* **5** (4), 495–508.

Delandre, C., Penabaz, T. R., Passarelli, A. L., Chapes, S. K. & Clem, R. J. (2009). Mutation of juxtamembrane cysteines in the tetraspanin CD81 affects palmitoylation and alters interaction with other proteins at the cell surface. *Exp. Cell Res.* **315** (11), 1953–1963.

DeSalle, R., Mares, R. & Garcia-España, A. (2010). Evolution of cysteine patterns in the large extracellular loop of tetraspanins from animals, fungi, plants and single-celled eukaryotes. *Mol. Phylogenet. Evol.* **56** (1), 486–491.

Destainville, N. & Foret, L. (2008). Thermodynamics of nanocluster phases: A unifying theory. *Phys. Rev. E* **77** (5).

Destainville, N. (2008). Cluster phases of membrane proteins. *Physical review. E, Statistical, nonlinear, and soft matter physics* **77** (1 Pt 1), 011905.

Drummer, H. E., Wilson, K. A. & Poumbourios, P. (2005). Determinants of CD81 dimerization and interaction with hepatitis C virus glycoprotein E2. *Biochem. Biophys. Res. Commun.* **328** (1), 251–257.

Dupuy, A. D. & Engelman, D. M. (2008). Protein area occupancy at the center of the red blood cell membrane. *Proc. Natl. Acad. Sci. U.S.A.* **105** (8), 2848–2852.

Espenel, C., Margeat, E., Dosset, P., Arduise, C., Le Grimellec, C., Royer, C. A., Boucheix, C., Rubinstein, E. & Milhiet, P.-E. (2008). Single-molecule analysis of CD9 dynamics and partitioning reveals multiple modes of interaction in the tetraspanin web. *J. Cell Biol.* **182** (4), 765–776.

Evans, M. J., Hahn, T. von, Tscherne, D. M., Syder, A. J., Panis, M., Wölk, B., Hatziioannou, T., McKeating, J. A., Bieniasz, P. D. & Rice, C. M. (2007). Claudin-1 is a hepatitis C virus co-receptor required for a late step in entry. *Nature* **446** (7137), 801–805.

Ficz, G., Heintzmann, R. & Arndt-Jovin, D. J. (2005). Polycomb group protein complexes exchange rapidly in living Drosophila. *Development* **132** (17), 3963–3976.

Flint, M., Maidens, C., Loomis-Price, L. D., Shotton, C., Dubuisson, J., Monk, P., Higginbottom, A., Levy, S. & McKeating, J. A. (1999). Characterization of Hepatitis C Virus E2 Glycoprotein Interaction with a Putative Cellular Receptor, CD81. *J Virol* **73** (8), 6235–6244.

Frishman, D. & Argos, P. (1995). Knowledge-based protein secondary structure assignment. *Proteins* **23** (4), 566–579.

Geisert, E. E., Williams, R. W., Geisert, G. R., Fan, L., Asbury, A. M., Maecker, H. T., Deng, J. & Levy, S. (2002). Increased brain size and glial cell number in CD81-null mice. *J. Comp. Neurol.* **453** (1), 22–32.

Goñi, F. M. (2014). The basic structure and dynamics of cell membranes: an update of the Singer-Nicolson model. *Biochim. Biophys. Acta* **1838** (6), 1467–1476.

Gordón-Alonso, M., Sala-Valdés, M., Rocha-Perugini, V., Pérez-Hernández, D., López-Martín, S., Ursa, A., Alvarez, S., Kolesnikova, T. V., Vázquez, J. & other authors (2012). EWI-2 association with α-actinin regulates T cell immune synapses and HIV viral infection. *Journal of immunology (Baltimore, Md. : 1950)* **189** (2), 689–700.

Harris, H. J., Clerte, C., Farquhar, M. J., Goodall, M., Hu, K., Rassam, P., Dosset, P., Wilson, G. K., Balfe, P. & other authors (2013). Hepatoma polarization limits CD81 and hepatitis C virus dynamics. *Cell. Microbiol.* **15** (3), 430–445.

Heckman, K. L. & Pease, L. R. (2007). Gene splicing and mutagenesis by PCR-driven overlap extension. *Nat Protoc* **2** (4), 924–932.

Hell, S. W. & Wichmann, J. (1994). Breaking the diffraction resolution limit by stimulated emission: stimulated-emission-depletion fluorescence microscopy. *Opt Lett* **19** (11), 780–782.

Hemler, M. E. (2003). Tetraspanin proteins mediate cellular penetration, invasion, and fusion events and define a novel type of membrane microdomain. *Annu. Rev. Cell Dev. Biol.* **19**, 397–422.

Hemler, M. E. (2005). Tetraspanin functions and associated microdomains. *Nat Rev Mol Cell Biol* **6** (10), 801–811.

Hemler, M. E. (2008). Targeting of tetraspanin proteins--potential benefits and strategies. *Nat Rev Drug Discov* **7** (9), 747–758.

Hemler, M. E. (2013). Tetraspanin proteins promote multiple cancer stages. *Nat Rev Cancer* **14** (1), 49–60.

Heuser, J. (2000). The Production of 'Cell Cortices' for Light and Electron Microscopy. *Traffic* **1** (7), 545–552.

Homsi, Y., Schloetel, J.-G., Scheffer, K. D., Schmidt, T. H., Destainville, N., Florin, L. & Lang, T. (2014). The Extracellular δ-Domain is Essential for the Formation of CD81 Tetraspanin Webs. *Biophys. J.* **107** (1), 100–113.

Hooke, R. (1667). *[Micrographia, 1665. [A facsimile of the edition of 1665.]]*.

Huang, B., Babcock, H. & Zhuang, X. (2010). Breaking the diffraction barrier: super-resolution imaging of cells. *Cell* **143** (7), 1047–1058.

Huang, S., Yuan, S., Dong, M., Su, J., Yu, C., Shen, Y., Xie, X., Yu, Y., Yu, X. & other authors (2005). The phylogenetic analysis of tetraspanins projects the evolution of cell-cell interactions from unicellular to multicellular organisms. *Genomics* **86** (6), 674–684.

Humphrey, W., Dalke, A. & Schulten, K. (1996). VMD: Visual molecular dynamics. *Journal of Molecular Graphics* **14** (1), 33–38.

Kaczmarek, J., Homsi, Y., van Üüm, J., Metzger, C., Knolle, P. A., Kolanus, W., Lang, T. & Diehl, L. (2014). Liver sinusoidal endothelial cell-mediated CD8 T cell priming depends on co-inhibitory signal integration over time. *PloS one* **9** (6), e99574.

Kai, M., Sakane, F., Jia, Y.-J., Imai, S.-I., Yasuda, S. & Kanoh, H. (2006). Lipid phosphate phosphatases 1 and 3 are localized in distinct lipid rafts. *J. Biochem.* **140** (5), 677–686.

Kitadokoro, K., Bordo, D., Galli, G., Petracca, R., Falugi, F., Abrignani, S., Grandi, G. & Bolognesi, M. (2001). CD81 extracellular domain 3D structure: insight into the tetraspanin superfamily structural motifs. *EMBO J.* **20** (1-2), 12–18.

Kitadokoro, K., Ponassi, M., Galli, G., Petracca, R., Falugi, F., Grandi, G. & Bolognesi, M. (2002). Subunit association and conformational flexibility in the head subdomain of human CD81 large extracellular loop. *Biol. Chem.* **383** (9), 1447–1452.

Kolesnikova, T. V., Stipp, C. S., Rao, R. M., Lane, W. S., Luscinskas, F. W. & Hemler, M. E. (2003). EWI-2 modulates lymphocyte integrin α4β1 functions. *Blood* **103** (8), 3013–3019.

Kovalenko, O. V., Metcalf, D. G., DeGrado, W. F. & Hemler, M. E. (2005). Structural organization and interactions of transmembrane domains in tetraspanin proteins. *BMC Struct Biol* **5**, 11.

Krementsov, D. N., Rassam, P., Margeat, E., Roy, N. H., Schneider-Schaulies, J., Milhiet, P.-E. & Thali, M. (2010). HIV-1 Assembly Differentially Alters Dynamics and Partitioning of Tetraspanins and Raft Components. *Traffic* **11** (11), 1401–1414.

Kusumi, A., Ike, H., Nakada, C., Murase, K. & Fujiwara, T. (2005). Single-molecule tracking of membrane molecules: plasma membrane compartmentalization and dynamic assembly of raft-philic signaling molecules. *Semin. Immunol.* **17** (1), 3–21.

Kyhse-Andersen, J. (1984). Electroblotting of multiple gels: a simple apparatus without buffer tank for rapid transfer of proteins from polyacrylamide to nitrocellulose. *J Biochem Biophys Methods* **10** (3-4), 203–209.

Laemmli, U. K. (1970). Cleavage of structural proteins during the assembly of the head of bacteriophage T4. *Nature* **227** (5259), 680–685.

Lavillette, D., Pécheur, E.-I., Donot, P., Fresquet, J., Molle, J., Corbau, R., Dreux, M., Penin, F. & Cosset, F.-L. (2007). Characterization of fusion determinants points to the involvement of three discrete regions of both E1 and E2 glycoproteins in the membrane fusion process of hepatitis C virus. *J. Virol.* **81** (16), 8752–8765.

Le Naour, F., Andre, M., Boucheix, C. & Rubinstein, E. (2006). Membrane microdomains and proteomics: lessons from tetraspanin microdomains and comparison with lipid rafts. *Proteomics* **6** (24), 6447–6454.

Levy, S. & Shoham, T. (2005a). Protein-protein interactions in the tetraspanin web. *Physiology (Bethesda)* **20**, 218–224.

Levy, S. & Shoham, T. (2005b). The tetraspanin web modulates immune-signalling complexes. *Nat. Rev. Immunol.* **5** (2), 136–148.

Lingwood, D. & Simons, K. (2010). Lipid rafts as a membrane-organizing principle. *Science* **327** (5961), 46–50.

Liu, S., Thomas, S. M., Woodside, D. G., Rose, D. M., Kiosses, W. B., Pfaff, M. & Ginsberg, M. H. (1999). Binding of paxillin to alpha4 integrins modifies integrin-dependent biological responses. *Nature* **402** (6762), 676–681.

Liu, S., Yang, W., Le Shen, Turner, J. R., Coyne, C. B. & Wang, T. (2009). Tight junction proteins claudin-1 and occludin control hepatitis C virus entry and are downregulated during infection to prevent superinfection. *J. Virol.* **83** (4), 2011–2014.

Londrigan, S. L., Hewish, M. J., Thomson, M. J., Sanders, G. M., Mustafa, H. & Coulson, B. S. (2000). Growth of rotaviruses in continuous human and monkey cell lines that vary in their expression of integrins. *The Journal of general virology* **81** (Pt 9), 2203–2213.

Low, S. H., Vasanji, A., Nanduri, J., He, M., Sharma, N., Koo, M., Drazba, J. & Weimbs, T. (2006). Syntaxins 3 and 4 are concentrated in separate clusters on the plasma membrane before the establishment of cell polarity. *Mol. Biol. Cell* **17** (2), 977–989.

Martin, F., Roth, D. M., Jans, D. A., Pouton, C. W., Partridge, L. J., Monk, P. N. & Moseley, G. W. (2005). Tetraspanins in viral infections: a fundamental role in viral biology? *J. Virol.* **79** (17), 10839–10851.

Masciopinto, F., Campagnoli, S., Abrignani, S., Uematsu, Y. & Pileri, P. (2001). The small extracellular loop of CD81 is necessary for optimal surface expression of the large loop, a putative HCV receptor. *Virus Res* **80** (1-2), 1–10.

Mattheyses, A. L., Simon, S. M. & Rappoport, J. Z. (2010). Imaging with total internal reflection fluorescence microscopy for the cell biologist. *J. Cell. Sci.* **123** (Pt 21), 3621–3628.

Meilhac, N. & Destainville, N. (2011). Clusters of proteins in biomembranes: insights into the roles of interaction potential shapes and of protein diversity. *J Phys Chem B* **115** (22), 7190–7199.

Meuleman, P. & Leroux-Roels, G. (2008). The human liver-uPA-SCID mouse: a model for the evaluation of antiviral compounds against HBV and HCV. *Antiviral Res.* **80** (3), 231–238.

Michna, L., Brenz Verca, Maria S., Widmer, D. A., Chen, S., Lee, J., Rogove, J., Zhou, R., Tsitsikov, E., Miescher, G. C. & other authors (2001). Altered sensitivity of CD81-deficient mice to neurobehavioral effects of cocaine. *Molecular Brain Research* **90** (1), 68–74.

Min, G., Wang, H., Sun, T.-T. & Kong, X.-P. (2006). Structural basis for tetraspanin functions as revealed by the cryo-EM structure of uroplakin complexes at 6-A resolution. *J. Cell Biol.* **173** (6), 975–983.

Mittelbrunn, M., Yanez-Mo, M., Sancho, D., Ursa, A. & Sanchez-Madrid, F. (2002). Cutting Edge: Dynamic Redistribution of Tetraspanin CD81 at the Central Zone of the Immune Synapse in Both T Lymphocytes and APC. *The Journal of Immunology* **169** (12), 6691–6695.

Miyazaki, T., Müller, U. & Campbell, K. S. (1997). Normal development but differentially altered proliferative responses of lymphocytes in mice lacking CD81. *The EMBO journal* **16** (14), 4217–4225.

Monk, P. N. & Partridge, L. J. (2012). Tetraspanins: gateways for infection. *Infect Disord Drug Targets* **12** (1), 4–17.

Montpellier, C., Tews, B. A., Poitrimole, J., Rocha-Perugini, V., D'Arienzo, V., Potel, J., Zhang, X. A., Rubinstein, E., Dubuisson, J. & Cocquerel, L. (2011). Interacting regions of CD81 and two of its partners, EWI-2 and EWI-2wint, and their effect on hepatitis C virus infection. *J. Biol. Chem.* **286** (16), 13954–13965.

Munro, S. (2003). Lipid rafts: elusive or illusive? *Cell* **115** (4), 377–388.

Nydegger, S., Khurana, S., Krementsov, D. N., Foti, M. & Thali, M. (2006). Mapping of tetraspanin-enriched microdomains that can function as gateways for HIV-1. *J. Cell Biol.* **173** (5), 795–807.

Ohno, M., Motojima, K., Okano, T. & Taniguchi, A. (2009). Maturation of the extracellular matrix and cell adhesion molecules in layered co-cultures of HepG2 and endothelial cells. *Journal of biochemistry* **145** (5), 591–597.

Ohtsubo, K. & Marth, J. D. (2006). Glycosylation in cellular mechanisms of health and disease. *Cell* **126** (5), 855–867.

Oren, R., Takahashi, S., Doss, C., Levy, R. & Levy, S. (1990). TAPA-1, the target of an antiproliferative antibody, defines a new family of transmembrane proteins. *Mol. Cell. Biol.* **10** (8), 4007–4015.

Pan, Y., Geisert, D. F., Orr, W. E. & Geisert, E. E. (2011). The effects of a CD81 null mutation on retinal pigment epithelium in mice. *Neurochemical research* **36** (4), 569–573.

Phillips, R., Kondev, J. & Theriot, J. (2009). *Physical biology of the cell.* New York: Garland Science.

Phillips, R., Ursell, T., Wiggins, P. & Sens, P. (2009). Emerging roles for lipids in shaping membrane-protein function. *Nature* **459** (7245), 379–385.

Pike, L. J. (2006). Rafts defined: a report on the Keystone Symposium on Lipid Rafts and Cell Function. *J. Lipid Res.* **47** (7), 1597–1598.

Pileri, P., Uematsu, Y., Campagnoli, S., Galli, G., Falugi, F., Petracca, R., Weiner, A. J., Houghton, M., Rosa, D. & other authors (1998). Binding of hepatitis C virus to CD81. *Science* **282** (5390), 938–941.

Poger, D. & Mark, A. E. (2010). On the Validation of Molecular Dynamics Simulations of Saturated and cis -Monounsaturated Phosphatidylcholine Lipid Bilayers: A Comparison with Experiment. *J. Chem. Theory Comput.* **6** (1), 325–336.

Potel, J., Rassam, P., Montpellier, C., Kaestner, L., Werkmeister, E., Tews, B. A., Couturier, C., Popescu, C.-I., Baumert, T. F. & other authors (2013). EWI-2wint promotes CD81 clustering that abrogates Hepatitis C Virus entry. *Cell. Microbiol.* **15** (7), 1234–1252.

Quast, T., Eppler, F., Semmling, V., Schild, C., Homsi, Y., Levy, S., Lang, T., Kurts, C. & Kolanus, W. (2011). CD81 is essential for the formation of membrane protrusions and regulates Rac1-activation in adhesion-dependent immune cell migration. *Blood* **118** (7), 1818–1827.

Rehm, H. & Letzel, T. (2010). *Der Experimentator: Proteinbiochemie/Proteomics*, 6th edn. Heidelberg: Spektrum Akademischer Verlag.

Rocha-Perugini, V., Gordon-Alonso, M. & Sánchez-Madrid, F. (2014). PIP2: choreographer of actin-adaptor proteins in the HIV-1 dance. *Trends Microbiol.* **22** (7), 379–388.

Rocha-Perugini, V., Lavie, M., Delgrange, D., Canton, J., Pillez, A., Potel, J., Lecoeur, C., Rubinstein, E., Dubuisson, J. & other authors (2009). The association of CD81 with tetraspanin-enriched microdomains is not essential for Hepatitis C virus entry. *BMC Microbiol.* **9**, 111.

Rocha-Perugini, V., Montpellier, C., Delgrange, D., Wychowski, C., Helle, F., Pillez, A., Drobecq, H., Le Naour, F., Charrin, S. & other authors (2008). The CD81 partner EWI-2wint inhibits hepatitis C virus entry. *PLoS ONE* **3** (4), e1866.

Rocha-Perugini, V., Zamai, M., González-Granado, J. M., Barreiro, O., Tejera, E., Yañez-Mó, M., Caiolfa, V. R. & Sanchez-Madrid, F. (2013). CD81 controls sustained T cell activation signaling and defines the maturation stages of cognate immunological synapses. *Mol. Cell. Biol.* **33** (18), 3644–3658.

Rubinstein, E., Le Naour, F., Lagaudrière-Gesbert, C., Billard, M., Conjeaud, H. & Boucheix, C. (1996). CD9, CD63, CD81, and CD82 are components of a surface tetraspan network connected to HLA-DR and VLA integrins. *Eur. J. Immunol.* **26** (11), 2657–2665.

Rubinstein, E., Ziyyat, A., Prenant, M., Wrobel, E., Wolf, J.-P., Levy, S., Le Naour, F. & Boucheix, C. (2006). Reduced fertility of female mice lacking CD81. *Dev. Biol.* **290** (2), 351–358.

Sala-Valdés, M., Ursa, A., Charrin, S., Rubinstein, E., Hemler, M. E., Sánchez-Madrid, F. & Yáñez-Mó, M. (2006). EWI-2 and EWI-F link the tetraspanin web to the actin cytoskeleton through their direct association with ezrin-radixin-moesin proteins. *J. Biol. Chem.* **281** (28), 19665–19675.

Scarselli, E., Ansuini, H., Cerino, R., Roccasecca, R. M., Acali, S., Filocamo, G., Traboni, C., Nicosia, A., Cortese, R. & Vitelli, A. (2002). The human scavenger receptor class B type I is a novel candidate receptor for the hepatitis C virus. *EMBO J* **21** (19), 5017–5025.

Scheffer, K. D., Berditchevski, F. & Florin, L. (2014). The tetraspanin CD151 in papillomavirus infection. *Viruses* **6** (2), 893–908.

Scheffer, K. D., Gawlitza, A., Spoden, G. A., Zhang, X. A., Lambert, C., Berditchevski, F. & Florin, L. (2013). Tetraspanin CD151 mediates papillomavirus type 16 endocytosis. *J. Virol.* **87** (6), 3435–3446.

Schleiden, M. J. (1838). *Beiträge zur Entwicklungsgeschichte der Blüthentheile bei den Leguminosen.* [S.l.].

Schmidt, T. H. & Kandt, C. (2012). LAMBADA and InflateGRO2: efficient membrane alignment and insertion of membrane proteins for molecular dynamics simulations. *J Chem Inf Model* **52** (10), 2657–2669.

Schneider, C. A., Rasband, W. S. & Eliceiri, K. W. (2012). NIH Image to ImageJ: 25 years of image analysis. *Nat Methods* **9** (7), 671–675.

Schreiber, A., Fischer, S. & Lang, T. (2012). The amyloid precursor protein forms plasmalemmal clusters via its pathogenic amyloid-β domain. *Biophysical journal* **102** (6), 1411–1417.

Schwann, T. (1838). *Mikroskopische Untersuchungen über die Uebereinstimmung in der Struktur und dem Wachsthum der Thiere und Pflanzen.* Berlin: Bei G. Reimer.

Seigneuret, M. (2006). Complete predicted three-dimensional structure of the facilitator transmembrane protein and hepatitis C virus receptor CD81: conserved and variable structural domains in the tetraspanin superfamily. *Biophys. J.* **90** (1), 212–227.

Seigneuret, M., Delaguillaumie, A., Lagaudrière-Gesbert, C. & Conjeaud, H. (2001). Structure of the tetraspanin main extracellular domain. A partially conserved fold with a structurally variable domain insertion. *The Journal of biological chemistry* **276** (43), 40055–40064.

Serru, V., Le Naour, F., Billard, M., Azorsa, D. O., Lanza, F., Boucheix, C. & Rubinstein, E. (1999). Selective tetraspan-integrin complexes (CD81/alpha4beta1, CD151/alpha3beta1, CD151/alpha6beta1) under conditions disrupting tetraspan interactions. *Biochem. J.* **340 (Pt 1)**, 103–111.

Sheetz, M. P. (1983). Membrane skeletal dynamics: role in modulation of red cell deformability, mobility of transmembrane proteins, and shape. *Semin. Hematol.* **20** (3), 175–188.

Sheetz, M. P., Schindler, M. & Koppel, D. E. (1980). Lateral mobility of integral membrane proteins is increased in spherocytic erythrocytes. *Nature* **285** (5765), 510–511.

Shoham, T., Rajapaksa, R., Boucheix, C., Rubinstein, E., Poe, J. C., Tedder, T. F. & Levy, S. (2003). The Tetraspanin CD81 Regulates the Expression of CD19 During B Cell Development in a Postendoplasmic Reticulum Compartment. *The Journal of Immunology* **171** (8), 4062–4072.

Sieber, J. J., Willig, K. I., Heintzmann, R., Hell, S. W. & Lang, T. (2006). The SNARE motif is essential for the formation of syntaxin clusters in the plasma membrane. *Biophys. J.* **90** (8), 2843–2851.

Sieber, J. J., Willig, K. I., Kutzner, C., Gerding-Reimers, C., Harke, B., Donnert, G., Rammner, B., Eggeling, C., Hell, S. W. & other authors (2007). Anatomy and dynamics of a supramolecular membrane protein cluster. *Science* **317** (5841), 1072–1076.

Silvie, O., Charrin, S., Billard, M., Franetich, J.-F., Clark, K. L., van Gemert, G.-J., Sauerwein, R. W., Dautry, F., Boucheix, C. & other authors (2006). Cholesterol contributes to the organization of tetraspanin-enriched microdomains and to CD81-dependent infection by malaria sporozoites. *J. Cell. Sci.* **119** (Pt 10), 1992–2002.

Silvie, O., Rubinstein, E., Franetich, J.-F., Prenant, M., Belnoue, E., Rénia, L., Hannoun, L., Eling, W., Levy, S. & other authors (2003). Hepatocyte CD81 is required for Plasmodium falciparum and Plasmodium yoelii sporozoite infectivity. *Nat. Med.* **9** (1), 93–96.

Simons, K. & Gerl, M. J. (2010). Revitalizing membrane rafts: new tools and insights. *Nat. Rev. Mol. Cell Biol.* **11** (10), 688–699.

Simons, K. & Ikonen, E. (1997). Functional rafts in cell membranes. *Nature* **387** (6633), 569–572.

Singer, S. J. & Nicolson, G. L. (1972). The fluid mosaic model of the structure of cell membranes. *Science* **175** (4023), 720–731.

Spoden, G. A., Besold, K., Krauter, S., Plachter, B., Hanik, N., Kilbinger, Andreas F M, Lambert, C. & Florin, L. (2012). Polyethylenimine is a strong inhibitor of human papillomavirus and cytomegalovirus infection. *Antimicrob. Agents Chemother.* **56** (1), 75–82.

Spoden, G., Freitag, K., Husmann, M., Boller, K., Sapp, M., Lambert, C. & Florin, L. (2008). Clathrin- and caveolin-independent entry of human papillomavirus type 16--involvement of tetraspanin-enriched microdomains (TEMs). *PLoS ONE* **3** (10), e3313.

Stipp, C. S., Kolesnikova, T. V. & Hemler, M. E. (2001). EWI-2 is a major CD9 and CD81 partner and member of a novel Ig protein subfamily. *J. Biol. Chem.* **276** (44), 40545–40554.

Stipp, C. S., Kolesnikova, T. V. & Hemler, M. E. (2003). EWI-2 regulates alpha3beta1 integrin-dependent cell functions on laminin-5. *J. Cell Biol.* **163** (5), 1167–1177.

Stipp, C. S., Orlicky, D. & Hemler, M. E. (2001). FPRP, a major, highly stoichiometric, highly specific CD81- and CD9-associated protein. *J. Biol. Chem.* **276** (7), 4853–4862.

Takeda, Y., Tachibana, I., Miyado, K., Kobayashi, M., Miyazaki, T., Funakoshi, T., Kimura, H., Yamane, H., Saito, Y. & other authors (2003). Tetraspanins CD9 and CD81 function to prevent the fusion of mononuclear phagocytes. *The Journal of cell biology* **161** (5), 945–956.

Tham, T. N., Gouin, E., Rubinstein, E., Boucheix, C., Cossart, P. & Pizarro-Cerda, J. (2010). Tetraspanin CD81 is required for Listeria monocytogenes invasion. *Infect. Immun.* **78** (1), 204–209.

Towbin, H., Staehelin, T. & Gordon, J. (1979). Electrophoretic transfer of proteins from polyacrylamide gels to nitrocellulose sheets: procedure and some applications. *Proc Natl Acad Sci U S A* **76** (9), 4350–4354.

Tsitsikov, E. N., Gutierrez-Ramos, J. C. & Geha, R. S. (1997). Impaired CD19 expression and signaling, enhanced antibody response to type II T independent antigen and reduction of B-1 cells in CD81-deficient mice. *Proceedings of the National Academy of Sciences of the United States of America* **94** (20), 10844–10849.

Tsuji, A. & Ohnishi, S. (1986). Restriction of the lateral motion of band 3 in the erythrocyte membrane by the cytoskeletal network: dependence on spectrin association state. *Biochemistry* **25** (20), 6133–6139.

Uhles, S., Moede, T., Leibiger, B., Berggren, P.-O. & Leibiger, I. B. (2003). Isoform-specific insulin receptor signaling involves different plasma membrane domains. *J. Cell Biol.* **163** (6), 1327–1337.

van Meer, G., Voelker, D. R. & Feigenson, G. W. (2008). Membrane lipids: where they are and how they behave. *Nat. Rev. Mol. Cell Biol.* **9** (2), 112–124.

van Spriel, Annemiek B & Figdor, C. G. (2010). The role of tetraspanins in the pathogenesis of infectious diseases. *Microbes Infect.* **12** (2), 106–112.

Veigel, C. & Schmidt, C. F. (2011). Moving into the cell: single-molecule studies of molecular motors in complex environments. *Nat. Rev. Mol. Cell Biol.* **12** (3), 163–176.

Vicidomini, G., Moneron, G., Han, K. Y., Westphal, V., Ta, H., Reuss, M., Engelhardt, J., Eggeling, C. & Hell, S. W. (2011). Sharper low-power STED nanoscopy by time gating. *Nat. Methods* **8** (7), 571–573.

Virchow, R. (1871). *Die Cellularpathologie in ihrer Begründung auf physiologische und pathologische Gewebelehre*, 4th edn. Berlin: Hirschwald.

Weitz, S. & Destainville, N. (2013). Attractive asymmetric inclusions in elastic membranes under tension: cluster phases and membrane invaginations. *Soft Matter* **9** (32), 7804.

Willig, K. I., Rizzoli, S. O., Westphal, V., Jahn, R. & Hell, S. W. (2006). STED microscopy reveals that synaptotagmin remains clustered after synaptic vesicle exocytosis. *Nature* **440** (7086), 935–939.

Wright, M. D., Moseley, G. W. & van Spriel, A B (2004). Tetraspanin microdomains in immune cell signalling and malignant disease. *Tissue Antigens* **64** (5), 533–542.

Wu, C., Fields, A. J., Kapteijn, B. A. & McDonald, J. A. (1995). The role of alpha 4 beta 1 integrin in cell motility and fibronectin matrix assembly. *J Cell Sci* **108 (Pt 2)**, 821–829.

Yáñez-Mó, M., Barreiro, O., Gordon-Alonso, M., Sala-Valdés, M. & Sánchez-Madrid, F. (2009). Tetraspanin-enriched microdomains: a functional unit in cell plasma membranes. *Trends Cell Biol.* **19** (9), 434–446.

Yang, X. H., Kovalenko, O. V., Kolesnikova, T. V., Andzelm, M. M., Rubinstein, E., Strominger, J. L. & Hemler, M. E. (2006). Contrasting effects of EWI proteins, integrins, and protein palmitoylation on cell surface CD9 organization. *The Journal of biological chemistry* **281** (18), 12976–12985.

Yang, X., Claas, C., Kraeft, S.-K., Chen, L. B., Wang, Z., Kreidberg, J. A. & Hemler, M. E. (2002). Palmitoylation of tetraspanin proteins: modulation of CD151 lateral interactions, subcellular distribution, and integrin-dependent cell morphology. *Mol. Biol. Cell* **13** (3), 767–781.

Zacharias, D. A., Violin, J. D., Newton, A. C. & Tsien, R. Y. (2002). Partitioning of lipid-modified monomeric GFPs into membrane microdomains of live cells. *Science* **296** (5569), 913–916.

Zhang, J., Randall, G., Higginbottom, A., Monk, P., Rice, C. M. & McKeating, J. A. (2004). CD81 Is Required for Hepatitis C Virus Glycoprotein-Mediated Viral Infection. *Journal of Virology* **78** (3), 1448–1455.

Zhang, X. A. & Huang, C. (2012). Tetraspanins and cell membrane tubular structures. *Cell. Mol. Life Sci.* **69** (17), 2843–2852.

11 Appendix 1

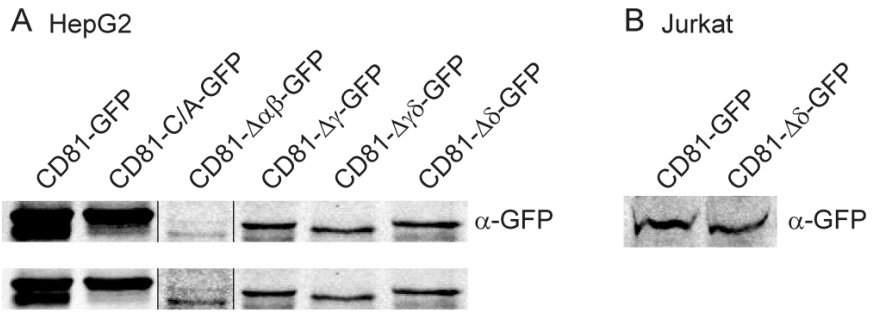

C

Construct	aa	-aa
CD81	236	0
CD81-C/A	236	0
CD81-Δαβ	195	-41
CD81-Δγ	217	-19
CD81-Δγδ	201	-35
CD81-Δδ	225	-11

Appendix 1. Western blot analysis of GFP-tagged CD81 variants in HepG2 and Jurkat cells

(A) HepG2 cells were transfected with GFP-tagged CD81 variants lysed in RIPA buffer and used directly for western blot analysis. GFP-tagged constructs were detected via immunoblotting with anti-GFP (B-2) antibody (#sc-9996, Santa Cruz, USA). Bands were visualized after treatment with the secondary antibody goat anti-Mouse (#926-32210, LI-COR, Germany) and scanning using Odyssey® CLx Imaging System (LI-COR Inc., Lincoln, USA) (for more information see 6.2.7). The detected bands showed the expected sizes for all overexpressed constructs. Note that the varying band intensities may cause by different cell viability after electroporation pulse. Such variability was not relevant for the performed experiments in HepG2 cells because during imaging cohorts of membrane sheets from cells with similar expression levels were obtained. Top section shows non contrasted bands, lower section showed same bands after contrast adjustment. (B) 10^7 Jurkat cells expressing either CD81-GFP or CD81-Δδ-GFP were lysed in RIPA buffer and used directly for western blot analysis following the same protocol as in A. CD81-GFP or CD81-Δδ-GFP detected bands ran at the expected sizes. No degradation products were observed and both constructs showed comparable expression levels. (C) A table shows the names of constructs followed by the number of amino acids in the respective construct sequence (aa) and the number of deleted amino acids compared to wild-type sequence (-aa).

12 Appendix 2

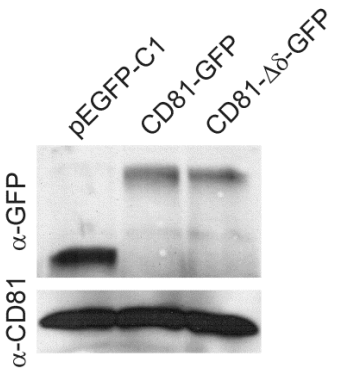

Appendix 2. Western blot analysis of CD81-GFP and CD81-Δδ-GFP in Jurkat cells

10^7 Jurkat cells expressing cytosolic GFP (empty plasmid pEGFP_C1), CD81-GFP or CD81-Δδ-GFP were lysed in 1 % CHAPS lysis buffer (EWI/2-RFP was also co-expressed). Cell lysates were used directly for western blot analysis. GFP-signals were detected via immunoblotting with first antibody anti-GFP rabbit polyclonal (#A11122, Invitrogen, Carlsbad, CA, USA) and second antibody goat anti-rabbit IgG-HRP (#sc-2030, Santa Cruz, USA). Endogenous CD81 was visualized via immunoblotting with first anti-body anti-CD81 (1.3.3.22) mouse monoclonal (#sc-7637, Santa Cruz, USA) and the second antibody goat anti-mouse (#sc-2031, Santa Cruz, USA). Membranes were developed on autoradiography films after treatment with western Blotting Luminol Reagent (#sc-2048, Santa Cruz, USA) (for more information see 6.2.7). The first lane of pEGFP_C1 was used for expression control. CD81-GFP and CD81-Δδ-GFP bands showed similar overexpression levels of both construct. In addition, no degradation products were observed. For loading control, the endogenous CD81 was visualized showing same loaded materials in all lanes.

13 Appendix 3

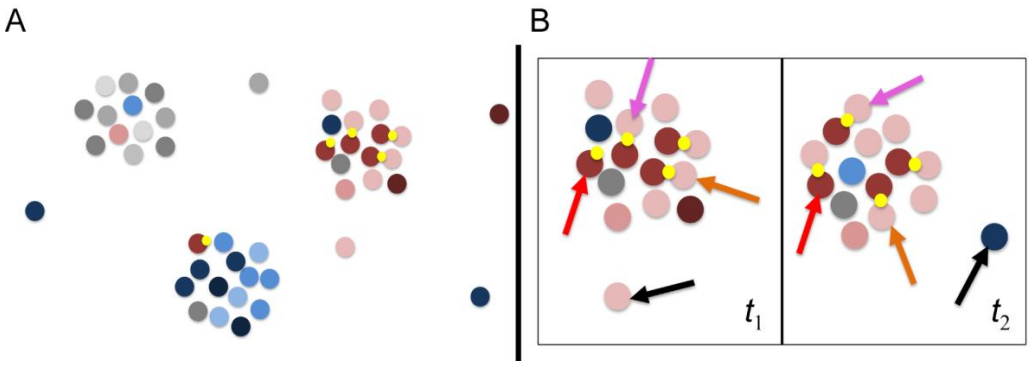

Appendix 3. Cluster phase dynamics model described in (Homsi et al., 2014)

The cartoons represent the cluster phase model at molecular level. (A) Tetraspanin domains formed by tetraspanins and tetraspanin partner proteins are regulated by the competition between moderate short-range attractions, which favor protein assembly in a condensed phase, and long-rage repulsions, which disfavor assembly into a macro-phase. The effect of steric hindrance within clusters causing physical repulsion has been described by (Sieber et al., 2007), and recently, Weitz (2013) proposed that the crystallographic shape of proteins can spontaneously alter membrane curvature which similarly leads to repulsion of proteins within a cluster (Weitz & Destainville, 2013). Proteins segregate in distinct clusters depending on their common energetic affinity (depicted here in different colors grey, red and blue). Therefore, each given color represents a different protein species. While some degree of missorting does occur, this is a rather rare event (Meilhac & Destainville, 2011). Yellow dots indicate the specific interaction sites between brick-red proteins and pink proteins, which represent the protein couple CD81/EWI-2 with yellow dots illustrating the specific interaction sites of δ-domains. (B) Magnified view of the right cluster in A at two different time points $t_2 > t_1$. Within a crowded cluster phase, proteins diffuse laterally when interacting with partner proteins (indicated by purple arrows). Moreover, proteins can also, even within dense clusters, perform rotational diffusion and change interaction partners (illustrated by the red-brick protein interacting with two different proteins simultaneously between t_1 and t_2 and indicated by orange arrows). Sometimes proteins engage in interaction after gaining free energy between t_1 and t_2, because interaction energies are moderate with respect to K_BT (indicated by red arrows). In contrast to the classical view, this model represents clustering at a more dynamic view, where the primary, binary interactions are replaced by a network of fluctuating interactions with temporary partners. This concept fits well to recently published work using single molecule tracking experiments which show that individual proteins can enter and leave domains (Espenel et al., 2008) (indicated here by black arrows) (modified from Homsi et al., 2014).

14 Acknowledgments

First I would like to thank Prof. Dr. Thorsten Lang for providing me with this interesting topic and for always being available for fruitful discussions. I enjoyed his kind supervision showing patience, friendship, professionalism and providing continual help and advice. He encouraged me to grow as an experimental researcher and independent thinker. I would like to thank him too for his critical comments and suggestions on this thesis.

Dr. Luise Florine, I would like to thank you and Dr. Konstanze Scheffer for the friendly and successful collaboration, as well as for exchanging materials and for helping with western blot detection. I will never forget my stay in Mainz doing experiments in your laboratory for two hard, yet enjoyable and productive days. Thank you too for your kindness, generous and cooperativeness. I would be delighted to work with you again.

Prof. Dr. Nicolas Destainville, thank you for your brilliant ideas and pleasant collaboration. The next steps are going to be more and more exciting.

I would like to thank Prof. Dr. Sven Burgdorf, Prof. Dr. Christoph Thiele and Prof. Dr. Ulrich Kubitscheck for taking the time to evaluate this thesis; they were always available for questions and help.

To Prof. Dr. Waldemar Kolanus and Dr. Thomas Quast, it is a pleasure to collaborate with you and I am very thankful for the opportunity to work at your confocal microscope.

Prof. Dr. Linda Diehl and Julita Kaczmarek are thanked for the team work and the successful collaboration.

Many thanks go to Dr. Jan-Gero Schlötel for providing the STED analysis, for critical reading and proof-reading this thesis. Dr. Thomas Schmidt is thanked for providing VMD images.

Many thanks go in particular to Helena Batoulis for her kindness and motivation. I would like to send her special thanks for the critical comments on this thesis and text proof-reading. I wish you all the best in your PhD.

I thank Prof. PhD Martin Hemler for the detailed scientific discussion of tetraspanin assembly as well Dr. Fedor Berditschevski for his critical comments and suggestions. I would like to thank both for the personal meeting at the 6th conference for tetraspanin in Lille France.

I would like to acknowledge Prof. Dr. Joachim Schultze' laboratory for providing the FACS machine and Dr. Marc Beyer, Dr. Verena Schütte and Matthias Zehner for introducing me to operating this machine.

I would also like to thank all the members of the Thiele research group for exchanging materials and experiences, and the Burgdorf research group for exchanging information, reagents and for helping by FACS data analysis.

My thanks also go to the entire Lang group (current and old members) for their team work, numerous conversations and nice surroundings.

I am grateful for the funding sources (SFB 704 and DFG) that allowed me to conduct this research.

Special thanks to my parents for their continuous encouragement, support and prayers.

To everybody who contributed in some way to the successful realization of this thesis I would like to say "Thanks", and apologise that I was not able to mention everybody personally.

And my guidance cannot come except from GOD, in Him I trust and unto Him I repent Quran (11.88)